Multiphysics Modelling of an Alkaline All-Iron, All-Soluble Aqueous Redox Flow Battery

by

Arjun Dhillon

A thesis

Presented to the University of Waterloo

in fulfillment of the

thesis requirement for the degree of

Master of Applied Science

in

Chemical Engineering

Waterloo, Ontario, Canada, 2021

Author's Declaration

I hereby declare that I am the sole author of this thesis. This is a true copy of the thesis, including any required final revisions, as accepted by my examiners.

I understand that my thesis may be made electronically available to the public.

Abstract

The development of redox flow battery (RFB) technologies has attracted considerable attention in recent years. Redox flow batteries are electrochemical energy storage devices that operate as flowing systems. Unlike what is possible in conventional batteries, the ability to size the electrolyte storage tanks and electrodes separately enables the battery energy and power capacities to be decoupled and these important properties to be designed and scaled independently. Such systems are particularly attractive for large-scale grid energy storage, especially in conjunction with intermittent energy generation from renewable sources. As RFBs move from research and development to commercial adoption, the use of mathematical models becomes increasingly important for design and analysis of these systems and is indispensable for ensuring their success. Most RFB modelling to date has focused on the all-vanadium RFB, although novel RFBs are continuously investigated and developed. One such novel RFB is the all-iron all-soluble aqueous RFB that is the focus of the present work. This RFB makes use of iron-cyanide (Fe(II)-CN/Fe(III)-CN) and iron-triethanolamine (Fe(II)-TEOA/Fe(III)-TEOA) redox couples in alkaline aqueous solutions. Both redox couples have fast kinetics and the use of high-pH conditions mitigates the loss of current efficiency due to the hydrogen evolution side reaction.

A model has been developed in the present work for the novel all-iron all-soluble aqueous redox flow battery presented by Gong et al. It is the first model to be developed for this RFB. The transient two-dimensional model considers transport of all redox species in the two electrode compartments using porous electrode theory. The side reaction involving the oxidation of TEOA following its permeation across the ion exchange membrane to the positive side is investigated and incorporated into the model. The hydrogen evolution reaction is also incorporated in the model. Parameter values are obtained from literature where available; the remainder of these values are obtained from fitting of the voltage-time curves for charge and discharge to published experimental data. A simulation of a sequence of repeated charge-discharge cycles is conducted and compared with experimental data. The RFB capacity and current efficiency are stable over this duration,

which is consistent with experimental observations in the original study. The model has been shown to fit the available experimental data well and describe the behaviour of the RFB. The electrode potentials and reactant species concentrations are found to remain fairly uniform, indicating facile mass transport within the electrode. Recommendations are also made on future experimental and modelling work that can be conducted for this system.

Acknowledgements

I offer my sincere thanks to my supervisor, Professor Mark Pritzker, whose support and guidance over the course of this work were indispensable. I also wish to thank Kiana Amini for teaching me about redox flow batteries and COMSOL Multiphysics and for always offering help when it was needed.

I would like to thank Dr. Ke Gong for providing information on his RFB research, on which the present work is based.

I would also like to acknowledge CMC Microsystems for providing access to COMSOL Multiphysics that was necessary to conduct the modelling in the present work.

Table of Contents

List of Figures

List of Tables

Nomenclature

$A_{c,\mathrm{H_2}}$	Tafel slope of hydrogen evolution reaction $[\mathrm{V}]$
a_e	Specific area of porous electrode $[\mathrm{m^{-1}}]$
$A_{\mathrm{electrolyte}}$	Cross-sectional area of current travel through electrolyte $[\mathrm{m^2}]$
c_i	Concentration of species i $\left[\frac{\mathrm{mol}}{\mathrm{m^3}}\right]$
$c_{i,0}$	Inlet concentration of species i $\left[\frac{\mathrm{mol}}{\mathrm{m^3}}\right]$
$C_{O,j}$	Concentration of oxidized form of redox species in reaction j $\left[\frac{\mathrm{mol}}{\mathrm{m^3}}\right]$
$C_{R,j}$	Concentration of reduced form of redox species in reaction j $\left[\frac{\mathrm{mol}}{\mathrm{m^3}}\right]$
$d_{\mathrm{electrolyte}}$	Length of current travel through electrolyte $[\mathrm{m}]$
D_i	Liquid-phase diffusion coefficient of species i $\left[\frac{\mathrm{m^2}}{\mathrm{s}}\right]$
d_{mem}	Membrane thickness $[\mathrm{m}]$
E_j^o	Standard potential of reaction j $[\mathrm{V}]$
$E_j^{o\prime}$	Formal potential of reaction j $[\mathrm{V}]$
$E_{\mathrm{rev},j}$	Reversible (equilibrium) potential of reaction j $[\mathrm{V}]$
i_{app}	Applied current density $\left[\frac{\mathrm{A}}{\mathrm{m^2}}\right]$
$\boldsymbol{i_l}$	Liquid-phase (electrolyte) current density $\left[\frac{\mathrm{A}}{\mathrm{m^2}}\right]$
$i_{\mathrm{loc},j}$	Local faradaic current density for reaction j $\left[\frac{\mathrm{A}}{\mathrm{m^2}}\right]$
$\boldsymbol{i_m}$	Membrane current density $\left[\frac{\mathrm{A}}{\mathrm{m^2}}\right]$
$\boldsymbol{i_s}$	Solid-phase (electrode) current density $\left[\frac{\mathrm{A}}{\mathrm{m^2}}\right]$
$i_{0,j}$	Exchange current density for redox reaction j $\left[\frac{\mathrm{A}}{\mathrm{m^2}}\right]$
$\boldsymbol{J_i}$	Flux of species i due to diffusion and migration $\left[\frac{\mathrm{mol}}{\mathrm{m^2 \cdot s}}\right]$

$J_{\mathrm{TEOA,0}}$	Magnitude of flux of TEOA across membrane $\left[\frac{\mathrm{mol}}{\mathrm{m}^2\cdot\mathrm{s}}\right]$
k_{chem}	Rate constant for chemical oxidation of TEOA $\left[\frac{L^{2.25}}{\mathrm{mol}^{2.25}\cdot\mathrm{min}}\right]$
k_j^o	Standard rate constant for redox reaction j $\left[\frac{\mathrm{m}}{\mathrm{s}}\right]$
$n_{e,j}$	Number of electrons transferred in redox reaction j
$\boldsymbol{N_i}$	Total flux of species i $\left[\frac{\mathrm{mol}}{\mathrm{m}^2\cdot\mathrm{s}}\right]$
$\boldsymbol{N_{i,\mathrm{con}}}$	Convective flux of species i $\left[\frac{\mathrm{mol}}{\mathrm{m}^2\cdot\mathrm{s}}\right]$
$\boldsymbol{N_{i,\mathrm{diff}}}$	Diffusive flux of species i $\left[\frac{\mathrm{mol}}{\mathrm{m}^2\cdot\mathrm{s}}\right]$
$\boldsymbol{N_{i,\mathrm{mig}}}$	Migration flux of species i $\left[\frac{\mathrm{mol}}{\mathrm{m}^2\cdot\mathrm{s}}\right]$
P	Permeation coefficient of TEOA $\left[\frac{\mathrm{m}^2}{\mathrm{s}}\right]$
Q	Electrolyte volumetric flow rate per electrode $\left[\frac{\mathrm{m}^3}{\mathrm{s}}\right]$
$r_{\mathrm{Fe(III)\text{-}CN}}$	Rate of generation of ferricyanide by chemical reaction $\left[\frac{\mathrm{mol}}{\mathrm{m}^3\cdot\mathrm{s}}\right]$
$R_{i,j}$	Rate of generation of species i by electrochemical reaction j $\left[\frac{\mathrm{mol}}{\mathrm{m}^3\cdot\mathrm{s}}\right]$
SOC	State of charge
T	Temperature $[\mathrm{K}]$
$\boldsymbol{u}$	Electrolyte velocity $\left[\frac{\mathrm{m}}{\mathrm{s}}\right]$
$u_{m,i}$	Liquid-phase ionic mobility of species i $\left[\frac{\mathrm{mol}\cdot\mathrm{m}^2}{\mathrm{J}\cdot\mathrm{s}}\right]$
$\Delta V_{\mathrm{electrolyte}}$	Ohmic voltage drop across electrolyte $[\mathrm{V}]$
V_{tank}	Electrolyte tank volume $[\mathrm{m}^3]$
z_i	Charge of ionic species i
α_j	Transfer coefficient for redox reaction j
ϵ	Porosity
η_j	Activation overpotential for redox reaction j $[\mathrm{V}]$

κ	Electrolyte conductivity $\left[\frac{\mathrm{S}}{\mathrm{m}}\right]$
$\nu_{i,j}$	Stoichiometric coefficient for species i in reaction j
σ_e	Electrode conductivity $\left[\frac{\mathrm{S}}{\mathrm{m}}\right]$
σ_m	Membrane conductivity $\left[\frac{\mathrm{S}}{\mathrm{m}}\right]$
ϕ_l	Liquid-phase (electrolyte) potential $[\mathrm{V}]$
ϕ_m	Membrane electric potential $[\mathrm{V}]$
ϕ_s	Solid-phase electric potential $[\mathrm{V}]$

Constants

F	Faraday constant $\left[\frac{\mathrm{C}}{\mathrm{mol}}\right]$
R	Gas constant $\left[\frac{\mathrm{J}}{\mathrm{mol \cdot K}}\right]$

Common Subscripts and Superscripts

ct	Charge-transfer (faradaic) reaction
eff	Porosity-corrected effective value
elec	Electrolyte phase
initial	Initialized value
l	Liquid (electrolyte) phase
mem	Membrane
nct	Non-charge-transfer reaction
neg	Negative electrode, negative electrolyte, primary negative redox reaction
pos	Positive electrode, positive electrolyte, primary positive redox reaction
s	Solid (electrolyte) phase
total	Total over all oxidation states
xx	Through-plane
yy	In-plane

1 Introduction

The global energy landscape is currently evolving due to sustainability and climate change concerns from both policymakers and the public. The effort to reduce our dependence on fossil fuels for energy production has necessitated the development and utilization of renewable and non-carbon-emitting energy generation technologies. Many such technologies to address this demand exist, but face a number of drawbacks. Nuclear energy is capable of high constant power output, but its output cannot be easily reduced or increased to adapt to short-term fluctuations in demand.[1] In addition, the hazards and costs associated with nuclear power plants and storage of their long-lived radioactive waste can make them undesirable to residents in their vicinity.[2] Photovoltaic solar energy is a popular and renewable power source but suffers due to the intermittency of its output; energy production does not occur at night and during periods of low sunlight. Wind energy is another popular, but intermittent, source of renewable energy since it obviously cannot be produced when little or no wind occurs.

Overcoming the intermittent nature of wind and solar energy production would likely improve the feasibility of their widespread adoption and inclusion into the energy supply mix. This could be accomplished with the implementation of energy storage technologies capable of storing renewable energy as it is generated and releasing it as needed. Beyond increasing the exploitation of these renewable sources, grid energy storage can play a role in improving the economics of power generation by storing electricity during off-peak times when demand is lower and then releasing electricity during peak times when demand is higher. Pumped hydro-energy is currently the dominant technology for energy storage for use in the electrical grid. It operates by using electricity to pump water to an elevated reservoir where its potential energy can later be extracted using a hydroelectric generator.[3] This method of energy storage is limited by geographical constraints since it requires existing hydroelectric infrastructure to be available. Electrochemical energy storage technologies such as batteries are also

currently used in grid storage applications. In the United States, installed capacity for large-scale battery storage was 869 MW at the end of 2018.[4] In Canada, the installed capacity for grid battery storage was estimated at 26.4 MW in 2019. Lead-acid batteries have been the most widely used type for these existing energy storage applications. Other battery-based storage systems include lithium-based, sodium-nickel-chloride, and sodium-sulfur batteries.[5] These electrochemical systems can reliably store and produce electrical power directly. A variety of other technologies that are not as widely used for grid energy storage include flywheels, compressed air storage, hydrogen storage, and power-to-gas storage.[1,6–8]

Conventional batteries that are used in grid applications are hindered by the fact that scale-up of their power capacity is strongly coupled to the scale-up of their energy capacity. The typical configuration of a battery system consists of several cells connected in series to achieve a desired voltage and many such sets connected in parallel to achieve a desired power output capacity. A battery can thus be thought of as an array of connected cells. The energy capacity of a cell depends on its volume and the concentration of the electrochemical species contained within it. The cell is also constrained by properties such as electrode kinetics, thickness, porosity, and area with respect to its maximum power output.[9–11] The consequence of these characteristics is that the maximum power output of a conventional battery is coupled to its energy capacity. Thus, in many practical situations, either the power output or energy capacity must be overdesigned. This can result in higher costs due to unnecessary electrochemical reactants or electrode materials, which can affect the economic feasibility of such storage systems. Redox flow batteries have been investigated as a potential solution to this drawback.

As in the case of conventional batteries, redox flow batteries use electrical energy to drive electrochemical reactions at electrodes and vice versa. What differentiates redox flow batteries is that

they operate as flowing systems, with the electroactive species contained in an electrolyte that flow between storage tanks and electrodes. A schematic for a typical all-vanadium redox flow battery is shown in Figure 1.1.

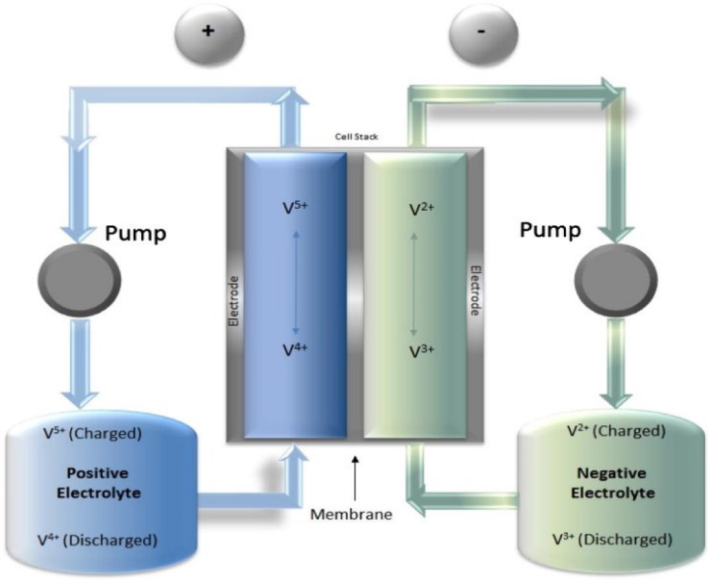

Figure 1.1: Schematic of a typical redox flow battery. Reproduced from Lucas and Chondrogiannis[12] with permission from Elsevier.

At each electrode, electrochemical reactions either store energy in the battery or extract energy from the battery. The properties of the electrode, electrode reactions and operating conditions determine the maximum power output of the battery. The energy capacity, on the other hand, is determined entirely by the volume of the electrolyte and concentration of electroactive species. Consequently, the parameters that affect the energy capacity and power output are decoupled in a redox flow battery.[13] This has the potential to make flow battery systems more attractive than their conventional alternatives in large-scale applications such as grid energy storage. Redox flow batteries have been deemed feasible for a variety of on-grid and off-grid energy storage applications, particularly in tandem with renewable energy from such sources as wind and solar.[13–16] Redox flow battery stacks do not have high energy densities in comparison to many conventional batteries such as lithium-ion and are thus better suited to

large-scale stationary applications such as grid energy storage, where a larger size is less of a drawback.[13]

Redox flow batteries use redox reactions to store and extract electrical energy from chemical reactants similar to those of other batteries. Several different combinations of redox reactions have been investigated for flow battery applications. Factors influencing the effectiveness of redox reactions used in flow batteries include reactant safety, electrode material, cell potential, side reactions, cost of battery materials and reactants, coulombic efficiency, and energy efficiency. Many of the aqueous-based redox reactions that have been considered for use in flow batteries involve transition metals, frequently in acidic electrolytes to maintain their solubility. A drawback to using an acidic electrolyte is the fact that this facilitates the hydrogen evolution reaction (HER) at the negative electrode during charge. With respect to redox flow batteries, hydrogen evolution is considered an undesirable side reaction; protons are reduced to hydrogen gas, consuming electrons that would otherwise go to the desired redox reaction(s). Since the hydrogen gas cannot be oxidized back to protons by the electrode during discharge, the charge consumed by the HER is not recoverable and constitutes a loss of current efficiency (CE), which is defined as the ratio of the charge transferred from the battery during discharge to the amount originally transferred to the battery during charge.

The transition metals used in redox flow batteries can be expensive, resulting in significant up-front capital costs when assembling these batteries in large-scale installations. This cost consideration is an important factor in determining the commercial feasibility of different redox reactions in flow battery applications. Not surprisingly, efforts have been made to use relatively inexpensive and abundant redox species, such as iron. Iron-based flow batteries have an advantage over many other redox flow batteries with respect to the electrolyte cost, a significant component of the initial capital cost for battery installation.

An all-iron, all-aqueous, redox flow battery has recently been developed and studied by Gong et al.[17] This battery system makes use of iron-cyanide and iron-triethanolamine redox couples at the positive and negative electrodes, respectively, as shown in eqs (1.1) and (1.2). The formal potentials for the two reactions determined by Gong et al.[17] are also provided below. It should also be noted that TEOA refers to triethanolamine ($(CH_2OHCH_2)_3N$) in eq (1.2).

$$[\mathrm{Fe(CN)_6}]^{3-} + e^- \rightleftharpoons [\mathrm{Fe(CN)_6}]^{4-} \qquad E^{o'} = 0.48\mathrm{V\ (SHE)} \qquad (1.1)$$

$$[\mathrm{Fe(TEOA)(OH)}]^{-} + e^- \rightleftharpoons [\mathrm{Fe(TEOA)(OH)}]^{2-} \qquad E^{o'} = -0.86\mathrm{V\ (SHE)} \qquad (1.2)$$

This system has a number of advantages that make it attractive as a potential energy storage technology. First, this battery operates with redox reactions that involve iron complexes in alkaline electrolytes. The high pH of the electrolytes greatly reduces the danger of hydrogen evolution as a side reaction, resulting in relatively high current efficiency. Additionally, as an iron-based redox flow battery, this system does not require relatively expensive and scarce metals such as vanadium or cerium in its electrolyte. Furthermore, unlike many other all-iron redox flow batteries, the system proposed by Gong et al.[17] is not a hybrid flow battery; solid metal deposition and dissolution do not take place, allowing for complete decoupling of the power and energy capacities. Finally, the fast electrode kinetics of both redox couples removes the need for catalysts and enable the usage of simple carbon paper electrodes. These advantages make a case for further research and development of this flow battery technology. Modelling of this battery system constitutes one such area of research that can be used to better understand it. Such a model would help provide a qualitative understanding of the underlying mechanisms and phenomena that affect battery performance, as well as the quantitative effects of operating conditions and system parameters on the battery performance.

Redox flow batteries can be modelled using many of the same equations that apply to conventional battery systems. Numerical methods such as the finite element method (FEM) can be used to solve the

system of partial differential equations that describe the operation of flow battery systems. Models that accurately describe the behaviour of chemical systems such as flow batteries are valuable as they allow operators and engineers to design and simulate these systems under various operating conditions. The primary objective of the present work is the formulation and validation of a Multiphysics model for the novel all-iron all-soluble aqueous RFB that has been developed by Gong et al.[17] While many RFB models exist for other RFB systems, as described in Chapter 3, no existing models for this recently-developed and attractive system have been reported. Lower-level objectives of the work include determination of the side reactions that occur and how they can be modelled, fitting of parameter values, and analysis of system behaviour such as potential and concentration profiles. The present work details the development and numerical solution of a model for the redox flow battery presented by Gong et al.,[17] implemented in the COMSOL Multiphysics FEM software.

Chapter 2 provides a basic primer on RFB systems, focusing on how they operate and how they are characterized. Chapter 3 provides a review of the available literature regarding the state-of-the-art for RFB systems and models, including literature relating to the present RFB system. Chapter 4 outlines the model formulation, theory, and assumptions. This includes constitutive equations and boundary conditions, as well as FEM solver and meshing details. Chapter 5 discusses the many model parameters and how their values are obtained. Chapter 6 presents the major results of the model including its fit to the experimental data, spatial profiles for reactant concentration and potentials, and cycling behaviour. Chapter 7 states the conclusions of the work and makes recommendations for further development of both the model and the RFB system.

2 Background

2.1 Redox Flow Battery Operation

2.1.1 Redox Flow Battery Components

During discharge of an RFB, spontaneous redox reactions at the two electrodes cause electrical current to flow through an external circuit; during charge, electrical energy is supplied to drive the redox reactions in the reverse direction so that the discharge cycle can be repeated. A redox flow battery is made up of several components, which can differ somewhat depending on the type of battery. Figure 2.1 presents a more detailed schematic of a typical all-vanadium RFB.

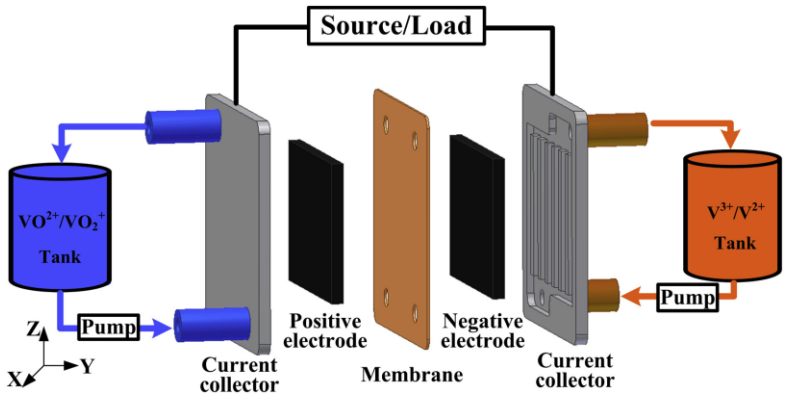

Figure 2.1: Detailed schematic of all-vanadium RFB. Reproduced from Yin et al.[18] with permission from Elsevier.

A soluble aqueous redox flow battery system, such as the one described in the present work, is a 2-compartment cell that typically consists of porous electrodes, current collectors, ion exchange membrane, electrolytes, tanks, pumps, and tubing. The positive and negative electrolytes are aqueous solutions of the reactants and additives necessary for the redox reactions to proceed at the positive and negative electrodes, respectively. The porous electrodes are the components of the RFB where the reduction and oxidation reactions occur; electrons flow between each electrode and its associated

reactants, resulting in oxidation or reduction of the reactants during charge and discharge. Each porous electrode makes electrical contact with a current collector, allowing the electrons to flow into and out of the electrodes from the external circuit during charge and discharge. Both electrolytes are stored in separate tanks and pumped through tubing into the inlets of their corresponding electrodes. Each electrolyte flows through a porous electrode, undergoing redox reactions before leaving through an outlet and being pumped back into their storage tank. Sometimes, the current collectors are designed with three-dimensional indentation patterns that serve as channels to influence the flow of electrolyte through the battery and enhance battery performance.[18] In some systems, these flow channels are instead imparted into bipolar plates that are fixed between the current collectors and porous electrodes.[19] The ion exchange membrane separates the positive and negative electrolytes and blocks most ions from crossing over from one side to the other while allowing the selective permeation of certain charge carriers to carry the current through the battery. These ion exchange membranes can generally be categorized as cation-exchange membranes (CEM) and anion-exchange membranes (AEM). Cation-exchange membranes such as Nafion are frequently used in RFB applications, particularly under acidic conditions. These membranes contain fixed negatively-charged functional groups that are intended to allow the passage of cations, typically protons. Anion-exchange membranes are not as widely used in RFB applications, although their use has become more common in recent years since they have some advantages over CEMs, such as lower crossover of undesired redox species.[20]

2.1.2 Charge and Discharge

In a redox flow battery, the main half-cell reactions at each electrode determine which electrode is positive and which electrode is negative. The half-cell reaction at the positive electrode operates at a more positive potential than that of the negative electrode reaction, indicating that the redox species at the positive electrode has a greater tendency to undergo reduction; conversely, the redox species at the

negative electrode has a greater tendency to undergo oxidation. When the two half-cell reactions occur together within a battery, a potential difference exists across the electrodes as a result of this difference in tendency to undergo reduction or oxidation. During discharge, the electrode reactions proceed spontaneously in their thermodynamically favoured directions: the positive electrode reaction proceeds cathodically and the negative electrode reaction proceeds anodically. The favourable thermodynamics enables electrical energy to be extracted from the system and utilized on an electrical load. During charge of the battery, the two main half-cell reactions are each driven in the direction opposite to that during discharge; the reaction with the higher potential is oxidized during charge, while the reaction with the lower potential is reduced. An external supply of electrical energy is required to drive these reactions since they are thermodynamically unfavourable and do not occur spontaneously.

2.1.3 Operating Conditions

The operating conditions of redox flow batteries can vary widely depending on the particular chemistry and application. Several operating parameters are applied to control the behaviour of flow battery systems, including the mode and current density during charge-discharge cycling, electrolyte volumes and flow rates, and operating temperature.

Charge and discharge of redox flow batteries can be carried out using either galvanostatic and/or potentiostatic modes.[21–23] When a battery is charged and discharged in the galvanostatic mode, the current is the controlled input and voltage is the monitored output. Galvanostatic charge curves are usually generated during the characterization of redox flow batteries. When a battery is charged and discharged in the potentiostatic mode, the cell voltage is the controlled input and current is the monitored output. This mode of operation is less common, but is still used in some RFB research, especially as an addition to galvanostatic cycling. Galvanostatic cycles are usually described in terms of the applied current density (or current) at which the battery is charged and discharged and the length of

charge and discharge, as controlled by the duration of time or specific charge/discharge voltage thresholds. Threshold voltages correspond to the maximum and minimum allowable voltages to which the battery can be charged and discharged, respectively. Under this scheme, the RFB is charged at a constant current until its voltage reaches an upper threshold, at which point the battery is discharged at the same current magnitude until its voltage reaches the lower discharge threshold.

The capacity of a redox flow battery is determined by the quantity of redox species present in each electrolyte, which depends on the electrolyte volume and concentrations of redox species. Physical and chemical considerations such as solubility and complexation efficacy typically limit the maximum concentration of redox species possible in each electrolyte; thus, the maximum capacity of a redox flow battery primarily scales with electrolyte volume. More electrolyte volume allows for longer charge and discharge times at a given current density.

The most fundamental difference in the operation of an RFB from that of a conventional rechargeable stationary battery is that electrolytes circulate through them from external reservoirs. The electrolyte flow rate is an operating parameter that affects both the transport of reactants in the battery and the overall efficiency of the RFB. A high flow rate of electrolyte reduces the gradient of reactant concentrations across the length of the electrodes, while a low electrolyte flow rate enables more depletion of reactant due to the longer residence time of the electrolyte in each electrode. As electrolyte flow rate increases, the pressure drop across each electrode also increases; consequently, the power required to pump the electrolyte increases as well. The more power required to pump the electrolyte, the lower the efficiency of the battery.

Redox flow batteries may be operated at different temperatures to optimize performance[24] or as a result of their utilization in different climates and seasons.[25–27] The operating temperature of a flow

battery has an impact on many of the physical properties of the system, including the diffusion and reaction rates, conductivity of the electrolytes and the equilibrium potentials of the redox couples.

2.2 Redox Flow Battery Characterization

Several techniques are frequently used to characterize redox flow batteries in research. Parameters of interest and data that are obtained from such measurements include half-cell kinetics, diffusion rates of redox species, formal potentials, cell efficiencies, polarization behaviour, and cycle life.

2.2.1 Half-Cell Kinetics

The rate of a redox or half-cell reaction is dependent on the electrode potential, which is the difference between the electric potential on the solid side of the electrode and the potential in the electrolyte adjacent to the electrode. If the electrode potential is made more positive than the equilibrium potential of a half-cell reaction, thermodynamics dictates that the reaction proceeds in the anodic direction. If the electrode potential is decreased below the equilibrium potential, the reaction proceeds in the cathodic direction. The more the electrode potential is increased or decreased, the more the rate of the oxidation or reduction reaction increases, resulting in a larger magnitude of current density through the electrode. Half-cell kinetics refers to the relationship between electrode potential and redox current density for a given redox reaction. Obviously, the kinetics of both the intended charge-transfer reactions and any side reactions play important roles in the performance of an RFB. The Butler-Volmer and Tafel equations are two examples of models that are used to describe electrode kinetics. The Tafel equation is a special case of the more general Butler-Volmer equation that applies when the overpotential is relatively high. A number of methods can be employed to characterize electrode kinetics, such as chronoamperometry,[28] chronopotentiometry,[28] square-wave voltammetry,[29] and cyclic voltammetry.[30]

2.2.2 Redox Species Transport

The transport of redox species through an electrolyte phase in a redox flow battery occurs by three mechanisms: diffusion, convection, and migration. The conservation of a charged species in a porous electrode can be expressed by eqs (2.1) and (2.2):

$$\frac{\partial(\epsilon c_i)}{\partial t} + \nabla \cdot \boldsymbol{N_i} = \sum_j \epsilon R_{i,j} \tag{2.1}$$

$$\boldsymbol{N_i} = \boldsymbol{N_{i,\mathrm{diff}}} + \boldsymbol{N_{i,\mathrm{mig}}} + \boldsymbol{N_{i,\mathrm{con}}} \tag{2.2}$$

The diffusive flux for a given species is dependent on the product of its concentration gradient and effective diffusion coefficient, as described by Fick's Law in eq (2.3).

$$\boldsymbol{N_{i,\mathrm{diff}}} = -D_{i,\mathrm{eff}} \nabla c_i \tag{2.3}$$

A larger concentration gradient leads to a faster rate of diffusion. Diffusion coefficients can be measured using cyclic voltammetry and the Randles-Sevcik equation, which describes the relationship between scan rate and peak current.

In RFB systems, convection is usually a significant mode of reactant transport since the electrolyte is pumped through the battery. The convective flux of a given species is determined by the product of its concentration and the electrolyte velocity, as described in eq (2.4).

$$\boldsymbol{N_{i,\mathrm{con}}} = \boldsymbol{u} c_i \tag{2.4}$$

The velocity profile in a redox flow battery depends on many system parameters. Depending on the flow conditions, different models such as Darcy's law, the Brinkman equations, or the Navier-Stokes equations may be utilized to determine the velocity profiles in an RFB system.

Migration refers to the motion of electrically charged species in an electric field that is present in a redox flow battery. Migration of charged species depends on the product of the electric potential

gradient, species concentration, ionic mobility, and species charge. The migration flux is described by eq (2.5).

$$\boldsymbol{N}_{i,\mathbf{mig}} = -z_i u_{m,i,\text{eff}} F c_i \nabla \phi_l \tag{2.5}$$

The electric potential gradient $\nabla \phi_l$ within an electrolyte is the driving force for migration, analogous to the concentration gradient for diffusive transport; thus, a steeper potential gradient leads to faster migration of a charged species. Also, the higher the concentration, mobility $u_{m,i,\text{eff}}$ and/or charge z_i of an ion, the more rapid is migration through an electrolyte.

A more comprehensive and detailed discussion of the equations and boundary conditions related to reactant transport in porous electrodes is included in Chapter 4.

2.2.3 Formal Potential

The equilibrium potential of a redox couple depends on the chemical activity of each species involved in the half-cell; this relationship is described by the Nernst equation, which makes use of a standard reduction potential. Since it is typically easier to work with species concentrations than activities, the activity coefficients can be separated from the concentration-dependent term in the Nernst equation, resulting in a form of the Nernst equation that is expressed in terms of species concentrations. In this form of the Nernst equation, the standard potential and the contribution of the activity coefficients are combined into a new term known as the formal potential. Using the Nernst equation with a formal potential, the equilibrium potential of a redox couple can be conveniently estimated from the species concentrations. In practice, the activity coefficients vary with concentration, so this form of the Nernst equation provides only an approximation for the equilibrium potential of a redox couple. In RFB studies, formal potentials are often reported for the redox couples used for each electrode. Half-cell formal

potentials are typically estimated to be equal to the half-wave potential obtained from cyclic voltammetry.[31]

2.2.4 Efficiency

The purpose of redox flow battery systems is the storage and subsequent reuse of electrical energy. Consequently, the efficiency of this process is crucial in evaluating the feasibility of a given RFB with respect to a proposed application. Three types of efficiency are commonly reported for redox flow batteries that aim to characterize different battery losses: current efficiency, voltage efficiency, and energy efficiency. These efficiencies may be defined for a single charge-discharge cycle or a sequence of cycles to determine how they change over time with continued operation of the RFB.

The current efficiency is the fraction of charge transferred to the battery during charge that is recovered during the subsequent discharge process. Current efficiency losses are generally caused by side reactions that consume current during charge but are not reversed during discharge, resulting in a loss of recoverable charge. In acidic redox flow batteries, the reduction of H^+ to hydrogen gas is a frequent cause of reduced current efficiency.

The voltage efficiency corresponds to the ratio of average battery voltage during discharge to the average battery voltage during charge. A number of losses cause the battery voltage to be higher during charge than discharge. One of these is the activation overpotential, which is the difference between the electrode potential and the equilibrium potential due to barriers associated with the electrode kinetics of a redox reaction. This component increases with current density. The activation overpotential always constitutes a loss of voltage efficiency in a battery at both electrodes and during both charge and discharge. In addition to activation overpotential, ohmic losses are responsible for reduced voltage efficiency. Ohmic losses occur as a consequence of the resistance to charge transport in a specific medium and irreversibly convert electrical energy to heat. Ohmic losses can occur across electrodes,

current collectors, electrolytes, and membranes and are generally proportional to the operating current of an RFB, assuming that resistances remain constant. The ohmic resistance across an electrolyte is dependent on its conductivity κ, inter-electrode spacing $d_{\text{electrolyte}}$ and electrode area $A_{\text{electrode}}$. The expression given below in eq (2.6) corresponds to the case of 1-dimensional current flowing between two planar electrodes with the same area. This expression shows that lower resistance is favoured by higher conductivity, larger electrode area, and smaller inter-electrode spacing. The voltage drop due to this resistance is equal to the product of the electrolyte current and resistance.

$$R_{\text{electrolyte}} = \frac{d_{\text{electrolyte}}}{\kappa A_{\text{electrode}}} \tag{2.6}$$

The voltage drop across a membrane can often be modelled as being simply ohmic, but more comprehensive models make use of more advanced transport mechanisms, such as those involved in electrolytes. Resistance to transport of reactants to and from the electrodes can also lead to voltage losses during charge and discharge, known as concentration overpotential, when reactant concentration at an electrode surface differs from its concentration in the bulk electrolyte. The concentration overpotential becomes especially significant when operating at higher current densities.[32,33]

Energy efficiency is a good overall measure of the capability of an RFB to perform its intended function of energy storage. This efficiency metric is the ratio of energy extracted during discharge to the energy input during charge. The energy efficiency of an RFB is equivalent to the product of the charge and voltage efficiencies. While the energy efficiency is a good overall measure of the performance of an RFB, the current and voltage efficiencies are more useful for identifying specific problems and potential for further improvement. An RFB with a low voltage efficiency may have sluggish kinetics, poor electrical contact between components, high membrane resistance to charge carriers, or any combination of these problems. When an RFB exhibits low current efficiency, it can usually be attributed to irreversible

side reactions. The first step to identifying these problems often begins with the determination of these efficiencies.

2.2.5 Polarization Plots

Since it is important to determine the optimum operating current for an RFB, it is useful to obtain its polarization curve. Polarization curves, which are routinely used to characterize other batteries and fuel cells, display the cell voltage as a function of operating current density; they can be used to identify the source of the voltage losses that are dominant at different current densities. As shown in Figure 2.2, losses due to activation overpotential are dominant at lower current densities. However, at intermediate current densities, the situation begins to change and ohmic losses now overtake the activation losses. Eventually, when the current density becomes high enough, transport of redox species to/from the electrode begins to have an impact and eventually becomes the main factor limiting battery performance.

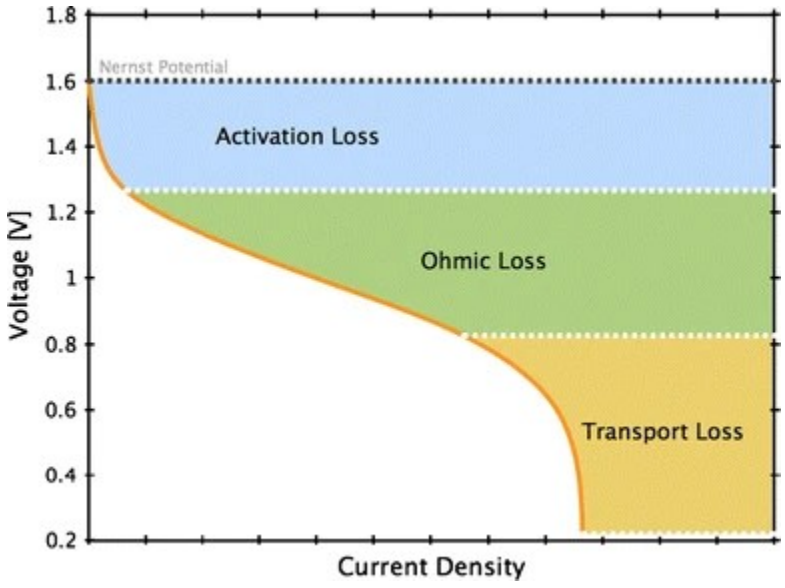

Figure 2.2: Polarization plot for a typical RFB. Reproduced from Aaron et al.[34] with permission from Springer.

2.2.6 Cycle Life

In order to be successfully deployed for grid storage applications, RFBs should be capable of operating for many charge-discharge cycles without performance deterioration to be competitive with existing energy storage technologies. For this reason, it is very common for studies to include an evaluation of the cycle life and capacity fade of the battery system. In these experiments, the RFB is subjected to a number of repeated charge-discharge cycles either for a constant period of time or between some pre-determined threshold voltages, while the resulting battery voltage is monitored. The various efficiencies of the RFB may be determined during each cycle to monitor any changes in the battery performance over time. The occurrence of side reactions and other undesirable phenomena in the battery may serve to cause an imbalance between the redox species concentrations in the two electrolytes, leading to a reduction in charge capacity that is known as capacity fade. Rebalancing of RFB systems, whereby the concentrations of the reactants in the electrolytes are adjusted to counteract the imbalance and reduce capacity fade, is an area of ongoing research that has resulted in a number of patents.[35-40]

3 Literature Review

3.1 Redox Flow Battery Development

3.1.1 Conventional Soluble Metal RFBs

Redox flow batteries have been investigated for many decades after their concept was first patented in the late 1940s.[41,42] Early redox flow batteries such as the iron-chromium system made use of redox couples consisting of multivalent transition metal ions.[43] While the iron-chromium RFB is still being actively studied,[44,45] numerous other aqueous electrolytes based on metal cations have been investigated as alternatives. These conventional aqueous redox flow batteries do not typically undergo phase changes, with the reactions occurring homogeneously in the liquid phase within porous electrodes. Recently, iron-chromium RFBs have been able to achieve energy efficiencies as high as 80.5% at 480 mA/cm^2 with high electrode compression resulting in altered porosity and transport properties,[46] as high as 80.7% at a current density of 320 mA/cm^2 using interdigitated flow fields,[47] and as high as 79.6% at a current density of 200 mA/cm^2 using serpentine flow fields.[48] Other approaches to RFB performance improvement that have been applied to iron-chromium RFB systems include optimizing electrolyte composition and modifying graphite electrodes with SiO_2 which have yielded energy efficiencies of 81.5% and 79.66%, respectively, at 120 mA/cm^2.[49,50] The membrane thickness in the iron-chromium RFB has also been optimized, with the finding that Nafion 212 membranes outperform the thicker Nafion 115 and 117 membranes.[51] The all-vanadium redox flow battery (VRFB), which has been the most heavily studied conventional RFB system, makes use of soluble vanadium in four different oxidation states in the positive and negative electrode reactions. A VRFB that was operated at a very high current density of 600 mA/cm^2 demonstrated very stable operation over the course of 20,000 cycles with an energy efficiency of 80.83%.[52] Research has been conducted on different modified

membranes for VRFBs such as sulfonated poly(ether ether ketone),[53–56] polybenzimidazole,[54,57] metal-organic framework,[58] and anion exchange membranes[55,59] to improve performance. The capacity and efficiencies of VRFBs have also been improved by optimizing electrolyte component concentrations, so as to improve viscosity, conductivity, and electrochemical activity.[60]

Reviews of RFB studies[16,61] have identified other noteworthy half-cell combinations for conventional RFBs including iron-vanadium,[62–64] polysulfide-bromine,[65–68] vanadium-cerium,[69–73] vanadium-bromine,[74,75] iron-titanium,[76,77] and manganese-vanadium.[78,79] Although these RFBs use different half-cell combinations, it can be seen that certain half-cell reactions such as those involving vanadium and iron redox couples have been commonly used in these novel flow batteries.

3.1.2 Hybrid RFBs

In conventional RFB systems, all the electroactive species and additives are soluble species in the liquid phase. In these RFBs, redox species are oxidized and reduced while remaining dissolved in the electrolyte phase. However, hybrid RFB systems operate on the basis of redox reactions involving at least one phase change such as solid metal deposition from the liquid phase and dissolution of solid metal from the liquid phase. With the exception of this phase change, hybrid RFBs function in the same manner as conventional redox flow batteries: electrode reactions occur at each electrode as flowing electrolytes transport reactants and products to and from the electrodes. Examples of redox couples that feature this type of phase change include the Fe^{2+}/Fe(s) and Zn^{2+}/Zn(s) redox couples. It should be noted that one of the consequences of such a phase change is that hybrid RFBs lose one of the advantages of conventional RFBS in that their power and energy are no longer completely decoupled from one another. The deposition of metal onto one or more electrodes modifies the electrode(s); the amount of metal deposited is proportional to the amount of charge, and therefore energy, stored. Although practical hybrid RFBs using planar electrodes are designed so that the phase change reactions

do not cause significant flow problems, the allowable energy capacity of such batteries has a theoretical upper limit that does not exist in conventional RFBs, which is determined by the point at which too much metal is deposited for electrolyte flow to be maintained. Additionally, the use of porous electrodes has been investigated for metal plating in hybrid RFBs and found to lead to some flow problems due to the deposition.[80,81] The amount of metal that can be deposited depends on the size of the electrode; a larger electrode is able to support more metal deposition without significant loss of performance than a smaller electrode. For this reason, the size of an electrode intended for metal deposition has constraints based on energy capacity as well as power capacity; this differs from conventional RFBs, where the energy density is determined entirely by the size of the electrolyte storage tanks and solubility of the electroactive species, both of which have no effect on its power density. An additional difference between conventional RFBs and hybrid RFBs is the difference in available flow configurations. While conventional RFBs typically employ porous flow-through electrodes, where the electrolyte can flow through the pores in the electrode itself, hybrid RFBs may use porous or non-porous electrodes for the plating reaction.[82] A non-porous planar electrode does not allow the flow of electrolyte through it, but instead allows the deposition of metal on its outer surface during the redox process. Hybrid RFBs that have attracted considerable attention include zinc-cerium,[83–94] zinc-bromine,[95–100] vanadium-air,[101–105] all-iron,[15,106–108] and soluble lead-acid batteries.[109–117]

3.2 Redox Flow Battery Models

Redox flow battery modelling is an active field of research that aims to accurately simulate and optimize redox flow battery systems for their eventual design and operation. The models developed to date differ greatly with respect to their depth and accuracy; models that consider more detailed and comprehensive descriptions of phenomena occurring in an RFB can generally be expected to have greater accuracy at the expense of more computational effort. As more detailed experimental studies

are carried out on particular redox couple combinations, more comprehensive and hopefully accurate models can be developed based on the observations of their behaviour.

3.2.1 Types of RFB Models

The models for redox flow batteries can be classified based on their spatial dimensionality: zero-dimensional (0D), one-dimensional (1D), two-dimensional (2D), and three-dimensional (3D). The dimensionality chosen for a model depends on the objectives and constraints of the study. For example, if research is being conducted on the performance of three-dimensional flow field designs then a 3D model is necessary, while the same 3D model may be unnecessary for the simulation of a stack of RFBs. RFB models may further be distinguished from one another based on whether they are dynamic or quasi-steady state. The latter makes use of the approximation that the change in reactant concentrations is gradual enough that transient terms can be assumed negligible in the transport equations, making the model quasi-steady state.[118] Since this assumption has the potential to introduce error during transient phenomena that occur during charge and discharge, dynamic models are generally used for RFB modelling.

3.2.2 Early Models

The zinc-bromine hybrid flow battery was among the first to be modelled in the 1980s with one- and two-dimensional models based on steady state transport equations.[119] Although simple 0D stack models were used for scale-up of other RFBs as early as the 1990s,[120] such models do not directly consider the transport and reaction processes taking place in these batteries; they instead model the RFBs as circuit elements. Other early models that explicitly consider the various electrochemical phenomena taking place in RFBs include transient 0D models of the VRFB,[121,122] a quasi-steady state 2D model of the VRFB,[123] and a transient 2D model of the VRFB[124] that was subsequently improved by taking into account the hydrogen evolution side reaction at the negative electrode,[125] consideration of non-isothermal

conditions[126] and the oxygen evolution side reaction at the positive electrode.[127] An early example of a model developed for a non-vanadium RFB was a transient 1D model for the polysulfide-bromine RFB.[128] Since these early models, many more models have been developed for the VRFB system.[129–135] A few other models have also been developed for less popular redox flow batteries. These include a 0D model of an iron-vanadium RFB,[136] 2D models of vanadium-cerium,[137] iron-vanadium,[138] zinc-bromine,[139] iron-air[140] RFBs, and a 3D model of an all-copper RFB.[141]

3.2.3 Thermal and Non-Isothermal Models

A simplifying assumption that is often used in RFB models is that of isothermal operating conditions. The operating temperature of an RFB affects several properties such as the conductivity of the electrolytes and kinetic parameters of the redox reactions. Obviously, this alters the current and voltage efficiencies and RFB performance.[24] The ohmic (resistive) losses in an RFB system dissipate some of the electrical energy as heat, which in turn raises the electrolyte temperature. As an RFB can be expected to heat up over the course of operation, it is important to characterize its thermal behaviour, including the spatial variance and temporal evolution of temperature. For this reason, non-isothermal battery and thermal models have been developed for VRFBs and VRFB stacks; these include transient 2D models,[126,127,142] transient 3D models,[143,144] quasi-steady state 3D models,[145] and 0D models.[26,146–148] A thermal model has been developed to describe the thermal behaviour of a VRFB stack during standby as a result of self-discharge.[146] Another VRFB model was developed to describe a system with forced cooling through heat exchangers.[148]

3.2.4 Flow and Geometry-Dependent Models

The flow of electrolytes through RFB systems is a sub-topic in this field of research that has received a fair amount of attention, particularly with respect to flow field and electrode geometry. In the simplest flow configuration, the electrolyte enters through an inlet into the electrode and is discharged from an

outlet. To improve this design, some RFBs have been developed with three-dimensional channels that form specific flow fields for the electrolyte. Two common channel patterns that have been used are serpentine and interdigitated. Quasi-steady state 2D models have been developed for VRFBs with interdigitated flow fields.[149,150] Quasi-steady state 3D models have also been developed for VRFBs with interdigitated flow fields.[18,151] A quasi-steady state 2D model was developed for electrolyte flow through a VRFB with a serpentine flow field.[152] A quasi-steady state 3D model for a VRFB with a serpentine flow field has also been investigated.[153] 3D quasi-steady state models for VRFBs have also been used to compare interdigitated and serpentine flow fields[154] and compare serpentine and parallel flow fields.[118] Electrode compression is another phenomenon that has been considered in some models; this can be important since porous electrodes can be compressible so that properties such as pore volume and conductivity can vary depending on the degree to which they are compressed.[155] Several 2D[149,156] and 3D[153] VFRB models have considered the effects of electrode compression in their formulation. In most RFB models, porous electrodes are approximated as homogeneous domains to greatly reduce complexity and simplify their calculations. This assumption has been relaxed in some models in which the domain is considered to be a three-dimensional porous structure. Such models are known as pore-scale models and allow for more detailed modelling transport phenomena within the porous electrode domain. 3D pore-scale models for the VRFB[157] and an all-copper RFB[141] have been developed using imaged and stochastically-generated pore geometries, respectively.

3.2.5 Species Crossover and Capacity Fade Models

A challenge that faces many RFB systems is the crossover of ions across the ion exchange membrane. This phenomenon results in self-discharge and capacity fade in RFBs. To simulate capacity fade, several models have been developed that take into account ion and water crossover through the VRFB

membrane, including 2D[156,158,159] and 3D[160] models. Some 0D models also account for one or both of ion crossover and capacity fade in VRFB systems.[26,161–165]

3.2.6 Stack and Equivalent-Circuit Models

Redox flow battery systems can be designed for high power and capacity storage applications by arranging stacks of interconnected redox flow batteries that provide the desired voltage and power to meet requirements. 1D[166] and 2D[142,159] models of RFB stacks have been formulated, but these models become unwieldy due to the computational burden of solving equations that account for both spatial and temporal changes when the total number of cells becomes too large. Stack models are therefore most commonly zero-dimensional.[167–170] Stack models also frequently make the additional simplification of modelling individual RFB units as equivalent circuits that can approximate the current-voltage behaviour of the RFB.[120,171–175] Some stack models are designed to adapt to changing system parameters to provide outputs in real-time.[162,176,177]

3.2.7 Model-Based Optimization

Optimization of RFBs is extremely valuable. Once a model has been appropriately validated, the operating conditions can be modified within applicable ranges to obtain results that would otherwise require experimental measurement. This can lead to better allocation of experimental time and resources, as model outputs can guide further experimental design. Optimization methods such as parametric sweeps and constrained optimization algorithms can be used in conjunction with accurate models to determine optimal parameter values and operating conditions for RFB systems. 2D models have been used to optimize flow geometry and electrode properties in VRFBs with interdigitated flow fields through constrained maximization of discharge voltage with respect to electrode (porosity, thickness, and fiber diameter) and flow channel parameters (channel fraction and pitch) using the

Bound Optimization by Quadratic Approximation (BOBYQA) algorithm.[149] 0D models have been used to optimize VRFB flow rates due to the fact that higher flow rates improve mass transport and decrease concentration overpotential while also increasing pressure losses and pumping energy requirements.[178-180] 0D models have also similarly been used to find the optimal operating flow rates for charging and discharging a larger-scale VRFB stack in order to maximize power delivered by the battery system after pumping losses.[181]

3.3 All-Iron All-Soluble Aqueous Redox Flow Battery

The redox flow battery considered in the present work was developed by Gong et al.[17] and consists of the redox reactions given by eqs (1.1) and (1.2) presented earlier in Chapter 1. The triethanolamine ligand and ferricyanide complex are shown in Figure 3.1.

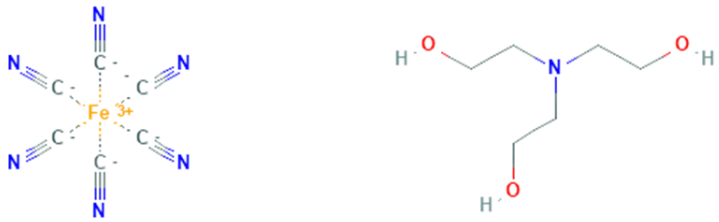

Figure 3.1: Ferricyanide complex (left) and triethanolamine ligand (right). Reproduced from Pubchem.[182,183]

Equation (1.1) gives the half-cell reaction that occurs at the positive electrode: Fe(III)-CN is reduced to Fe(II)-CN during discharge, while the reaction is reversed during charge. Equation (1.2) is the half-cell reaction that occurs at the negative electrode: Fe(II)-TEOA is oxidized to Fe(III)-TEOA during discharge and the reverse occurs during charge. The formal cell voltage produced from these reactions is reported to be 1.34 V.[17] The battery is operated under alkaline conditions in concentrated sodium hydroxide.

Over the course of more than 100 cycles, the RFB was shown to achieve relatively stable energy and voltage efficiencies, with minor fluctuations in current efficiency.[17] This system has not been studied extensively and has not been modelled prior to the present work as it has only recently been developed.

Additional research on the Fe-CN/Fe-TEOA system has been conducted in recent years. In one study, the researchers were able to increase the solubility of iron-triethanolamine to greater than 1.2 mol/L by using a novel synthesis protocol utilizing a 1:1 stoichiometric ratio of iron to triethanolamine in a mixed NaOH/KOH electrolyte, enabling a volumetric battery capacity of approximately 12 Ah/L to be reached.[184] In a recent patent, an improvement to the solubility of iron-cyanide complexes for flow battery applications has been reported using mixed NaOH/KOH electrolytes that achieves iron-cyanide concentrations of up to 1.0 mol/L at 2 mol/L hydroxide concentration.[185] A method to determine TEOA concentrations in solution has been presented in another study and used to determine the concentration of TEOA that was present in the positive electrolyte after crossing the ion exchange membrane in an all-iron all-soluble flow battery.[186]

3.3.1 Fe-CN and Fe-TEOA Redox Couples

The iron-cyanide redox couple has been used in other novel RFBs, including ferri/ferrocyanide-polysulfide,[187] alloxazine-COOH-ferrocyanide,[188,189] zinc-ferricyanide,[190] tetrapyridophenazine/ferrocyanide,[191] anthraquinone-ferrocyanide,[192] BPP-Vi-ferrocyanide,[193] flavin mononucleotide-ferrocyanide,[194] and quinoxaline-ferrocyanide[195] flow batteries. Symmetric cell studies, which utilize the same redox couple at both electrodes in an RFB to determine its operational behaviour in the absence of the other redox couple, have also been conducted on the iron-cyanide redox couple to characterize its stability in alkaline solution over time. One such study found that neutral pH conditions are optimal for the stability of the iron-cyanide redox couple and that significant capacity fade occurs when operated at higher pH. This observation was attributed, at least partially, to decomposition of the

electrolyte itself.[196] However, this explanation was refuted by another group who concluded that the decomposition of the electrolyte did not occur and instead suggested that the capacity fade was caused by the charge imbalance that arises between the two electrodes due to the significant amount of oxygen evolution that occurs as a side reaction at the positive electrode.[197] The iron-triethanolamine redox couple has been used in other novel RFBs, including the Fe-TEOA-Co-TEOA,[198] Co-mTEA-Fe-TEOA,[199] Fe-TEOA-bromine,[200] and Fe-TEOA/K_2MnO_4[201] flow batteries.

This section has thus provided an overview of the state-of-the-art for research into the all-iron all-soluble aqueous RFB system studied in the present work, as well as related systems that make use of its redox couples.

4 Model Formulation

A two-dimensional transient model has been developed for the redox flow battery investigated in the present work. The model was modified from a steady-state version for an all-vanadium redox flow battery available on the COMSOL website. A two-dimensional model was chosen as it contains the minimum dimensionality required to directly account for convective transport of reactants, which is perpendicular to the flow of current and charge-carrying species in the battery. The geometry of the model is shown schematically in Figure 4.1. This geometry consists of three subdomains, each of which is subject to its own set of model equations and boundary conditions. The subdomains consist of a (a) porous negative electrode, (b) Nafion ion exchange membrane and (c) porous positive electrode.

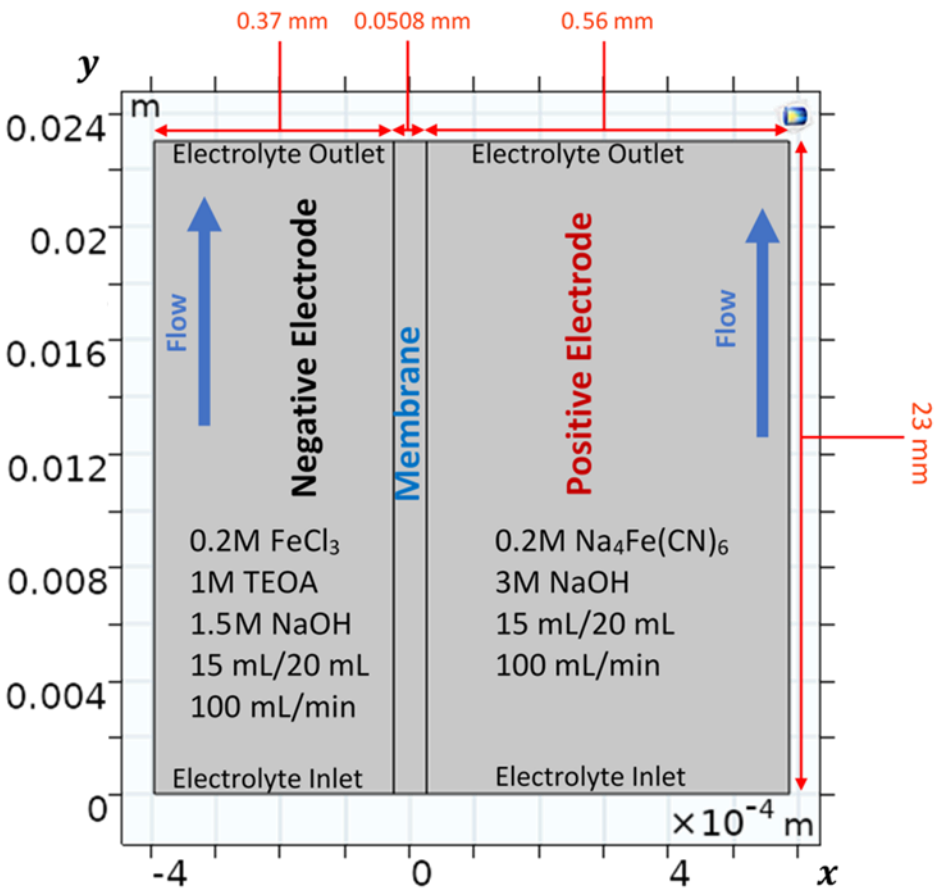

Figure 4.1: The domain of the model is comprised of the (a) negative electrode, (b) ion exchange membrane, and (c) positive electrode subdomains. Each subdomain is drawn as a grey rectangle over the white background. Dimensions and electrolyte compositions are also shown.

Current flow and charge transport occur primarily in the x-direction between the negative and positive electrode subdomains. Convective mass transport within the two electrode subdomains occurs along the y-axis in the positive direction. Diffusive transport can occur in both the x and y directions, while mass transfer due to migration occurs primarily along the x-axis. Although different modes of transport occur predominantly in different directions, the model explicitly considers all charge and mass transport in both the x and y directions within the positive and negative electrode subdomains. The flow battery geometry is defined so that the membrane is centered at zero along the x-axis. The dependent variables of interest within each subdomain are listed in Table 4.1. Throughout the thesis, Fe(III)-TEOA and Fe(II)-TEOA are used as shorthand notation for the species $Fe(TEOA)OH^-$ and $Fe(TEOA)OH^{2-}$, respectively.

Fe(III)-CN and Fe(II)-CN are shorthand notation for $Fe(CN)_6^{3-}$ and $Fe(CN)_6^{4-}$, respectively. The model has been formulated to accommodate battery operation for both a single charge-discharge cycle and repeated charge-discharge cycles.

Table 4.1: Dependent Variables of Model

Negative Electrode	Membrane	Positive Electrode
$c_{\mathrm{Na}}^{\mathrm{neg}}, c_{\mathrm{OH}}^{\mathrm{neg}}, c_{\mathrm{Fe(III)\text{-}TEOA}}^{\mathrm{neg}}, c_{\mathrm{Fe(II)\text{-}TEOA}}^{\mathrm{neg}}, c_{\mathrm{Cl}}^{\mathrm{neg}}, \phi_l^{\mathrm{neg}}, \phi_s^{\mathrm{neg}}$	ϕ_m	$c_{\mathrm{Na}}^{\mathrm{pos}}, c_{\mathrm{OH}}^{\mathrm{pos}}, c_{\mathrm{Fe(III)\text{-}CN}}^{\mathrm{pos}}, c_{\mathrm{Fe(II)\text{-}CN}}^{\mathrm{pos}}, c_{\mathrm{TEOA}}^{\mathrm{pos}}, \phi_l^{\mathrm{pos}}, \phi_s^{\mathrm{pos}}$

4.1 Negative Electrode Subdomain

4.1.1 Constitutive Equations

A porous carbon paper electrode constitutes the entire negative electrode subdomain and is in direct contact with the ion exchange membrane subdomain. The species of interest in this subdomain are Fe(II)-TEOA, Fe(III)-TEOA, Na^+, Cl^-, OH^-, and TEOA. It should be noted that TEOA is added in excess to the negative side and its primary role is to form a complex with iron that participates in the desired redox reaction. Also, since TEOA is uncharged, it does not carry any charge through the negative electrolyte. Consequently, it is not necessary to account for the spatial dependence of the concentration of TEOA within the negative electrode domain. For this reason, a transport equation has not been included for TEOA on the negative side. The concentration of TEOA on the negative side is instead accounted for as a time-dependent scalar quantity. Its balance is given in eq (4.1), where $c_{\mathrm{TEOA}}^{\mathrm{neg}}$ is the average concentration of TEOA in the negative electrolyte, $J_{\mathrm{TEOA},0}$ is the flux of TEOA across the membrane that is calculated later in the chapter, V_{tank} is the volume of negative electrolyte, and A_{mem} is the area of the membrane.

$$\frac{dc_{\mathrm{TEOA}}^{\mathrm{neg}}}{dt} = -\frac{J_{\mathrm{TEOA},0} A_{\mathrm{mem}}}{V_{\mathrm{tank}}} \tag{4.1}$$

The porous electrode consists of a complex and tortuous microscopic arrangement of a solid carbon phase and void space (pores) that is filled with electrolyte. The complexity of the electrode geometry necessitates the simplifying assumption that the electrode can be modelled as a pseudo-homogeneous domain to make solution of the model tractable in many cases. This simplification is frequently employed when dealing with porous domains and allows for the usage of porous electrode theory.[202,203] Porous electrode theory uses volumetric averaging of porous electrode phases to establish solid-phase and liquid-phase potentials that are continuous over its domain. Electronic current is conducted in the solid phase, while ionic current is conducted in the electrolyte phase. Porous electrode theory also establishes spatially continuous functions of ionic species concentrations for the electrolyte in the pore volume and mass balance equations to account transport of these species. Porous electrode theory further makes use of the electroneutrality assumption that charge separation does not occur on a macroscopic scale and provides a relationship between electrode current and faradaic redox reactions.[202]

The transport of each species of interest within the electrolyte phase of the negative and positive electrode subdomains is given by eqs (4.2) – (4.5) and consistent with the formulation according to porous electrode theory.[202,203]

$$\frac{\partial(\epsilon c_i)}{\partial t} + \nabla \cdot \boldsymbol{J_i} + \boldsymbol{u} \cdot \nabla c_i = \sum_j \epsilon R_{i,j}^{\mathrm{nct}} + \sum_j \epsilon R_{i,j}^{\mathrm{ct}} \tag{4.2}$$

$$\boldsymbol{J_i} = -\epsilon^{1.5} D_i \nabla c_i - z_i u_{m,i,\mathrm{eff}} F c_i \nabla \phi_l \tag{4.3}$$

$$u_{m,i,\mathrm{eff}} = \frac{\epsilon^{1.5} D_i}{RT} \tag{4.4}$$

$$R_{i,j}^{\mathrm{ct}} = -a_e \frac{\nu_{i,j} i_{\mathrm{loc},j}}{n_{e,j} F} \tag{4.5}$$

Equations (4.2) – (4.5) are valid for all species of interest throughout the interior of the negative electrode subdomain. The first term on the left-hand side of eq (4.2) accounts for the accumulation or depletion of a given species. The second term accounts for the diffusional flux and migration flux due to the electric field (shown in eq (4.3)), while the third term on the left-hand side accounts for convection due to flow of the electrolyte. The terms on the right-hand side account for both the generation and consumption rates of chemical species due to homogeneous chemical (non-charge-transfer $R_{i,j}^{\mathrm{nct}}$) and electrochemical (charge-transfer $R_{i,j}^{\mathrm{ct}}$) reactions, respectively. The diffusion term in eq (4.3) includes the Bruggemann correction to account for the tortuosity of the porous phase.[204] The mobility of ionic species is calculated from the Nernst-Einstein relation given in eq (4.4) and also makes use of this correction. The rates of the charge transfer reactions are given in eq (4.5) and depend on the specific surface area a_e of the electrode that represents the average pore wall area in a unit volume available for electron transfer.[202] The term $\nu_{i,j}$ corresponds to the stoichiometry coefficient of species *i* in the reduction reaction j for a given redox couple. The term $i_{\mathrm{loc},j}$ refers to the local faradaic current due to reaction j, $n_{e,j}$ refers to the number of electrons transferred in reaction j, and $u_{m,i,\mathrm{eff}}$ refers to the effective ionic mobility of species i. This reaction is shown in eq (4.6), where "Red" and "Ox" refer to the reduced and oxidized species in a redox couple, respectively. Coefficients corresponding to the oxidized species are negative, while those corresponding to the reduced species are positive.

$$|\nu_{\mathrm{ox}}|\mathrm{Ox} + ne^- \rightleftharpoons |\nu_{\mathrm{red}}|\mathrm{Red} \tag{4.6}$$

The reactions that occur at the negative electrode are given in eqs (1.2) and (4.7). Equation (1.2) is the intended redox reaction, while eq (4.7) is the hydrogen evolution side reaction. It should be noted that the formal potential is given for eq (1.2), while the standard potential is given for eq (4.7) since the formal potential is not known under the system conditions.

$$2\mathrm{H_2O} + 2e^- \rightleftharpoons 2\mathrm{OH^-} + \mathrm{H_2(g)} \qquad E^o = -0.83\ \mathrm{V\ (SHE)} \tag{4.7}$$

Due to the high electrolyte flow rate through the electrode and the resulting high electrolyte velocity in the y-direction, the x-component of the velocity is considered negligible; thus only convection in the y-direction is considered in the model. The velocity vector in the convection term is assumed to have a constant value that is equal in magnitude to the superficial velocity through the electrode and is directed in the positive y-direction. This is also consistent with the treatment of flow through the porous electrode in other RFB models.[205] Since the velocity profile is specified rather than being computed from a fluid mechanics model, this obviates the need to explicitly include the pressure loss in the system. As a result, it is not possible to estimate the pumping losses that reduce the overall energy efficiency using the model in its present form.

The current densities through the solid ($\boldsymbol{i_s}$) and electrolyte ($\boldsymbol{i_l}$) phases of the porous electrode are given by the current balances in eqs (4.8) – (4.11):

$$\nabla \cdot \boldsymbol{i_l} = \epsilon F \sum_i \left(z_i \sum_j R_{i,j}^{\mathrm{ct}} \right) \tag{4.8}$$

$$\boldsymbol{i_l} = F \sum_i z_i \boldsymbol{N_i} \tag{4.9}$$

$$\nabla \cdot \boldsymbol{i_s} + \nabla \cdot \boldsymbol{i_l} = 0 \tag{4.10}$$

$$\boldsymbol{i_s} = -\sigma_e \nabla \phi_s \tag{4.11}$$

Equations (4.8) and (4.9) account for charge transfer in the electrolyte phase within the electrode, while eqs (4.10) and (4.11) account for charge transfer in the electrode phase. The porous electrode model establishes a continuum where both the solid-phase and electrolyte-phase current densities are spatially continuous in the electrode subdomain. While the electron transfer reactions occur at the interface between these two phases, the model also assumes that this interface is continuous in the electrode subdomain. As electrons are transferred between the electrode and the electrolyte, charged species in the electrolyte are generated and consumed by various electrochemical reactions. Since the ions are the

charge carriers in the electrolyte, their fluxes account for the current through the electrolyte. Equation (4.10) reflects the fact that the loss of charge from the electrolyte is necessarily accompanied by gain of charge by the electrode, and vice versa. The current $\boldsymbol{i_s}$ through the solid phase follows an ohmic relationship with respect to the electrode potential gradient.

Another reasonable assumption for typical electrolytes is electroneutrality, which is described by eq (4.12). This condition can be used to eliminate the concentration of one of the aqueous species so that the balance given by eq (4.2) is not required for this species. The most convenient species to eliminate is one that is maintained at a high concentration and does not participate in any of the chemical and electron-transfer reactions so that its concentration or flux does not appear in any boundary condition.[206] Based on these criteria, Na^+ is the species eliminated by the electroneutrality condition for this system.

$$\sum_i z_i c_i = 0 \tag{4.12}$$

Electrochemical kinetics is also obviously considered in the model. Two electron-transfer reactions occur at the negative electrode: Fe-TEOA redox couple and hydrogen evolution. The inclusion of the HER is justified later in Section 4.6. The Butler-Volmer equation given in eq (4.13) is used to describe the kinetics of the Fe-TEOA redox couple. The exchange current density $i_{0,j}$ in the Butler-Volmer equation for reaction j is related to the standard rate constant for the reaction k_j^0 and has a concentration dependence given in eq (4.14), where $C_{R,j}$ and $C_{O,j}$ represent the concentrations of the reduced and oxidized form of the redox species at the electrode, respectively.

$$i_{\mathrm{loc},j} = i_{0,j}\left(\exp\left(\frac{(1-\alpha_j)F\eta_j}{RT}\right) - \exp\left(\frac{-\alpha_j F\eta_j}{RT}\right)\right) \tag{4.13}$$

$$i_{0,j} = Fk_j^0 C_{O,j}^{1-\alpha_j} C_{R,j}^{\alpha_j} \tag{4.14}$$

The activation overpotential η_j of reaction *j* given in eq (4.15) is obtained from the difference between the solid phase potential (ϕ_s) and the electrolyte phase potential (ϕ_l) of the porous electrode and the reversible potential of the reaction. The reversible potential $E_{\mathrm{rev},j}$ of reaction j is given by the Nernst equation (eq (4.16)). Since eq (4.16) is formulated in terms of species concentrations rather than activities, it is expressed in terms of a formal potential ($E_j^{o\prime}$) rather than a standard potential (E_j^o).

$$\eta_j = \phi_s - \phi_l - E_{\mathrm{rev},j} \tag{4.15}$$

$$E_{\mathrm{rev},j} = E_j^{o\prime} - \frac{RT}{n_{e,j}F}\ln\left(\prod_i c_i^{\nu_{i,j}}\right) \tag{4.16}$$

The transfer coefficients α_j for the primary redox couples are assumed to be 0.5, as this value is frequently assumed in the absence of an experimentally determined value for the specific combination of redox couple and electrode[207] and already used for the Fe-CN redox couple in the literature.[208,209] Although the Butler-Volmer equation can be formulated more generally to account for concentration overpotential and limiting current, the present model does not use such a formulation. Due to the high flow rate of electrolyte through the porous electrode and the linearity of the polarization plot of the flow battery system over a wide range of current densities up to 400 mA/cm^2,[17] mass transfer limitations associated with departure of the concentrations of redox species at the electrode surface from their bulk values are neglected under practical operating conditions in the flow battery. The absence of any observed limiting current density makes it difficult to estimate or fit the parameters necessary to modify the kinetics expressions accordingly.

The hydrogen evolution reaction is not considered to be reversible; thus, it can be approximated by the simpler cathodic Tafel equation given in eq (4.17) that does not involve the reverse reaction at all. This is reasonable given that H_2 oxidation does not occur during discharge. The Tafel slope ($A_{c,\mathrm{H_2}}$) is an empirical coefficient that can be determined by fitting to experimental data. In the absence of empirical

data for HER kinetics under the prevailing conditions of this system, a “typical” value of -118 mV has been used; this is equivalent to assuming a transfer coefficient of 0.5 that is widely assumed for redox couples in the absence of other data, as discussed earlier.[210]

$$i_{\mathrm{loc,H_2}} = -i_{0,\mathrm{H_2}}\, 10^{\frac{\eta_{\mathrm{H_2}}}{A_{c,\mathrm{H_2}}}} \tag{4.17}$$

Both the Butler-Volmer and Tafel equations are dependent on the overpotential η_j for the given electrode reaction j defined by eq (4.15). The formal potential of -0.86V vs. SHE for the iron-triethanolamine redox couple was determined experimentally by Gong et al.[17] from cyclic voltammetry and is used in the present work.

4.1.2 Boundary Conditions

The equations that govern the behaviour of the negative electrode require boundary conditions to generate a unique solution to the model. The choice of appropriate boundary conditions is important to ensure that the model can be solved successfully and that it produces results that reflect the reality of the system being modelled. Boundary conditions apply for the boundaries of each subdomain labelled (1) to (10) in Figure 4.2 below.

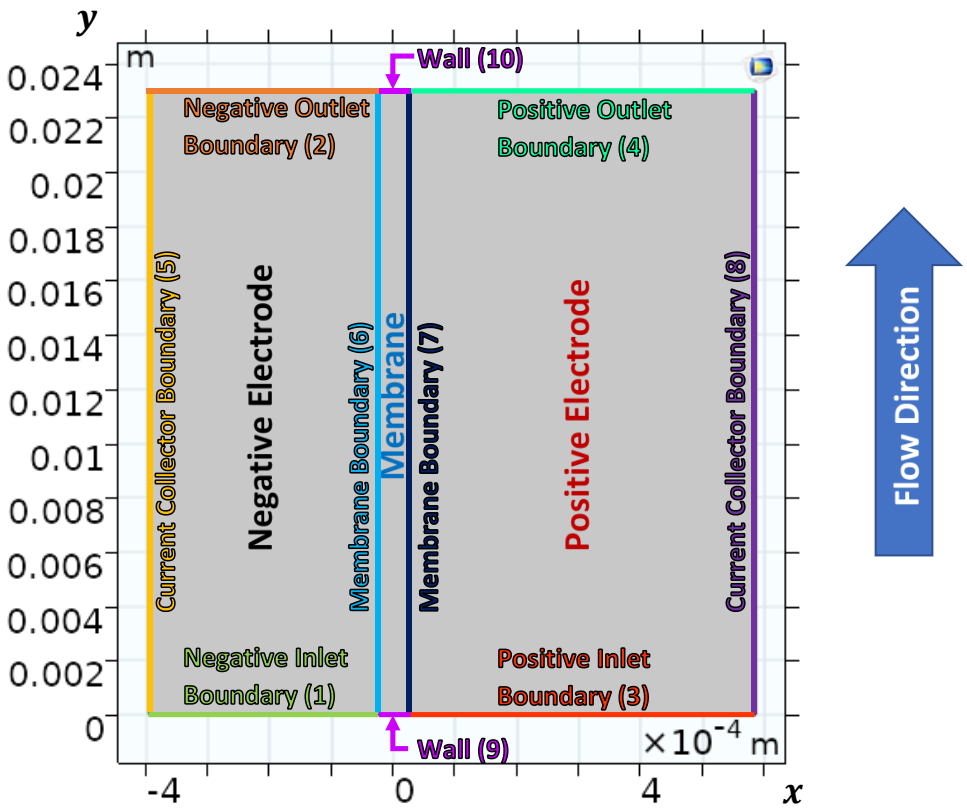

Figure 4.2: Boundaries of the domain geometry include electrolyte inlets and outlets, current collector boundaries, and membrane boundaries for each electrode. Boundaries are numbered for later reference. Impermeable wall boundaries are also labelled.

The electrolyte inlet and outlet on the negative side of the battery occur at boundaries (1) and (2), respectively. The condition specified at boundary (1) is given in eq (4.18) and is a concentration constraint. This boundary condition serves to specify the inlet concentrations $c_{i,0}$ of all chemical species of interest. Numerically, this boundary condition is implemented in COMSOL as an equivalent flux (Danckwerts) boundary condition because this can improve solution stability and reduce oscillations in situations where high reaction rates occur near the inlet.[206]

$$c_i|_{\text{inlet}} = c_{i,0} \tag{4.18}$$

Boundary (2) has an outlet condition represented by eq (4.19), where $\boldsymbol{n}$ is the unit normal vector for the relevant control surface. This boundary condition assumes that concentration gradients are sufficiently small by the time the fluid has reached the outlet that transport by diffusion is negligible in comparison to transport by convection due to fluid flow and migration due to electric fields. Due to the high flow electrolyte flow rate through the porous electrode, convection is likely to dominate diffusion as a transport mechanism for the species present. This assumption can further be justified by the likelihood that each species reaches a final constant concentration by the time it leaves the electrode.

$$\boldsymbol{n} \cdot D_i \nabla c_i = 0 \tag{4.19}$$

The current collector for the negative electrode (boundary (5)) is impermeable to all aqueous species and is subject to a constraint on the potential. Due to the impermeability of this boundary, the flux of all species at this boundary is set to zero (eq (4.20)). It is common practice to refer to the negative electrode, which is at the lower potential of the two electrodes, to be at ground. By grounding the negative electrode, its electric potential is set to zero in eq (4.21).

$$\boldsymbol{n} \cdot \boldsymbol{J_i} = 0 \tag{4.20}$$

$$\phi_s = 0 \tag{4.21}$$

The final explicit boundary condition specified for the negative electrode subdomain occurs at the interface (boundary (6)) with the ion exchange membrane. This boundary condition involves a combination of phenomena that enforce continuity of current through the ion exchange membrane, impermeability to species other than charge carriers, coupling of the charge carrier flux to the current, and coupling of the potential drop to the charge carrier concentration gradient. This boundary condition is specified in greater detail in the following sub-section describing the equations within the membrane subdomain (see eqs (4.25), (4.26), and (4.27)).

4.2 Membrane Subdomain

The membrane subdomain comprises the Nafion 212 membrane that separates the negative and positive porous electrodes. Unlike the porous electrode subdomains that use partial differential equations to model the concentrations of redox species, the membrane is treated as a simpler ohmic element wherein only the potential is solved with a differential equation. This simplification requires the assumption that the current through the membrane is due to transport of a single ionic species. If multiple charge carrier ions were considered in the membrane subdomain, the model for this subdomain would need to include partial differential equations for all present ionic species (as in the porous electrode subdomains).

Nafion is a cation exchange membrane, where protons act as the primary charge carriers under acidic conditions. Under alkaline conditions, as in the case of the present redox flow battery system, it has been shown that the predominant charge carrier in Nafion is the hydroxide ion.[211] While sodium cations also participate as charge carriers,[212] the level of detail required to include their contribution does not justify the added complication and time that would be required to numerically solve the governing equations. It is for this reason that a single-ion transport model has been utilized to describe the membrane subdomain. This is also consistent with other flow battery models reported in the literature.[139,213]

The Nafion membrane is modelled as an electrolyte, where the flow of charge carriers constitutes the current. This relationship is given by eqs (4.22) and (4.23):

$$\nabla \cdot \boldsymbol{i_m} = 0 \tag{4.22}$$

$$\boldsymbol{i_m} = -\sigma_m \nabla \phi_m \tag{4.23}$$

Equation (4.22) reflects the conservation of charge across the membrane. Equation (4.23) specifies an ohmic relationship between the current density and the membrane potential gradient. The membrane conductivity σ_m is treated as an empirical property that will be obtained by fitting the model to experimental data, as discussed later. Equations (4.22) and (4.23) are solved in conjunction with the boundary conditions at the i) insulating interfaces (9-10) along the bottom ($y = 0$ m) and top ($y = 0.023$ m) edges of the membrane and ii) ion-exchange interfaces (6-7) with the negative and positive electrodes. The insulation conditions specify that the normal flux of charge carriers, and thus current, is zero through these surfaces, as described in eq (4.24):

$$-\boldsymbol{n} \cdot \boldsymbol{i_m} = 0 \tag{4.24}$$

The ion exchange membrane boundary conditions prevail at boundaries (6) and (7) of Figure 4.2. These boundary conditions consist of three explicit relationships given in eqs (4.25), (4.26), and (4.27) that are implemented simultaneously. These equations apply at each membrane-electrolyte interface.

$$\phi_l - \phi_m = -\frac{RT}{z_i F} \ln\left(\frac{c_{\mathrm{OH}}^{\mathrm{elec}}}{c_{\mathrm{OH}}^{\mathrm{mem}}}\right) \tag{4.25}$$

$$\boldsymbol{n} \cdot \boldsymbol{i_l} = \boldsymbol{n} \cdot \boldsymbol{i_m} \tag{4.26}$$

$$\boldsymbol{n} \cdot \boldsymbol{J}_{\mathrm{OH}} = \frac{\boldsymbol{n} \cdot \boldsymbol{i_l}}{z_{\mathrm{OH}} F} \tag{4.27}$$

Equation (4.25) describes the difference in electrolyte (ϕ_l) and membrane (ϕ_m) potentials at the membrane-electrode interface that occurs due to a difference in the concentration of the charge carrier between the electrolyte and the membrane. The membrane is assumed to have a different capacity to hold charge carriers compared to the electrolyte due to its fixed charged functional groups, which results in this concentration difference between the two phases. The net effect of eq (4.25) applied at both boundaries determines the Donnan potential drop across a selective membrane that separates two electrolytes with different concentrations of the charge carrier. This potential is due to the selectivity of

the membrane restricting some ions from permeating and moving between the two electrolytes.[214,215] The model considers the membrane to be permeable only to hydroxide ions as charge carriers. It should be noted that the variable $c_{\mathrm{OH}}^{\mathrm{elec}}$ corresponds to the concentration obtained in each of the electrode subdomains. The boundary condition in eq (4.26) enforces the continuity of current at the boundary, i.e., the flow of current leaving either the membrane or electrode is accompanied by an identical flow entering the other. Equation (4.27) describes Faraday's Law relating the molar flux of charge carriers across the membrane boundary to the corresponding current density being carried. Finally, the flux of each species other than the charge carrier hydroxide ions is assumed to be zero (i.e. eq (4.20)). The walls labelled as boundaries (9) and (10) at the top and bottom of the ion exchange membrane are considered impermeable and insulated such that no current or chemical species pass through them.

4.3 Positive Electrode Subdomain

The positive electrode subdomain is modelled very similarly to the negative electrode. The main phenomena that differ are the electron-transfer reactions, leakage of TEOA from the negative side to the positive side, and the consequent side reaction involving TEOA. The reactions that occur at the positive electrode are given in eqs (1.1) and (4.28). The former is the desired redox reaction, while the latter is the side reaction involving TEOA oxidation. Since the products of the TEOA oxidation reaction have no further effect on the battery operation, their specific identity is not considered in the present model. Consequently, TEOA oxidation is written as a simplified single-step reaction with nonspecific products. The previous research group investigating this RFB[17] hypothesized a two-step mechanism, whereby TEOA is first oxidized in a 2-electron step to 1-(bis(2-hydroxyethyl)amino)ethane-1,2-diol, which in turn is oxidized in another 2-electron step to 2-hydroxy-N,N-bis(2-hydroxyethyl)acetamide.

$$\mathrm{TEOA} \rightarrow 4e^{-} + \mathrm{products} \tag{4.28}$$

Equations (4.2) – (4.6) and (4.8) – (4.12) account for transport of the aqueous species and current flow, as in the case of the negative electrode. The species on the positive side are listed in Table 4.1. The permeation of uncomplexed TEOA across the membrane and the subsequent reaction (eq (4.28)) are not insignificant and so warrant inclusion in the model within the positive electrode subdomain. This permeation is assumed to be driven by diffusion due to the concentration difference of TEOA on the two sides of the membrane and electro-osmosis due to the movement of charge carriers through the membrane. These mechanisms are lumped together with a permeation coefficient P in eq (4.29) that describes the net flux of TEOA through the membrane:

$$J_{\mathrm{TEOA},0} = \frac{P}{d_{\mathrm{mem}}}\left(c_{\mathrm{TEOA}}^{\mathrm{neg}} - c_{\mathrm{TEOA}}^{\mathrm{pos}}\right) \tag{4.29}$$

The net flux of TEOA through the membrane $J_{\mathrm{TEOA},0}$ depends on the membrane thickness d_{mem}, as well as the concentrations of TEOA in the electrolyte on the negative ($c_{\mathrm{TEOA}}^{\mathrm{neg}}$) and positive ($c_{\mathrm{TEOA}}^{\mathrm{pos}}$) sides of the membrane. Due to the reactivity of TEOA in the positive electrolyte, a transport equation for TEOA (eq (4.1)) is included in the positive electrode subdomain. Equations with the same form as eqs (4.13) – (4.16) also apply to the kinetics of the iron-cyanide redox couple at the positive electrode. The irreversible oxidation of TEOA in the positive electrode subdomain is modelled with the Tafel version of the Butler-Volmer equation (eq (4.30)) that contains only the anodic term and is first order with respect to the TEOA concentration. This equation has been chosen through trial and error that also considered the unmodified Butler-Volmer equation. The formulation in eq (4.30) produces reasonable results reliably with greater model stability. The TEOA oxidation current $i_{\mathrm{loc,TEOA}}$ depends on the reaction standard rate constant k_{TEOA}^{0}, TEOA concentration c_{TEOA}, transfer coefficient α_{TEOA}, and overpotential η_{TEOA}. The determination of the numerical values of the rate constant, transfer coefficient, and formal potential in this equation is discussed in Chapter 5.

$$i_{\mathrm{loc,TEOA}} = F k^{0}_{\mathrm{TEOA}} c_{\mathrm{TEOA}} \exp\left(\frac{\alpha_{\mathrm{TEOA}} F \eta_{\mathrm{TEOA}}}{RT}\right) \tag{4.30}$$

The electrolyte flow through the positive electrode is modelled using the same boundary conditions as in the case of the flow through the negative electrode. The electrolyte inlet at boundary (3) is described by eq (4.18) and the electrolyte outlet at boundary (4) is described by eq (4.19). Boundary (7) is subject to the ion exchange membrane boundary conditions given by eqs (4.25) – (4.27), as specified in the previous section. An additional boundary condition is required for boundary (7) to account for the flux of TEOA across the Nafion membrane. This is described in eqs (4.29) and (4.31), which specify an average flux of TEOA $J_{\mathrm{TEOA,0}}$ across this boundary. The flux of TEOA is dependent on its concentration difference across the membrane and the permeation coefficient P of the membrane.[17]

$$-\boldsymbol{n} \cdot \boldsymbol{J}_{\mathbf{TEOA}} = J_{\mathrm{TEOA,0}} \tag{4.31}$$

As with the left current collector boundary (5), the right current collector boundary (8) is impermeable to all chemical species and so the zero-flux condition of eq (4.20) applies to all species. In addition, another boundary condition for this interface accounts for specified applied current density i_{app} as given in eq (4.32). This equation maintains conservation of current by stating that the average current density through the current collector is equal to the average current density through the solid electrode phase at the interface between the two. The potential of the positive electrode cannot be specified and is a quantity determined by the model. It is also important to note that the specified current density i_{app} is negative during charge and positive during discharge.

$$\int_{\partial\Omega} \boldsymbol{i_s} \cdot \boldsymbol{n} dl = i_{\mathrm{app}} \int_{\partial\Omega} dl \tag{4.32}$$

4.4 Spatially Independent Equations

During charge and discharge of the battery, the concentrations of species at the electrode inlets vary with time as electrolytes are pumped from the reservoir tanks to the electrodes. Since these inlet concentrations are specified explicitly in eq (4.18) at (1) and (3), their variation with time must also be included. For this purpose, each reservoir is modelled as a simple tank, in which the electrolyte is assumed to be perfectly mixed before re-entering the corresponding electrode. This is described by the simple mass balance in eq (4.33) for each species, where Q is the constant electrolyte flow rate and V_{tank} is the constant electrolyte volume in the tank. Since the outlet concentration is a function of the x-coordinate, the average outlet concentration must be computed for the model to reflect the physical reality of the system. The average outlet concentration in eq (4.33) is determined using the "average" operator in COMSOL Multiphysics. This operator can integrate a model variable to produce its average over one or more spatial dimensions. In this case, the average species concentrations over the length of the outlet boundaries are computed for use in eq (4.33):

$$\frac{dc_{i,0}}{dt} = \frac{Q}{V_{\text{tank}}}\left(c_i|_{\text{outlet}} - c_{i,0}\right) \tag{4.33}$$

This tank model results in a set of ordinary differential equations coupled to the transport equations in the battery subdomains described previously. Each of the ordinary differential equations provides a balance on the inlet concentration of a single species to the battery. A reservoir tank balance is not required for the species that is eliminated using the electroneutrality condition. The tank model equations are implemented in COMSOL Multiphysics as spatially-invariant general ODEs that are not attached specifically to any subdomain. Based on the formulation and notation, however, these equations do not overlap or interfere with one another.

4.5 Numerical Solution Details

The model is implemented in COMSOL Multiphysics with solution parameters described in Table 4.2.

Table 4.2: Solution Parameters for COMSOL Multiphysics Solver

Relative Error	0.0025 (single-cycle) / 0.01 (multiple-cycle)
Maximum time step	10 s (single-cycle) / 5 s (multiple-cycle)
Time Stepping Method	Backward differentiation formula (BDF) Min BDF order: 1; Max BDF order: 5
Mesh	Physics-controlled, extremely fine

4.5.1 Mesh and Solver Settings

Physics-controlled meshing has been used to generate meshes for all three subdomains. This meshing procedure uses the types of physics being modelled such as current distribution and reactant transport to automatically generate a mesh with a desirable structure for the model domain. The mesh size is set to the "extremely fine" setting to minimize numerical error in the model at the expense of computation time. The resulting two-dimensional mesh consists of primarily triangular elements with varying sizes. Smaller mesh elements are formed where the solution is expected to vary more significantly spatially. The relative error tolerance for the multiple-cycle solver is set to 0.01, as this provides a good balance of efficiency and accuracy. The relative error tolerance is set to 0.0025 for the single-cycle solver for superior accuracy during fitting and model validation. The time-dependent solver uses backward differentiation formula (BDF) time-stepping due to its stability, particularly with respect to stiff equation systems such as those encountered in reaction-diffusion transport problems.[203,216–218] Although the software has other time-stepping methods available, none of them support the use of the *Events* interface that is necessary for controlling the solver (as explained in the following subsection). The solver makes use of BDF with minimum order of 1 and maximum order of 5. The order of the BDF solver

refers to the number of steps used to obtain each subsequent set of values of the dependent variables.[219] The first order BDF is also known as the backward Euler method. At each time step, the solver makes use of the Newton method with damping to iteratively solve the system of algebraic and differential equations for the system. If this method fails to converge, the step size is reduced and solution of the system is attempted again.[216] The time-dependent solver follows an intermediate time-stepping scheme that ensures the model equations are solved at least once within each 5 s (multi-cycle formulation) or 10 s (single-cycle formulation) subinterval.

4.5.2 Events Interface

As mentioned earlier, the average current density ($i_{s,\mathrm{avg}}$) specified in eq (4.32) is positive or negative, depending on whether the battery is being charged or discharged. It is necessary that this boundary condition be updated when the operation mode of the battery switches between charge and discharge. This can be achieved using the *Events* interface in the COMSOL Multiphysics package. The *Events* interface allows variables in a model to be reinitialized as desired when certain implicit or explicit conditions are met. An explicit event is one for which the time of occurrence is known prior to solving the model, such as a time-triggered discharge. An implicit event is one for which the time of occurrence is unknown prior to solving the model and is determined based on some criterion as the model is solved, such as a voltage-triggered discharge. Both types of events are incorporated in the present model for different purposes.

The single-cycle formulation of the model uses an explicit event to switch from charge to discharge after ~ 1704 s have elapsed, corresponding to the approximate time at which the mode was switched in the single-cycle run conducted in the experimental study of Gong et al.[17] The multiple-cycle formulation of the model makes use of implicit events to enable automated charge and discharge of the battery. One implicit event switches from charge to discharge when the battery voltage reaches 1.6 V, based on the

criterion used by Gong et al.[17] in their study. Another implicit event switches from discharge to charge when the battery voltage reaches 0.85 V. The discharge threshold of 0.85 V, which is higher than the 0.5 V threshold used in the experimental test setup, is used due to the rapid drop of the battery voltage that is observed at this point of operation. By the time the battery reaches a voltage of 0.85 V it has, in effect, discharged completely. Setting a lower discharge threshold voltage can cause convergence difficulties that result in failure of the solver. A final implicit event is used to pre-empt failures due to convergence. This implicit event is triggered when the solver time step gets smaller than 5×10^{-4} s, an indication that the solver is experiencing convergence issues. This condition usually occurs when discharge is effectively complete but the cell voltage is above the threshold voltage. A likely phenomenon responsible for this convergence difficulty is the large change in potential with position at the end of discharge, as reactants are depleted to low levels. This phenomenon is discussed in more detail in Chapter 6. This implicit event triggers the switch to battery charge, despite not having reached the threshold discharge voltage. This step size threshold has been chosen by inspection of the convergence data obtained over the course of modelling such that it is small enough to trigger only under poor convergence conditions but not so small that it is unable to trigger before the solver is forced to terminate. In the event that a convergence problem is not associated with deep discharge of the battery, this condition is likely not relevant.

4.5.3 Run-time and Stop Conditions

The time-dependent solver requires explicit specification of the range of times to simulate the model. In the single-cycle case, it is known that the battery discharged completely within ~ 3320 s. If the range of times being solved by the model ends prior to complete discharge of the battery, the full behaviour is not modelled sufficiently. If the battery discharges completely prior to the end of the time range, the solver continues to run indefinitely or terminate due to an error. It is for this reason that a stop

condition has been used for the single-cycle formulation of the model. This condition is able to stop the run when a certain condition is fulfilled. In the single-cycle formulation, a stop condition has been added to terminate the model when the battery voltage drops below 0.5 V. With the inclusion of this stop condition, the time range specified to the solver can be set to 3400 s, much greater than the expected end of the model, allowing all behaviour to be modelled without the risk of solver error. An additional stop condition is used to terminate the run when the time-dependent solver uses a time step smaller than 2.5×10^{-6} s, indicating that the model has failed to converge. For the multiple-cycle formulation of the model, a stop condition is not strictly necessary due to the fact that the model continues to alternate between charge and discharge as long as it runs. The stop condition that relates to convergence still applies to the multiple-cycle formulation. The time step size at which the run is terminated for the multiple-cycle model is smaller than the step size required to trigger the implicit event that causes the battery to charge. Thus, if a convergence error is caused by deep discharge of the battery, the stop condition is invoked prior to solver termination.

4.6 Model Development

The model and the role of the side reactions in particular presented in this chapter were obtained after several model versions were evaluated to correctly explain the experimental observations. Some of the considerations that went into this process are outlined in this section. This analysis consists of determining the cause of current efficiency loss, identifying the likely reaction responsible for said current efficiency loss, finding the most desirable implementation of the reaction in the model, and addressing issues involving reactant imbalance in the electrolytes.

The coulombic or current efficiency (CE) of a battery is defined as the ratio of the charge transferred during discharge to the charge transferred during charge.[120] In the previous experimental study of this

system, the current efficiency of the modelled redox flow battery is found to be ~ 93% in the single-cycle test and varied in the range of 80-90% during multi-cycle testing, as shown in Figure 4.3.[17]

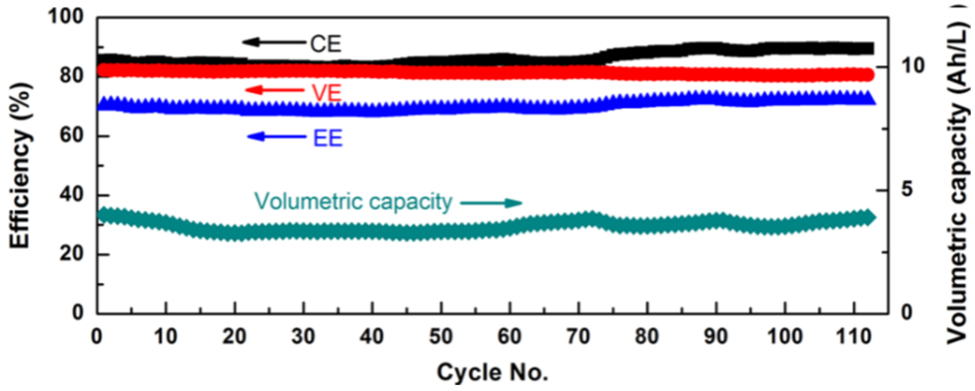

Figure 4.3: Multi-cycle experimental results for the RFB system. Reproduced from Gong et al.[17] with permission from the American Chemical Society.

The fact that the CE of the battery is not 100% indicates that at least one side reaction occurs at either one or both of the positive and negative electrodes. The cause of this reduced CE is explored in the original experimental study through measurements of the half-cell potential of each electrode with respect to a reference electrode during single-cycle discharge of the battery.[17] These experiments clearly show that the positive electrode potential is responsible for the drop in cell voltage at the end of discharge; this implies that the positive electrode reaction is limiting and causing the drop in CE and that a second reaction is occurring at this electrode during battery discharge.

Gong et al.[17] first investigated the possibility of oxygen reduction being the side reaction at the positive electrode during discharge. However, they obtained a current efficiency of 100% in a symmetrical cell with the iron-cyanide redox reaction occurring at both electrodes, suggesting that no side reaction, including oxygen evolution, would be expected to take place at the positive electrode of the actual battery in the absence of any other redox-active species. The next cause of the loss of current efficiency in the overall RFB system that Gong et al.[17] considered was the crossover of triethanolamine through the Nafion membrane from the negative side to the positive side and its subsequent oxidation by

ferricyanide present on the positive side (see Section 4.3 for a previous discussion of this reaction). This process reduces ferricyanide ($Fe(CN)_6^{3-}$) to ferrocyanide ($Fe(CN)_6^{4-}$), as does the intended discharge redox reaction, but reduces the current efficiency and causes faster depletion of ferricyanide on the positive side.[17] The researchers found that triethanolamine can be oxidized electrochemically in the presence of iron-cyanide species at lower potentials than that required for direct oxidation by the electrode in the absence of iron-cyanide species. They also found from membrane crossover experiments that leakage of free triethanolamine through the Nafion membrane was significant relative to that of other species, given its high permeability and very large concentration difference on the two sides of the battery.[17]

The permeation rate of TEOA from the negative side to the positive side determined experimentally for this RFB by Gong et al.[17] is insufficient to account for the observed reduction in current efficiency. One of the researchers[220] speculates that the actual permeation coefficient during RFB operation could be larger than the measured value due to the presence of an electric field. It should be noted that the crossover tests in the original study were conducted in the absence of an electric field. One explanation for this discrepancy involves the possibility that some of the TEOA carries a charge that increases its crossover due to migration in the presence of an electric field. TEOA can be protonated and thus develop a positive charge with a pKa of approximately 8.[221] However, the high-pH conditions of the battery make it likely that the quantity of charged TEOA is negligible.

A more reasonable explanation for the high permeation rate of TEOA that has been cited in another study of this type of RFB is electro-osmosis. In a study of a similar iron-triethanolamine/iron-cyanide RFB, the authors state that electro-osmosis due to the flow of charge carriers across the Nafion membrane results in the transport of uncharged TEOA from the negative to positive electrode compartment.[186] This explanation is preferable because it explains why permeation of TEOA is

accelerated in the presence of an electric field and does not require TEOA to have a charge in alkaline solution. If this were the case, the permeation of triethanolamine across the membrane may be accelerated by the presence of electric fields during operation of the battery. For this reason, the permeation coefficient for TEOA was estimated by fitting the model to the single-cycle experimental data.

In developing the model for this system, we have explored the feasibility of triethanolamine oxidation on the positive side proposed by Gong et al.[17] and several other alternatives as explanations for the loss in the CE. These possibilities are detailed in the remainder of this section.

4.6.1 Chemical Oxidation of TEOA

The simplest case for the side reaction is the chemical oxidation of TEOA by ferricyanide and is investigated first. In this case, the oxidation process consists of a reaction in the electrolyte phase between ferricyanide and TEOA to produce the oxidation products and ferrocyanide. The kinetics of the chemical oxidation of triethanolamine by ferricyanide in alkaline solution has been studied by Shukla et al.[222] According to this study, the rate law for consumption of ferricyanide follows the expression given in eq (4.34) at lower hydroxide concentrations. At hydroxide concentrations higher than approximately 20 mM, the dependence on hydroxide concentration changes, with the reaction rate becoming proportional to $(c_{OH})^{1.25}$. Since the hydroxide concentrations are high in the present system, eq (4.35) has also been considered in the model investigation.

$$r_{\text{Fe(III)-CN}} = -k_{\text{chem}} c_{\text{Fe(III)-CN}} c_{\text{OH}} c_{\text{TEOA}} \tag{4.34}$$

$$r_{\text{Fe(III)-CN}} = -k_{\text{chem}} c_{\text{Fe(III)-CN}} (c_{\text{OH}})^{1.25} c_{\text{TEOA}} \tag{4.35}$$

$$r_{\text{Fe(III)-CN}} = -k_{\text{chem}}^{\text{obs}} c_{\text{Fe(III)-CN}} \tag{4.36}$$

Sets of apparent rate constants with respect to ferricyanide ($k_{\text{chem}}^{\text{obs}}$) corresponding to eq (4.36) are tabulated in the study where the concentration of one of the three reactants (triethanolamine, ferricyanide, and hydroxide) is varied with the remaining concentrations held constant. The chemical reaction rate constant k_{chem} is not reported in the Shukla et al.[222] study. While the tabulated apparent rate constants are dependent on the concentrations of the reactants, they can be used to determine the chemical rate constant k_{chem} using linear regression. Shukla et al.[222] report values of the apparent rate constants at different TEOA concentrations with hydroxide and ferricyanide concentrations of 25 mM and 2 mM, respectively. Plotting these data (Figure 4.4), we find that the dependence of $k_{\text{chem}}^{\text{obs}}$ on c_{TEOA} is strongly linear. The expression for the best-fit straight line and R^2 are shown in Figure 4.4.

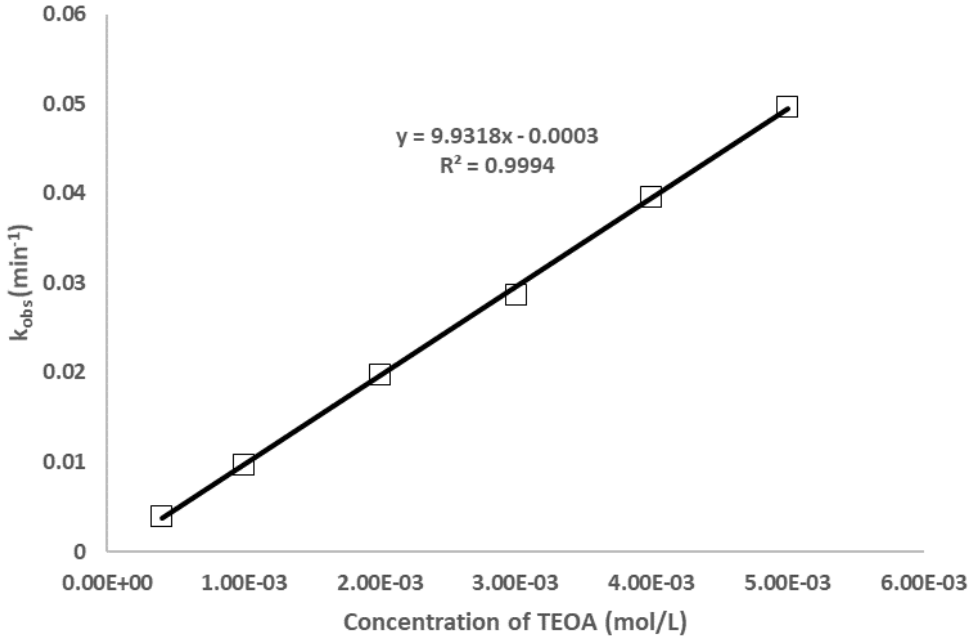

Figure 4.4: Apparent rate constant for ferricyanide oxidation of TEOA with linear fit.

The value of k_{chem} is then obtained by dividing the slope of the straight line in Figure 4.4 by $c_{\text{OH}}^{1.25}$ to yield a value of $1.0 \times 10^3 \frac{L^{2.25}}{\text{mol}^{2.25} \cdot \text{min}}$. This is due to the high hydroxide concentration present in the system, which suggests that eq (4.35) is more valid than eq (4.34). The rate law given in eq (4.35) and the rate

constant calculated above were incorporated into an early version of the model as the sole side reaction.

Under the assumption that the chemical oxidation of TEOA by ferricyanide is responsible for the loss of current efficiency in the studied battery, the permeation rate of TEOA is of direct consequence to the current efficiency. TEOA that permeates the membrane from the negative compartment to the positive compartment is oxidized by ferricyanide. This reaction would partially consume ferricyanide rather than the intended electrode reaction. Since the charge used to generate that fraction of ferricyanide cannot be recovered during discharge, the current efficiency is reduced by this process.

The primary reason why this formulation of the TEOA oxidation reaction has not been adopted into subsequent versions is primarily because of the potential dependence of the TEOA oxidation reaction that has been observed experimentally. Gong et al.[17] found that when 0.01 M $Fe(CN)_6^{4-}$ is added to a much greater concentration (0.2 M) of triethanolamine during cyclic voltammetry, an anodic current is observed that is significantly larger in magnitude than the sum of anodic currents observed in the cyclic voltammetry studies obtained in the presence of each species separately at the same concentrations. This is shown in Figure 4.5.

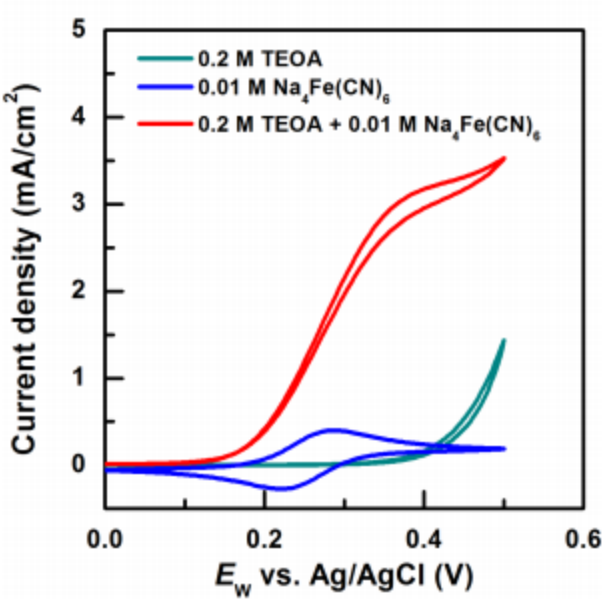

Figure 4.5: Cyclic voltammetry study of TEOA oxidation in the presence of iron-cyanide. Reproduced from Gong et al.[17] with permission from the American Chemical Society.

This behaviour suggests that the electrooxidation of TEOA is catalyzed in the presence of ferricyanide. Due to the relatively fast kinetics of the chemical oxidation of triethanolamine by ferricyanide, one possibility is that the side reaction involves a combination of chemical oxidation and electrochemical oxidation steps. In particular, ferricyanide would first oxidize triethanolamine and be converted to ferrocyanide which would then be oxidized electrochemically back to ferricyanide at the electrode. Although this mechanism may be plausible, its implementation in the model requires the assumption that the potential-dependent kinetics of TEOA oxidation is due to the chemical oxidation coupled to the kinetics of the existing primary redox reaction at the positive electrode for this formulation to reflect reality. As an alternative, TEOA oxidation can be modelled directly as an electrochemical reaction with kinetics that can be fit to the data. This alternative formulation does not require such a restrictive assumption regarding the mechanism of TEOA oxidation and so is a better candidate for use in the model. It is for this reason that chemical TEOA oxidation is not included in the final model formulation and has been replaced with electrochemical TEOA oxidation, as explained in the following subsection.

4.6.2 Electrochemical Oxidation of TEOA

The TEOA oxidation reaction is incorporated into the next major model version as a porous electrode reaction given by eq (4.28). It replaces the chemical reaction between TEOA and ferricyanide in the solution within the pores of the positive electrode that is considered in the version of the model described in the previous subsection. This model version has TEOA oxidation as the only side reaction. In this formulation, the side reaction can reduce the current efficiency in two ways: (i) during charge, the anodic current is split between the primary Fe(II)-CN/Fe(III)-CN reaction and the TEOA oxidation side reaction and (ii) during discharge, the current at the positive electrode is split between the primary Fe(III)-CN reduction and the TEOA oxidation side reaction.

$$\mathrm{TEOA} \xrightarrow{\text{Catalyzed by } \mathrm{Fe(CN)_6^{3-}}} 4e^- + \text{products} \tag{4.28}$$

The electron transfer coefficient α required in the Butler-Volmer equation for TEOA oxidation is initially estimated by using non-linear regression to fit the voltammetry data for this reaction obtained from Gong et al.[17] to the Butler-Volmer equation. The equilibrium potential for the reaction is also estimated from this data by inspection. These kinetic parameters are then modified as necessary to fit the flow battery model to experimental data. It can be inferred from Figure 4.5 and the high chemical reaction rate constant earlier that the kinetics of TEOA oxidation under these conditions is fast relative to the permeation rate of TEOA through the Nafion membrane; thus, the reaction is assumed to be permeation-limited. This assumption is supported by the fact that Fe-TEOA solubility is dependent on an excess of TEOA.[200] If TEOA oxidation is limited by reaction kinetics, this suggests that more TEOA crossover occurs than in the permeation-limited case. With so much TEOA crossover it would be reasonable to expect some loss of iron-triethanolamine solubility and permanent loss of capacity, which has not been observed. The assumption of permeation-limited TEOA oxidation is further supported by

empirical evidence collected for a similar iron-cyanide/iron-TEOA RFB that finds the concentration of TEOA in a sample taken from the positive electrolyte to be on the order of 1 mM.[186] Such a small concentration of TEOA in the positive electrolyte is indicative of fast reaction kinetics that causes TEOA to be oxidized soon after its crossover into the positive electrolyte compartment. It is for these reasons that the model is fairly insensitive to the rate constant used for the TEOA oxidation reaction at the positive electrode. It is also noted that small values of this rate constant introduce instability to the model, resulting in convergence difficulties. Since TEOA oxidation is permeation-limited, the rate constant for this reaction is assumed to be large enough (100 m/s) to reflect this behaviour while preventing the convergence problems.

4.6.3 Reactant Imbalance

The second major version of the model fits the single-cycle data reasonably well; however, the model predicts the battery to exhibit rapid capacity fade over a number of repeated charge-discharge cycles due to the reactant imbalance caused by the side reaction, unlike that observed experimentally. This can be seen from Figure 4.6 that shows the concentrations of the primary redox species over multiple charge-discharge cycles when TEOA oxidation is the only side reaction. The difference in Fe(III)-CN and Fe(II)-TEOA concentrations grows between the two electrolytes over time as the side reaction causes an imbalance between them. This results in capacity fade over time since the battery is unable to charge both electrolytes fully when one of the redox reactants is depleted sooner than the other. For this reason, this version of the model is deemed insufficient; the model needs to be further modified to remove the reactant imbalance and reduce the resulting capacity fade that develops over repeated cycles. The problem of reactant imbalance is described in the following subsection.

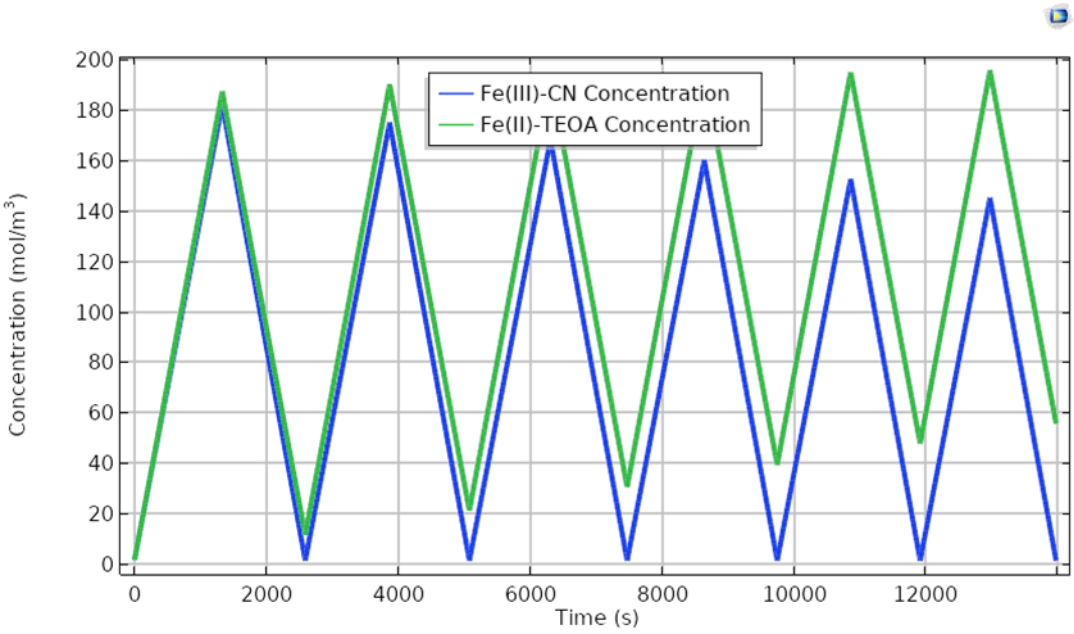

Figure 4.6: Computed concentrations of limiting redox species over multiple cycles without HER.

The reactant imbalance in this model version occurs due to a side reaction on one side that causes the accumulation of a redox species relative to its counterpart at the second electrode, resulting in premature reactant depletion at the second electrode and loss in battery capacity. This process is illustrated in Figure 4.7 and explained below.

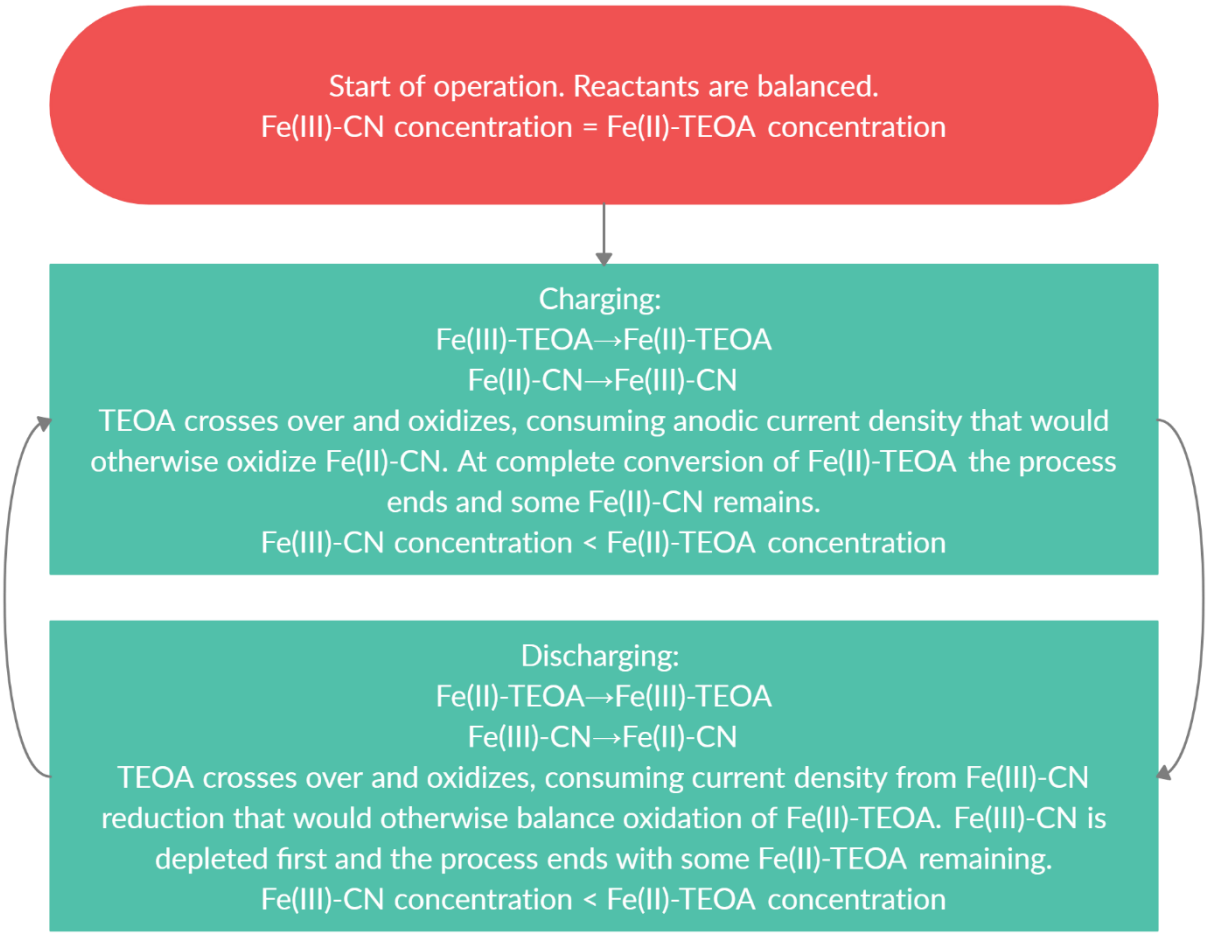

Figure 4.7: Illustration of the process by which an imbalance in redox species concentrations arises and is perpetuated.

During charge, the irreversible anodic current drawn by the side reaction competes with the anodic current of the intended electrode reaction at the positive electrode. Since the intended electrochemical oxidation of ferrocyanide (Fe(II)-CN) to ferricyanide (Fe(III)-CN) does not receive all of the current, it will be out of balance with Fe(II)-TEOA at the end of charge. During discharge, anodic TEOA oxidation continues to occur at the positive electrode, but now subtracts from the current delivered by the intended cathodic reduction of ferricyanide to ferrocyanide at the same electrode. This also limits the amount of current deliverable at the negative electrode due to the anodic oxidation of Fe(II)-TEOA to Fe(III)-TEOA. Discharge terminates when ferricyanide has been completely converted to ferrocyanide

without the complete conversion of Fe(II)-TEOA to Fe(III)-TEOA, resulting in an imbalance that carries forward to the next cycle. Now, once the battery is charged, less Fe(III)-TEOA is available for conversion back to Fe(II)-TEOA, resulting in a shorter charge time and reduced capacity. However, this scenario would lead to a charge imbalance that is not observed in the multi-cycle experiments reported in the literature.

The experimental data obtained from the multi-cycle run of the RFB system shows that the capacity of the battery fluctuates over the course of testing, as shown in Figure 4.3, but these fluctuations are both positive and negative; however, no significant overall decline in the capacity of the battery is observed over time. As described above, a single side reaction is insufficient to explain this long-term behaviour of the battery; an imbalance in the reactants over the course of operation results in continuous capacity fade in the battery model that is not observed in the experiments on the actual battery system. As a result, we consider a second side reaction to enable the model to accurately describe both the single-cycle and multi-cycle behaviour of the battery.

4.6.4 Hydrogen Evolution and Final Formulation

The final version of the battery model includes the electrochemical oxidation of TEOA as a side reaction at the porous positive electrode, as described previously, with the addition of hydrogen evolution as a side electrode reaction at the porous negative electrode. The incorporation of a single TEOA oxidation reaction at the positive electrode without a side reaction at the negative electrode leads to reactant imbalance that causes continuous capacity fade due to the accumulation of Fe(II)-TEOA relative to Fe(III)-CN at the end of discharge. An additional side reaction at the negative electrode is necessary to reduce the magnitude of this capacity fade taking place over many cycles. Given the available evidence, the most likely such side reaction is hydrogen evolution. Although the operation of the battery occurring

under high-pH conditions is less favourable than acidic conditions for hydrogen evolution to take place, hydrogen evolution is still possible. Under alkaline conditions, hydrogen evolution occurs as follows:

$$2\mathrm{H_2O}(l) + 2e^- \rightleftharpoons \mathrm{H_2}(g) + 2\mathrm{OH^-}(aq) \quad (4.7)$$

Equation (4.7) has a standard potential of -0.83 V (SHE),[210] very close to the formal potential of -0.86 V (SHE) for the redox couple at the negative electrode. This further supports the proposal that hydrogen evolution also occurs to some extent at the negative electrode. A prior study of the Fe(II)-TEOA/Fe(III)-TEOA redox couple reveals that some distortion of the cathodic peak is observed in the cyclic voltammograms for this system in alkaline solution.[200] The authors attribute this effect to hydrogen evolution taking place at the graphite electrode. The peak distortion is found to occur at conditions where the ratio of TEOA concentration to Fe(III) concentration is less than 8:1. This condition is met by our current RFB system that contains a total TEOA concentration of 1.0 M and total iron concentration of 0.2 M in the negative electrolyte. Thus, the possibility of hydrogen evolution should not be ignored based on the evidence presented. Gong et al.[17] also note that the Fe(II)-TEOA/Fe(III)-TEOA redox couple has been shown to exhibit relatively low current efficiency in other RFB systems.

We assume that the reaction in eq (4.7) is irreversible due to the difficulty of oxidizing hydrogen gas on a carbon paper electrode and the very high electrolyte flow rate that impedes the adsorption of gas to the electrode. The assumption of irreversibility of hydrogen evolution at the negative electrode allows the use of simpler Tafel kinetics in the model rather than Butler-Volmer kinetics, as described in Chapter 4. Additionally, since the hydrogen evolution reaction under alkaline conditions uses water as the reactant, this reaction has no kinetic dependence on a dissolved species concentration. For this reason, the exchange current density is assumed to be constant in the model.

When implemented in the model, the hydrogen evolution reaction is able to dramatically reduce the capacity fade observed. When comparing the single-cycle results of the model where both TEOA

oxidation (chemical or electrochemical) and hydrogen evolution occur to the results of the model where only TEOA oxidation occurs, the imbalance in reactants is reduced dramatically at the end of the run. This reduction in imbalance and capacity fade provides an improvement for the model in that it exhibits long-term stability over many cycles, as will be discussed further in Chapter 6.

5 Parameter Determination and Estimation

The model developed in the present work includes a number of parameters that affect its behaviour and accuracy. It is neither feasible nor practical to estimate all of these parameters by fitting computed charge/discharge curves to experimental data. For this reason, we rely on the published literature for some of them. The approach adopted to estimate parameter values involves (a) considering the available data, (b) assessing the relevance and accuracy of these data, (c) screening out parameters of questionable accuracy that significantly affect model behaviour, and (d) fitting model output to experimental data in order to estimate the values of these screened parameters.

The available sources of parameter data consisted of manufacturer data sheets, research literature and publications, patents, and data specified by or obtained experimentally by the original researchers of this RFB system.[17] The values of the various model parameters and operating conditions for the RFB system are listed in the following subsections. Tables (5.1) – (5.5) present the large number of parameters that describe the physical conditions of the RFB system. Much of the data for the RFB system is obtained directly from the experiments reported for the system. The remaining parameters are determined from the literature where available and fit to the experimental data where data of acceptable quality was unavailable.

5.1 Assumed Parameter Values

Table 5.1: Assumed Parameter Values

Parameter	Description	Value [Unit]	Reference/Comments
α_{neg}	Transfer coefficient of Fe(II)-TEOA / Fe(III)-TEOA redox couple	0.5	Assumed.
α_{pos}	Transfer coefficient of $Fe(CN)_6^{4-}$/ $Fe(CN)_6^{3-}$ Fe-CN redox couple	0.5	Assumed.
k^0_{TEOA}	Electrochemical reaction rate constant for TEOA (eq (4.30))	$100\ \left[\frac{\mathrm{m}}{\mathrm{s}}\right]$	Assumed.

$c_{\mathrm{OH}}^{\mathrm{mem}}$	Membrane charge carrier concentration	$1.81 \times 10^3 \left[\frac{\mathrm{mol}}{\mathrm{m}^3}\right]$	Assumed based on available proton concentration.[223]
$E_{\mathrm{H_2}}^0$	Standard potential of HER	$-0.83\ [V]$	Assumed as formal potential.[210]

The parameters values assumed in the model are listed in Table 5.1. Transfer coefficients for both primary redox reactions ($\alpha_{\mathrm{neg}}, \alpha_{\mathrm{pos}}$) are assumed to be 0.5, as discussed in Chapter 4.

Although the RFB system in this study is normally operated under alkaline conditions, the membrane that has been used is Nafion, which is a cation-exchange membrane (CEM) designed to conduct protons under acidic conditions. The membrane is made up of a hydrophobic polymeric backbone with hydrophilic sulfonic acid groups that attract water molecules to form clusters. When the membrane is sufficiently hydrated, diffusive transport of protons takes place through the water clusters due to hydrogen-bonding-driven hopping between water molecules and transport of protonated hydronium ions.[224] The datasheet for this component lists a value for the minimum available acid capacity as $0.92 \frac{\mathrm{meq}}{\mathrm{g}}$ on the basis of weight, with a specific gravity of 1.97.[223] The product of these two parameters gives a membrane proton concentration of $1.81 \times 10^3 \frac{\mathrm{mol}}{\mathrm{m}^3}$. However, under the operating conditions of this RFB, the primary charge carriers are expected to be hydroxide ions. The use of the Donnan potential as a boundary condition (eq (4.25)) at each membrane-electrode interface requires that the concentration of hydroxide charge carriers in the membrane be specified. A value for this parameter could not be found in literature; in the absence of a literature value, we assume this value to be equal to the concentration of proton charge carriers in the acidic case that is calculated from the Nafion data sheet.

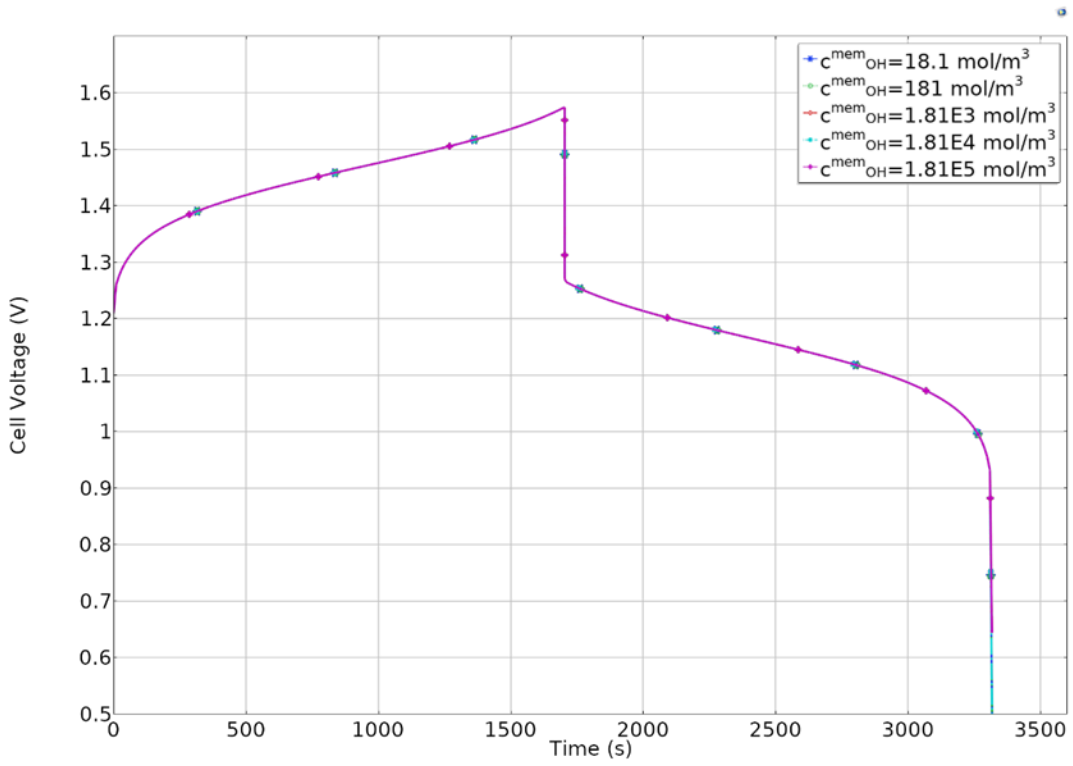

Figure 5.1: Parameter sweep of membrane hydroxide concentration ($c_{\mathrm{OH}}^{\mathrm{mem}}$) on single-cycle curve.

As shown in Figure 5.1, it turns out that the overall charge-discharge behaviour predicted by the RFB model is insensitive to the charge carrier concentration over many orders of magnitude. This figure plots the single-cycle charge-discharge curves for the model with the value for $\boldsymbol{c}_{\mathrm{OH}}^{\mathrm{mem}}$ varied over several orders of magnitude. The curves overlap one another, which implies that the model fit is not affected significantly by this parameter. As a consequence, knowledge of the true hydroxide membrane concentration is not required; on the other hand, this parameter value cannot be accurately estimated by fitting the model to available experimental data. Direct membrane permeability experiments would have to be conducted in order to determine the hydroxide membrane concentration, but such an undertaking is unnecessary for the objective of the present model and thus outside the scope of this work. When eq (4.25) is applied at both membrane boundaries, the net Donnan potential drop over the entire membrane is dependent on the hydroxide concentrations in the two electrolytes only. Thus, the overall system response is expected to be insensitive to the membrane charge carrier concentration,

regardless of operating conditions. Since the model predictions are not sensitive to the hydroxide membrane concentration, their accuracy does not depend on the precise value used.

As mentioned previously, it can be assumed based on the facile kinetics of the $Fe(CN)_6^{4-}$/ $Fe(CN)_6^{3-}$ redox couple and fast chemical kinetics of TEOA oxidation by ferricyanide that the rate of the electrochemical reaction of TEOA at the positive electrode is significantly higher than the rate of TEOA permeation through the membrane. Thus, it is reasonable to conclude that rate of the reaction of TEOA is limited by its permeation through the membrane. The value of rate constant k_{TEOA}^{0} used for the TEOA oxidation reaction has been set to $100\,\frac{\mathrm{m}}{\mathrm{s}}$ to be large enough to be consistent with permeation-limited conditions. This value is determined to be large enough since any further increase in its value does not have a noticeable effect on the model output. In addition, convergence problems with the COMSOL Multiphysics solver are observed when the value of the rate constant is too small. We observe that the model output is not affected by values of this parameter between $0.001\,\frac{\mathrm{m}}{\mathrm{s}}$ and $100\,\frac{\mathrm{m}}{\mathrm{s}}$, but the solver is unable to converge for a step size larger than a few milliseconds over thousands of time steps when it is reduced below $0.0001\,\frac{\mathrm{m}}{\mathrm{s}}$, which prevents solution of the model.

Without this numerical instability, we would expect that further reduction of the rate constant would eventually lead to an increase in the current efficiency of the RFB model when the TEOA oxidation side reaction becomes limited by reaction kinetics. Since the current efficiency predicted by the model is required to match the experimental value, the permeation coefficient of TEOA across the membrane would have to increase to compensate for reduced reaction rate kinetics with increased TEOA concentration in the positive electrolyte. Given that the TEOA permeation coefficient is measured by Gong et al.[17] to be quite small, it is not likely that this coefficient is large enough for the reaction to become limited by kinetics. The permeation coefficient that has been fit under the assumption of permeation-limited TEOA oxidation differs from the measured value of Gong et al.[17] by one order of

magnitude. Additionally, a larger permeation coefficient would result in faster crossover of TEOA and faster depletion of TEOA at the negative electrode. The fact that TEOA is needed in significant excess in the negative electrolyte to enable all of the iron-bearing cations to remain complexed further suggests that a larger permeation coefficient is not correct.

In the absence of a value for the formal potential of the hydrogen evolution reaction under the conditions prevailing in this RFB system, the standard half-cell potential for this reaction is used in its place.[210] The equilibrium potential of this reaction depends on the hydroxide concentration, but the stable concentration of hydroxide within the negative electrode results in a stable equilibrium potential for the HER. The exchange current density for the hydrogen evolution reaction is obtained by trial-and-error fitting of the model to the multi-cycle experimental data. Given that this parameter is estimated by fitting the model to experimental data, as described in Section 5.5, any error in estimating the formal potential of this reaction is much less important to the accuracy of the model than would be the case if literature values of the exchange current density were instead used.

5.2 Calculated Parameter Values

Table 5.2: Calculated Parameter Values

Parameter	Description	Value [Unit]	Reference/Comments
a_e	Electrode specific area	$2.42 \times 10^6 [\mathrm{m^{-1}}]$	Calculated from literature[225] and manufacturer data.[226]
$\boldsymbol{u}_{\mathbf{neg}}$	Negative electrolyte velocity	$2.05 \times 10^{-1} \cdot \boldsymbol{j} \left[\frac{\mathrm{m}}{\mathrm{s}}\right]$	Calculated based on Gong et al.[17]
$\boldsymbol{u}_{\mathbf{pos}}$	Positive electrolyte velocity	$1.35 \times 10^{-1} \cdot \boldsymbol{j} \left[\frac{\mathrm{m}}{\mathrm{s}}\right]$	Calculated based on Gong et al.[17]
$\sigma_{e,xx}$	Electrode conductivity (through-plane)	$1.25 \times 10^3 \left[\frac{\mathrm{S}}{\mathrm{m}}\right]$	Calculated from manufacturer data.[226]
$\sigma_{e,yy}$	Electrode conductivity (in-plane)	$1.72 \times 10^4 \left[\frac{\mathrm{S}}{\mathrm{m}}\right]$	Calculated from manufacturer data.[226]
$V_{\mathrm{tank}}^{\mathrm{neg}}$	Negative electrolyte volume in reservoir	1.985×10^{-5} [$\mathrm{m^3}$] (single-cycle) 1.485×10^{-5} [$\mathrm{m^3}$] (multi-cycle)	Calculated based on personal communication.[220]

$V_{\text{tank}}^{\text{pos}}$	Positive electrolyte volume in reservoir	1.978×10^{-5} [m^3] (single-cycle) 1.478×10^{-5} [m^3] (multi-cycle)	Calculated based on personal communication.[220]

Table 5.2 lists the parameter values that are calculated based on other known values. The surface area of the Toray H-060 carbon paper used as the electrode material in the present RFB system has been reported to be $5.5\,\frac{\text{m}^2}{\text{g}}$.[225] This value for surface area is similar to the values in the range of 0.9-10.9$\frac{\text{m}^2}{\text{g}}$ for comparable carbon papers reported in the literature.[225,227,228] It is possible to use the carbon paper density along with the surface area to determine the volumetric specific surface area.[229] With the density of the electrode known to be $0.44\,\frac{\text{g}}{\text{cm}^3}$ from the manufacturer datasheet,[226] the volumetric specific area required as an input to the model is calculated to be $2.42 \times 10^6\ \text{m}^{-1}$. Although both Toray H-120 and Toray H-060 carbon papers have been used as electrode materials in the RFB system, they are very similar and only differ significantly in terms of their thickness. They therefore are assumed to have the same approximate volumetric specific areas. They are also reported to have the same porosity.[226] Thus, the volumetric specific areas of both carbon paper electrodes are taken to be $2.42 \times 10^6\ \text{m}^{-1}$.

The electrical conductivity of the electrodes used in the RFB is anisotropic; a significant difference exists between the in-plane and through-plane conductivities of the electrode. COMSOL Multiphysics allows the model to account for this characteristic by specifying both of these conductivity values separately. The electrical resistivity of the Toray H-060 electrode is $80\ \text{m}\Omega\cdot\text{cm}$ in the through-plane direction and $5.8\ \text{m}\Omega\cdot\text{cm}$ in the in-plane direction, according to the manufacturer's datasheet.[226] These resistivity values are taken to be representative of both electrodes since Toray H-120 carbon paper has similar properties to Toray H-060. The corresponding conductivities are the inverses of the resistivities.

The volume of the electrolyte on each side of the RFB is not published in the original work or supporting information by Gong et al.[17] Through direct correspondence with one of the authors of the original study, the total electrolyte volume has been confirmed to be 20 mL on each side for the single-cycle run and 15 mL on each side for the multi-cycle run. The choice of a lower electrolyte volume in the multi-cycle run is motivated by the consequent reduction in time per cycle to reduce the overall experimental run-time.[220] The volumes of the electrolytes contained in the respective reservoirs at any time can be calculated by subtracting the volume of electrolyte in the electrode pores from the total volume of electrolyte on each side. Due to the different sizes of the positive and negative electrodes, the reservoir volumes on each side are not the same.

5.3 Literature and Manufacturer-Provided Parameter Values

Table 5.3 lists the parameter values obtained from the literature and manufacturer datasheets along with their references.

Table 5.3: Parameter Values Obtained from Literature and Manufacturer Data

Parameter	Description	Value [Unit]	Reference/Comments
ϵ	Electrode porosity	0.78	Manufacturer data[226]
D_{Na}	Diffusion coefficient of Na^+	$1.33 \times 10^{-9}\left[\frac{\mathrm{m}^2}{\mathrm{s}}\right]$	Literature value[230]
D_{Cl}	Diffusion coefficient of Cl^-	$2.03 \times 10^{-9}\left[\frac{\mathrm{m}^2}{\mathrm{s}}\right]$	Literature value[230]
D_{TEOA}	Diffusion coefficient of free TEOA	$5.75 \times 10^{-10}\left[\frac{\mathrm{m}^2}{\mathrm{s}}\right]$	Literature value[231]
D_{OH}	Diffusion coefficient of OH^-	$5.27 \times 10^{-9}\left[\frac{\mathrm{m}^2}{\mathrm{s}}\right]$	Literature value[230]
d_{mem}	Membrane thickness	$5.08 \times 10^{-5}[\mathrm{m}]$	Manufacturer data[223]

5.4 Parameter Values Measured/Specified in RFB Study

Table 5.4: Parameters Specified in RFB Study

Parameter	Description	Value [Unit]	Reference/Comments
$D_{\text{Fe(III)-TEOA}}$	Diffusion coefficient of Fe(III)-TEOA	$7.1 \times 10^{-11}\left[\frac{\text{m}^2}{\text{s}}\right]$	Gong et al.[17]
$D_{\text{Fe(II)-TEOA}}$	Diffusion coefficient of Fe(II)-TEOA	$7.2 \times 10^{-11}\left[\frac{\text{m}^2}{\text{s}}\right]$	Gong et al.[17]
$D_{\text{Fe(III)-CN}}$	Diffusion coefficient of $Fe(CN)_6^{3-}$	$8.6 \times 10^{-10}\left[\frac{\text{m}^2}{\text{s}}\right]$	Gong et al.[17]
$D_{\text{Fe(II)-CN}}$	Diffusion coefficient of $Fe(CN)_6^{4-}$	$8.2 \times 10^{-10}\left[\frac{\text{m}^2}{\text{s}}\right]$	Gong et al.[17]
T	Operating temperature	293.15 [K]	Gong et al.[17]
$E_{\text{neg}}^{o\prime}$	Formal potential of Fe(II)-TEOA / Fe(III)-TEOA redox couple	-0.859 [V]	Gong et al.[17]
k_{pos}^{o}	Rate constant of $Fe(CN)_6^{4-}$/ $Fe(CN)_6^{3-}$ redox couple	$2.5 \times 10^{-3}\left[\frac{\text{m}}{\text{s}}\right]$	Gong et al.[17]
k_{neg}^{o}	Rate constant of Fe(II)-TEOA / Fe(III)-TEOA redox couple	$1.1 \times 10^{-4}\left[\frac{\text{m}}{\text{s}}\right]$	Gong et al.[17]
i_{app}	Applied current density	$4.00 \times 10^{2}\left[\frac{\text{A}}{\text{m}^2}\right]$	Gong et al.[17]
Q	Electrolyte flow rate through each compartment	$1.67 \times 10^{-6}\left[\frac{\text{m}^3}{\text{s}}\right]$	Gong et al.[17]

The parameter values that are specified in the study of this RFB system by Gong et al.[17] are summarized in Table 5.4. The temperature of the system is assumed to be 293.15 K based on the information provided by Gong et al.[17] The formal potentials of the Fe(II)-TEOA /Fe(III)-TEOA and $Fe(CN)_6^{4-}$/ $Fe(CN)_6^{3-}$ redox couples are determined from cyclic voltammetry by Gong et al.[17] The authors note, however, that the potential of the $Fe(CN)_6^{4-}$/ $Fe(CN)_6^{3-}$ redox couple is particularly sensitive to the ionic strength of the electrolyte, as found by Kolthoff and Tomsicek.[232] The concentrations of the redox species in the cyclic voltammetry study are twice as large as those in the RFB system.[17] Due to this large difference, we choose not to use the reported formal potential for the $Fe(CN)_6^{4-}$/ $Fe(CN)_6^{3-}$ redox couple and instead obtain this parameter by fitting the model to the experimental data for the operating RFB reported in the literature. No literature documenting the sensitivity of the Fe(II)-TEOA/Fe(III)-TEOA formal potential

to ionic strength could be found and for this reason the value determined by Gong et al.[17] is used in the model.

5.5 Parameter Values Obtained by Model Fitting

The parameter values obtained by fitting the model to experimental data are summarized in Table 5.5. The data used to fit the parameters consist of the experimental single-cycle charge and discharge voltage-time curves at 40 mA/cm^2, as well as the multiple-cycle behaviour observed, with the operating parameters specified in this chapter.

Table 5.5: Parameter Values Fit to Experimental Data

Parameter	Description	Value [Unit]	Reference/Comments
$E_{\mathrm{pos}}^{o\prime}$	Formal potential of $Fe(CN)_6^{4-}$/ $Fe(CN)_6^{3-}$ redox couple	0.44 [V]	Fit to single-cycle data
σ_m	Membrane conductivity	$1.35 \times 10^{-1} \left[\frac{\mathrm{S}}{\mathrm{m}}\right]$	Fit to single-cycle data
P	Permeation coefficient of TEOA through membrane	$1.85 \times 10^{-12} \left[\frac{\mathrm{m}^2}{\mathrm{s}}\right]$	Fit to single-cycle data
$i_{0,\mathrm{H_2}}$	Exchange current density of HER	$7.5 \times 10^{-3} \left[\frac{\mathrm{A}}{\mathrm{m}^2}\right]$	Fit to multiple-cycle data
$E_{\mathrm{rev,TEOA}}$	Equilibrium (reversible) potential of TEOA oxidation reaction	0.27 [V]	Fit to single-cycle data
α_{TEOA}	Transfer coefficient of TEOA oxidation reaction	0.61	Fit to single-cycle data

As described in Chapter 4, the membrane subdomain is treated as an ohmic element, in which the potential gradient is related to the current density vector field through the conductivity of the subdomain. This conductivity value accounts for all transport phenomena that occur in the membrane subdomain. This assumption is supported by experimental data for the RFB system obtained particularly from impedance and polarization experiments.[17] Impedance testing of the RFB shows that the ohmic resistance of $2.6\ \Omega \cdot \mathrm{cm}^2$ is significantly greater than the charge transfer resistance of $0.75\ \Omega \cdot \mathrm{cm}^2$, as depicted in Figure 5.2.

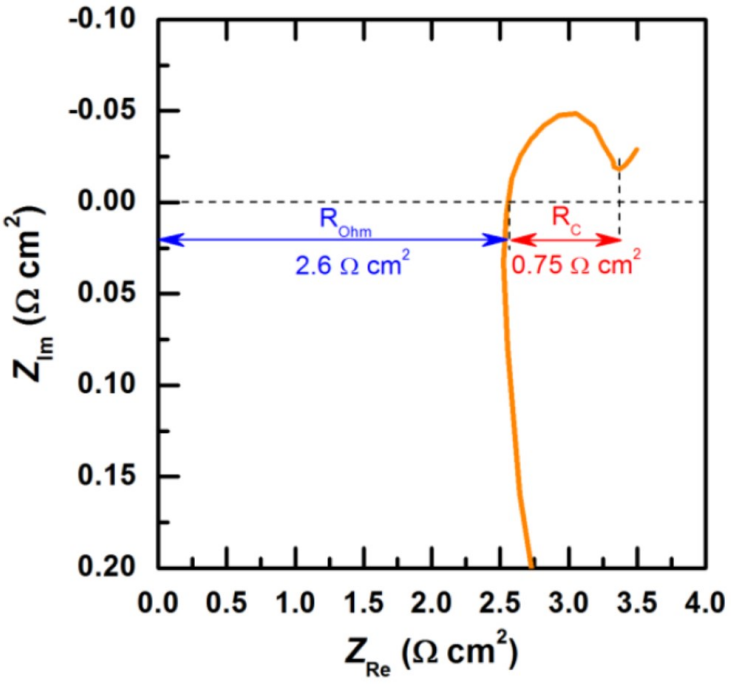

Figure 5.2: Impedance of all-iron all-soluble RFB. Reproduced from Gong et al.[17] with permission from the American Chemical Society.

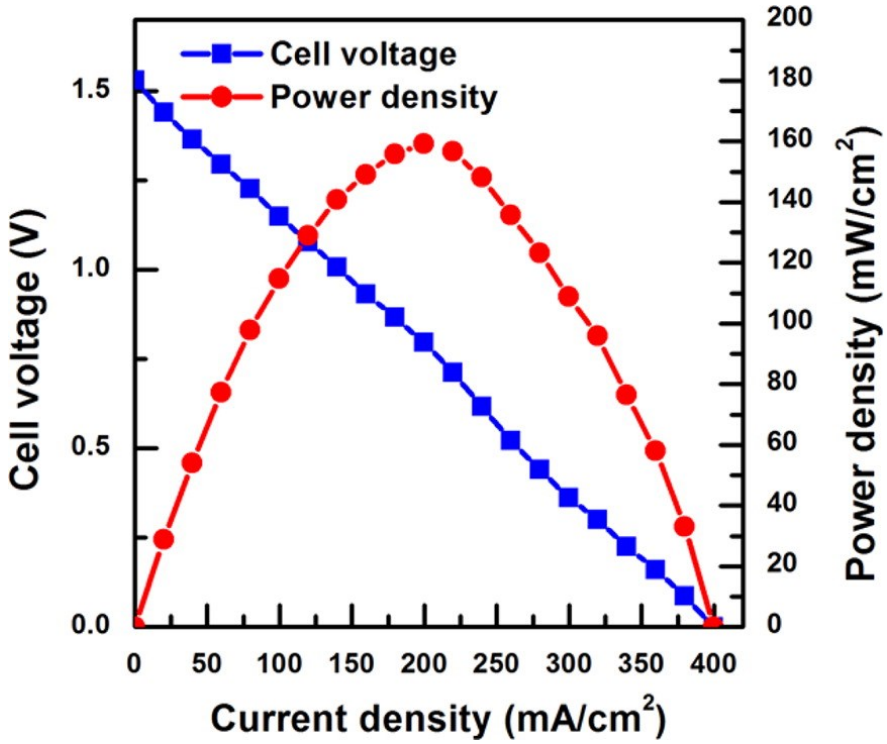

Figure 5.3: Polarization curve for all-iron all-soluble RFB. Reproduced from Gong et al.[17] with permission from the American Chemical Society.

Additionally, the polarization curve (shown in Figure 5.3) for the RFB system exhibits a largely linear dependence on current density, which is characteristic of ohmic behaviour. This further suggests that the system is limited primarily by the internal ohmic resistance. The authors[17] reason that the ohmic resistance within the electrode is relatively small due to the membrane electrode assembly (MEA) structure of the RFB[233] and conclude that the membrane resistance is primarily responsible for the internal resistance of the battery. Based on these factors, we assume that the membrane resistance can be modelled as an ohmic resistor with a single parameter value for conductivity. This value of the membrane conductivity is obtained by fitting the model to experimental data of the operating RFB.

We find that our model does not satisfactorily predict the observed RFB current efficiency when the permeation coefficient of TEOA across the membrane reported by Gong et al.[17] is used. Based on correspondence with one of the authors of the original study, we speculate that this discrepancy may be linked to the differences in the conditions between those of the permeation experiments and those of charge-discharge operation of the RFB.[220] For this reason, the permeation coefficient of TEOA is determined by fitting the model to experimental data of the operating RFB.

5.5.1 Model-Fitting Procedure and Results

Following a review of the literature, some parameter values for the model remain unknown. As mentioned above, these parameter values are determined by fitting the model to experimental data collected by Gong et al.[17] for the single-cycle run of the RFB system.

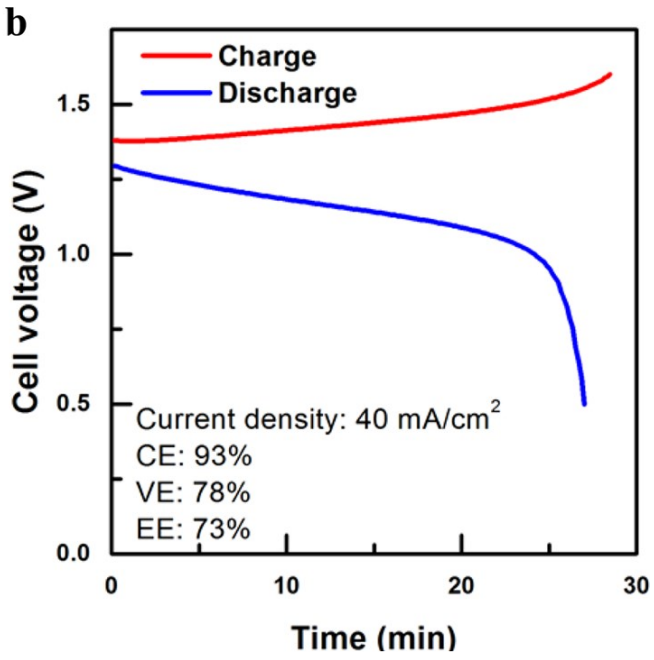

Figure 5.4: Single cycle charge and discharge curves for the all-iron all-soluble RFB. Reproduced from Gong et al.[17] with permission from the American Chemical Society.

The charge and discharge curves (Figure 5.4) have been digitized to provide voltage-time data points using *UN-SCAN-IT* software (Silk Scientific Inc). The voltage-time data for the discharge curve follow those of the charge curve to produce a voltage-time plot for a sequence consisting of charge followed by discharge. This is referred to as the single-cycle experimental curve. The model is configured to simulate this single-cycle run, which includes a charge duration equal to that of the experimental data and a subsequent discharge until the cell voltage reaches the cut-off level of 0.5 V used by Gong et al.[17] Using the probe feature in COMSOL, the voltage across the two electrodes is computed at every time step over the simulated duration. Most of the fitting is done by comparing the simulated cell voltage-time data to the single-cycle experimental charge-discharge curve for different sets of three of the fitting parameters ($E_{\mathrm{pos}}^{o\prime}$, σ_m, and P) and then adjusting their values as necessary. This manual fitting is performed instead of a built-in COMSOL automated fitting method because the many iterations required to arrive at a solution result in computation time that is substantial and prohibitive. This is due to the fact that every iteration of the fitting method requires the model to be fully solved over the

single-cycle run. Manual fitting also provides insight into the effects of parameters on the model behaviour that informs further tuning of these parameters to best fit the experimental data. The HER exchange current density is obtained by trial-and-error using the multiple-cycle charge-discharge behaviour and single-cycle concentration-time data from the model for each redox-active species. The computed multiple-cycle charge-discharge response is found to be sensitive to the HER exchange current density. The fitting procedures are carried out iteratively since a change in the value of one of the parameters could affect the sensitivity of the model to the others. Following fitting of the parameters, it is observed that they affect the characteristics and behaviour of the model in distinct ways. This greatly simplifies the fitting process as they can be fit independently one at a time. Each iteration of fitting consists of varying one parameter, with the other parameter values held constant, until the model fit is improved sufficiently; this process is then repeated with a different parameter varied at each fitting iteration. After cycling through the parameters multiple times, the fit of the model to the data cannot be improved any further, at which point the fitting process is complete.

The value for $E_{\mathrm{pos}}^{o\prime}$ is fit to the experimental data with an initial guess of 0.48 V, which corresponds to the formal potential of this reaction measured by Gong et al.[17] under conditions where the total redox-active species concentrations are twice as large as those in the RFB system. As shown in Figure 5.5, a change in the value of this parameter tends to shift the charge and discharge curves vertically. Not surprisingly, an increase in the formal potential causes the cell potential at every time step during charge and discharge to increase, while a decrease has the opposite effect. The fitting procedure yields a value of 0.44 V for the final model.

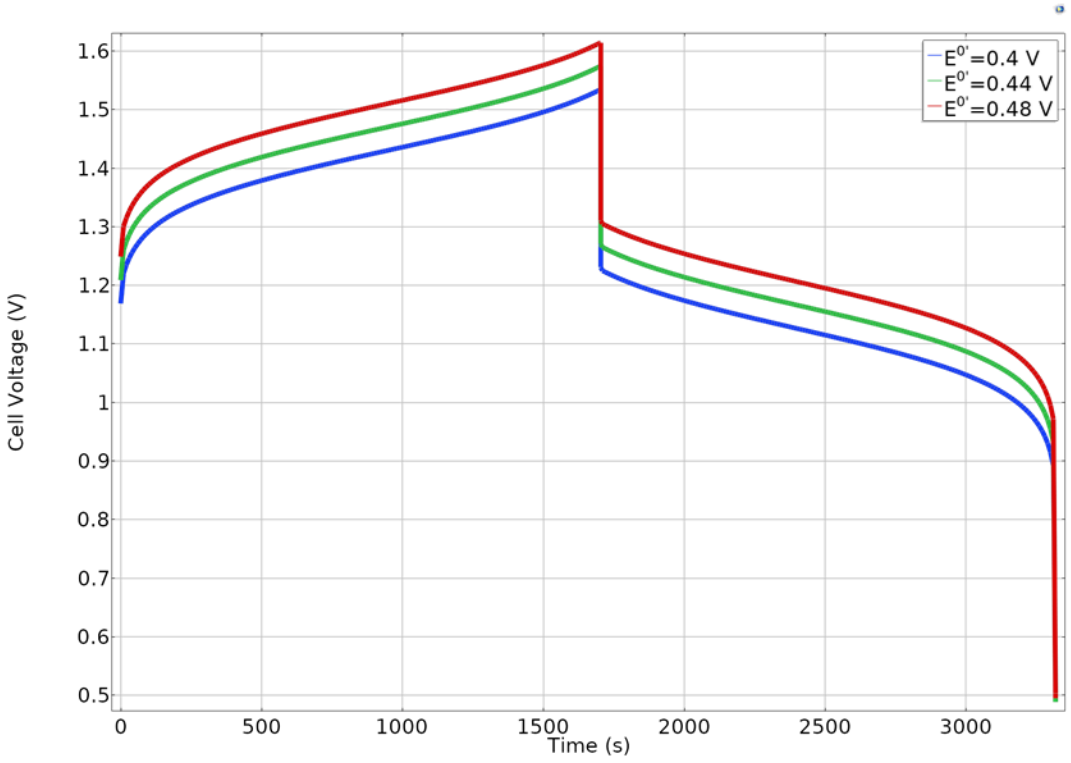

Figure 5.5: Parameter sweep of iron-cyanide reaction formal potential ($E^{o\prime}_{\mathrm{pos}}$) on single-cycle curve.

Fitting of the membrane conductivity is carried out in a similar manner to that used for the formal potential of the positive redox couple, although the initial guess for this parameter is less certain. The values of this parameter are varied over a wide range and a reasonable fit is ultimately obtained through trial and error.

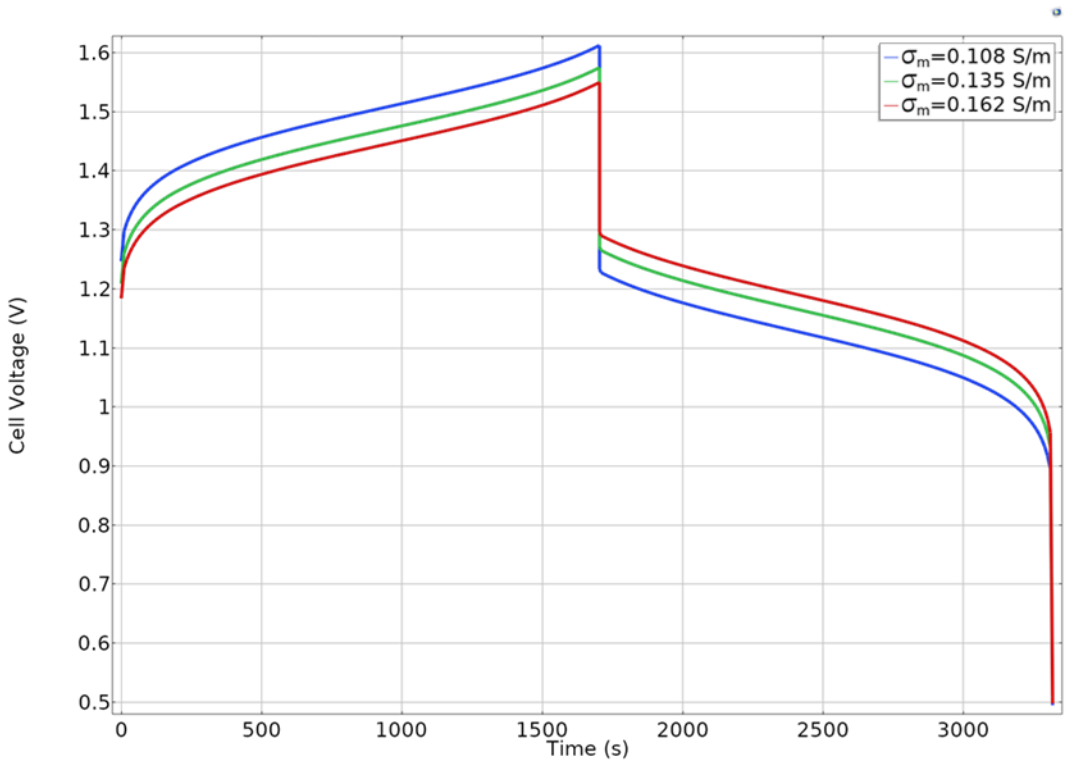

Figure 5.6: Parameter sweep of membrane conductivity (σ_m) on single-cycle curve.

As illustrated in Figure 5.6, the main effect of changing the membrane conductivity is on the magnitude of the step change in cell voltage when battery operation is switched from charge to discharge. This behaviour is not surprising given that the membrane has a large effect on battery performance due to its ohmic resistance. A larger conductivity results in lower membrane resistance and greater voltage efficiency. It is for this reason that the cell voltages during charge and discharge tend to approach each other as the conductivity is increased. The value for membrane conductivity obtained from fitting is $1.35 \times 10^{-1} \frac{\mathrm{S}}{\mathrm{m}}$. The proton conductivity of Nafion under standard operating conditions is approximately $8 \frac{\mathrm{S}}{\mathrm{m}}$ in literature.[224] The lower value obtained in the present work is reasonable given that the membrane is being used under alkaline conditions so that OH^- is the charge carrier rather than H^+.

The permeation coefficient of TEOA through the membrane is fit to the experimental data using the value obtained in the permeation study by Gong et al.[17] under non-operating conditions as the initial

guess. This parameter affects the current efficiency of the RFB model in particular. Not surprisingly, an increase in the permeation coefficient increases the rate of TEOA permeation and resulting oxidation, leading to a lower current efficiency of the charge-discharge cycle. As shown in Figure 5.7, discharge terminates sooner when the value of the TEOA permeation coefficient is higher for the same charge duration. The value of the fitted permeation coefficient is found to be $1.85 \times 10^{-12} \frac{\mathrm{m}^2}{\mathrm{s}}$. This is an order of magnitude smaller than the permeation coefficient value of $1.5 \times 10^{-13} \frac{\mathrm{m}^2}{\mathrm{s}}$ measured by Gong et al.[17] under conditions that differ from those used during RFB operation.

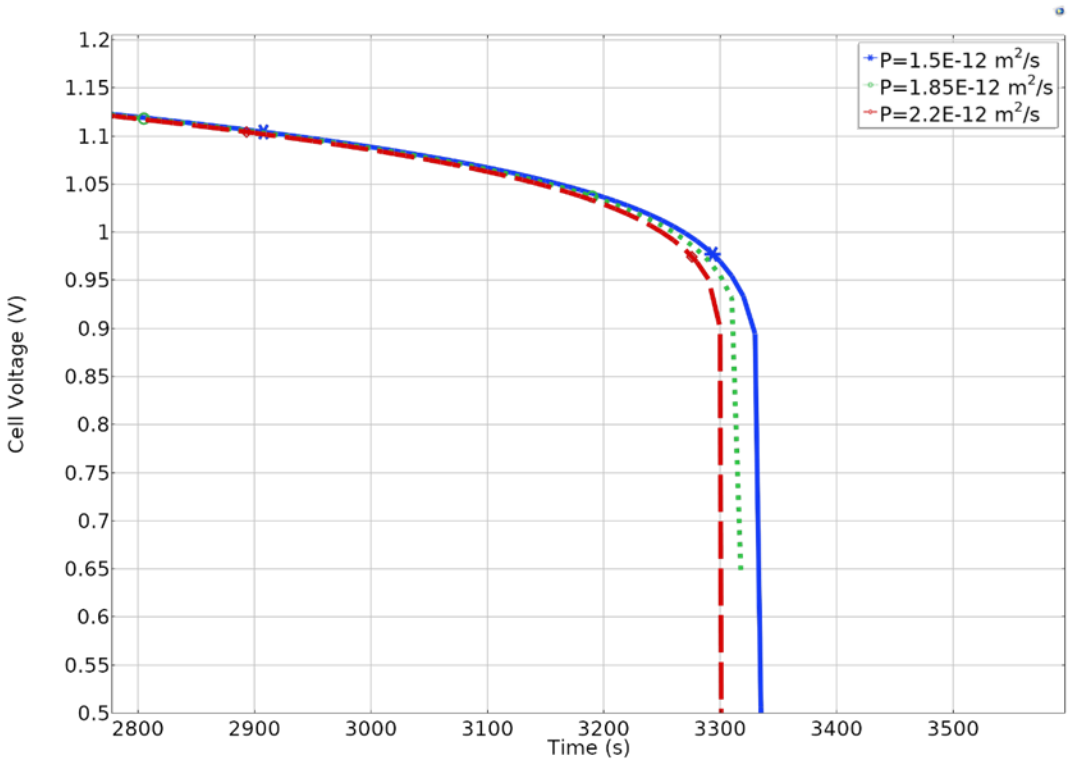

Figure 5.7: Parameter sweep of TEOA permeation coefficient (P) on single-cycle curve.

The exchange current density for the hydrogen evolution reaction at the negative electrode is fit differently from the aforementioned parameters since the single-cycle charge-discharge curve is not sensitive to this parameter. This parameter primarily affects the balance between the redox reactions at the two electrodes, which does not become apparent until the battery has been subjected to a number

of charge-discharge cycles. The concentration-time data for the chemical species involved in the iron-triethanolamine and iron-cyanide redox couples over the duration of the single-cycle run is initially used to screen values of the HER exchange current density based on the imbalance observed at the end of the cycle. The model is then fit to experimental multiple-cycle data to estimate this parameter. If the HER exchange current density were too small, a significant imbalance would occur between the $Fe(CN)_6^{3-}$ and Fe(II)-TEOA concentrations at the end of discharge. As this parameter increases, the imbalance in concentrations is reduced until the point is reached where the HER side reaction becomes too dominant and the discharge time of the battery becomes limited. It is known from the investigation of Gong et al.[17] that the positive electrode limits the discharge of the RFB, implying that $Fe(CN)_6^{3-}$ becomes depleted prior to Fe(II)-TEOA. As a result of this analysis, any value of the exchange current density for the HER that causes depletion of Fe(II)-TEOA prior to $Fe(CN)_6^{3-}$ at the end of discharge is too large, providing an upper bound for this value. Through successive iterations of multiple-cycle model simulations using various values of the HER exchange current density, a value of $1.1 \times 10^{-1} \frac{\mathrm{A}}{\mathrm{m}^2}$ is found to provide long-term stability of the model with respect to the experimental multi-cycle charge-discharge data.

5.6 Initialization Parameter Values

As shown in eq (4.16), the reversible potential for any half-cell reaction obtained from the Nernst equation does not have a finite value when the concentration of any reactant or product is zero; as a consequence, the model cannot be solved when species involved in redox couples have concentrations of zero. For this reason, the model is initialized assuming a small arbitrary state-of-charge (SOC) value of 0.0075. This value is chosen by trial and error to establish a value small enough to not appreciably affect model accuracy, yet large enough to prevent model instability due to the Nernst equation. This value has no significant impact on the model behaviour, but it allows the model simulations to get underway.

Based on this choice of SOC, the initial species concentrations used to initialize the model are calculated using eqs (5.1) and (5.2) and are given in Table 5.6.

$$c_{i,\text{initial}} = (\text{SOC})c_{i,\text{total}} \tag{5.1}$$

$$c_{i,\text{initial}} = (1 - \text{SOC})c_{i,\text{total}} \tag{5.2}$$

where $c_{i,\text{total}}$ is the total concentration of this redox species across both oxidation states. The initial concentration $c_{i,\text{initial}}$ of redox-active species i is related to the SOC by eq (5.1) if the species is produced during charge or eq (5.2) if it is consumed during charge.

Table 5.6: Initial Parameter Values

Parameter	Description	Value [Unit]
$c_{\text{FeT1,initial}}^{\text{neg}}$	Initial Fe(III)-TEOA concentration (negative electrode)	$1.985 \times 10^2 \left[\frac{\text{mol}}{\text{m}^3}\right]$
$c_{\text{FeT2,initial}}^{\text{neg}}$	Initial Fe(II)-TEOA concentration (negative electrode)	$1.5 \left[\frac{\text{mol}}{\text{m}^3}\right]$
$c_{\text{Na,initial}}^{\text{neg}}$	Initial Na^+ concentration (negative electrode)	$1.500 \times 10^3 \left[\frac{\text{mol}}{\text{m}^3}\right]$
$c_{\text{OH,initial}}^{\text{neg}}$	Initial OH^- concentration (negative electrode)	$1.500 \times 10^3 \left[\frac{\text{mol}}{\text{m}^3}\right]$
$c_{\text{Cl,initial}}^{\text{neg}}$	Initial Cl^- concentration (negative electrode)	$6.00 \times 10^2 \left[\frac{\text{mol}}{\text{m}^3}\right]$
$c_{\text{TEOA,initial}}^{\text{neg}}$	Initial TEOA concentration (negative electrode)	$8.00 \times 10^2 \left[\frac{\text{mol}}{\text{m}^3}\right]$
$c_{\text{FeCN3,initial}}^{\text{pos}}$	Initial $Fe(CN)_6^{3-}$ concentration (positive electrode)	$1.5 \left[\frac{\text{mol}}{\text{m}^3}\right]$
$c_{\text{FeCN4,initial}}^{\text{pos}}$	Initial $Fe(CN)_6^{4-}$ concentration (positive electrode)	$1.985 \times 10^2 \left[\frac{\text{mol}}{\text{m}^3}\right]$
$c_{\text{Na,initial}}^{\text{pos}}$	Initial Na^+ concentration (positive electrode)	$3.800 \times 10^3 \left[\frac{\text{mol}}{\text{m}^3}\right]$

$c_{\mathrm{OH,initial}}^{\mathrm{pos}}$	Initial OH^- concentration (positive electrode)	$3.000 \times 10^3 \left[\frac{\mathrm{mol}}{\mathrm{m}^3}\right]$
$c_{\mathrm{TEOA,initial}}^{\mathrm{pos}}$	Initial TEOA concentration (positive electrode)	$0 \left[\frac{\mathrm{mol}}{\mathrm{m}^3}\right]$
SOC	Initial state of charge	0.0075

6 Model Validation and Behaviour

6.1 Single-Cycle Run

Based on the fitted model parameters, the single-cycle charge-discharge curve predicted by the model is shown in Figure 6.1 along with the corresponding experimental data obtained by Gong et al.[17] It can be seen the model fits the experimental data well overall. Agreement between the fitted curve and experimental curve during charge is excellent after the first ~ 100 s, while the fit is also very good during discharge. Some deviation is observed at the end of the cycle where the drop in the RFB voltage begins sooner and is more gradual in the experimental data than in the model curve. This could be due to transport limitations of reactant species from the bulk electrolyte into the pores of the electrodes, which is not considered in the model. This would cause the voltage to begin to drop sooner during discharge. As stated previously, the half-cell potential measurements of the RFB taken at the end of discharge imply that the positive electrode potential is primarily responsible for the drop in cell voltage. The negative electrode has a relatively flat half-cell potential curve at the end of discharge. This evidence may suggest that the transport of ferricyanide into the electrode pores at the end of discharge is slow and this results in the experimentally observed drop in cell voltage over a longer duration than the model reflects. The topic of mass transfer limitations has been investigated in porous electrodes[234,235] and specifically in redox flow batteries.[236,237] Flow battery models incorporating mass transfer coefficients have also been proposed.[205,238]

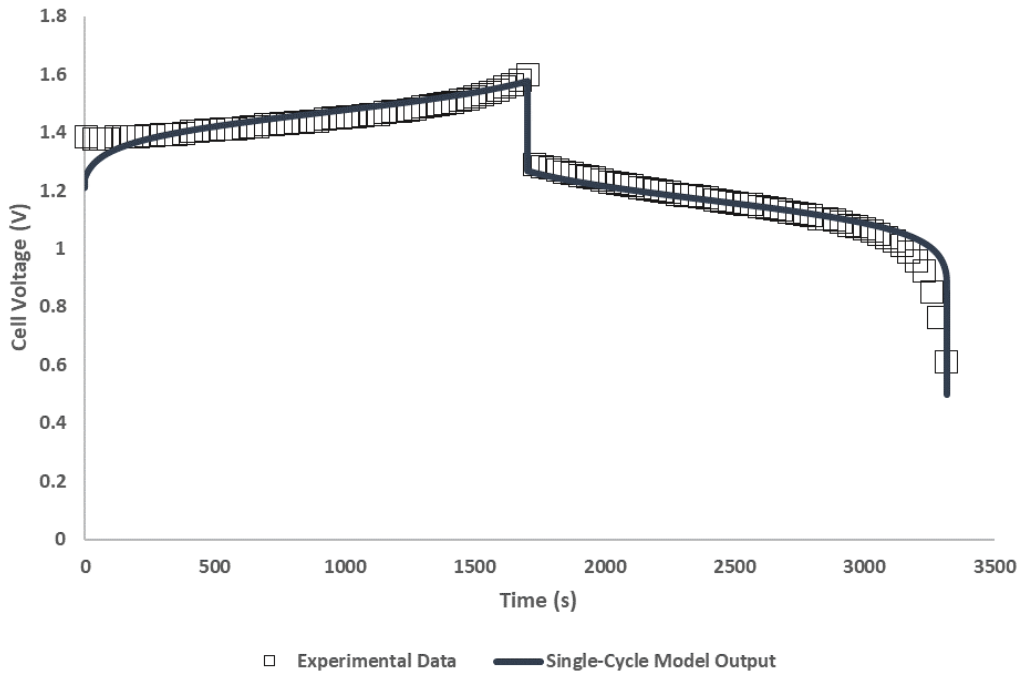

Figure 6.1: Fit of the model to experimental single-cycle data.

Using the cut line feature in COMSOL Multiphysics, it is possible to extract data corresponding to one-dimensional spatial profiles of the dependent variables within the battery at different times during the charge/discharge cycle, with the other spatial coordinate held constant at specified values. Several cut lines are considered to examine the extent to which variables such as the electrode potential vary spatially within each electrode subdomain at a given point in time. The constructed cut lines are summarized in Table 6.1 below and presented in Figure 6.2.

Table 6.1: Cut Line Descriptions

Cut Line Number	Description
CL1	Horizontal cut line along electrolyte outlet
CL2	Horizontal cut line at 3/4 height of RFB
CL3	Horizontal cut line at 1/2 height of RFB
CL4	Horizontal cut line at 1/4 height of RFB
CL5	Horizontal cut line along electrolyte inlet
CL6	Vertical cut line through negative electrode, 1/3 of electrode width from left boundary
CL7	Vertical cut line through negative electrode, 1/3 of electrode width from membrane

CL8	Vertical cut line through positive electrode, 1/3 of electrode width from membrane
CL9	Vertical cut line through positive electrode, 1/3 of electrode width from right boundary

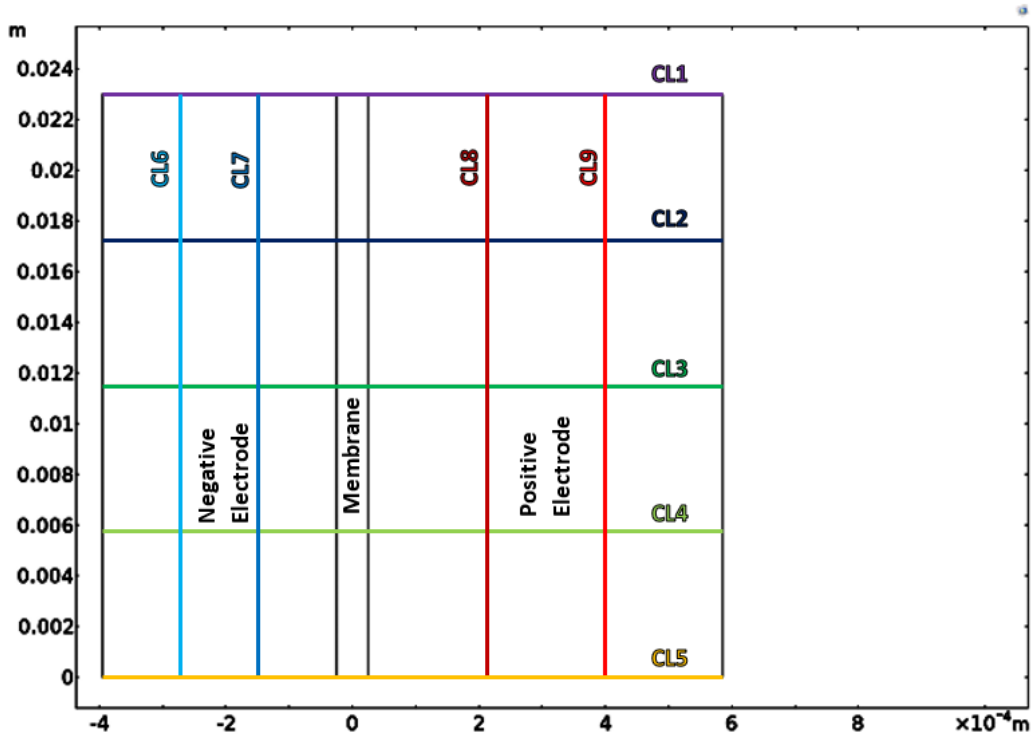

Figure 6.2: Cut lines examined in model domain.

The electrode potential of each porous electrode obtained by subtracting the electrical potential ϕ_l in the electrolyte phase from the electrical potential ϕ_s of the solid phase at the same location is observed to remain essentially uniform within each electrode at all times during the cycle, with the exception of the very end of discharge. The electrode potential profile remains uniform in the x-direction at the end of discharge but varies significantly in the y-direction at the same time. The electrode potential profiles in the positive and negative electrodes along cut lines CL1, CL2, CL3, CL4, and CL5 are shown in Figures 6.3, 6.4, 6.5, 6.6, and 6.7, respectively.

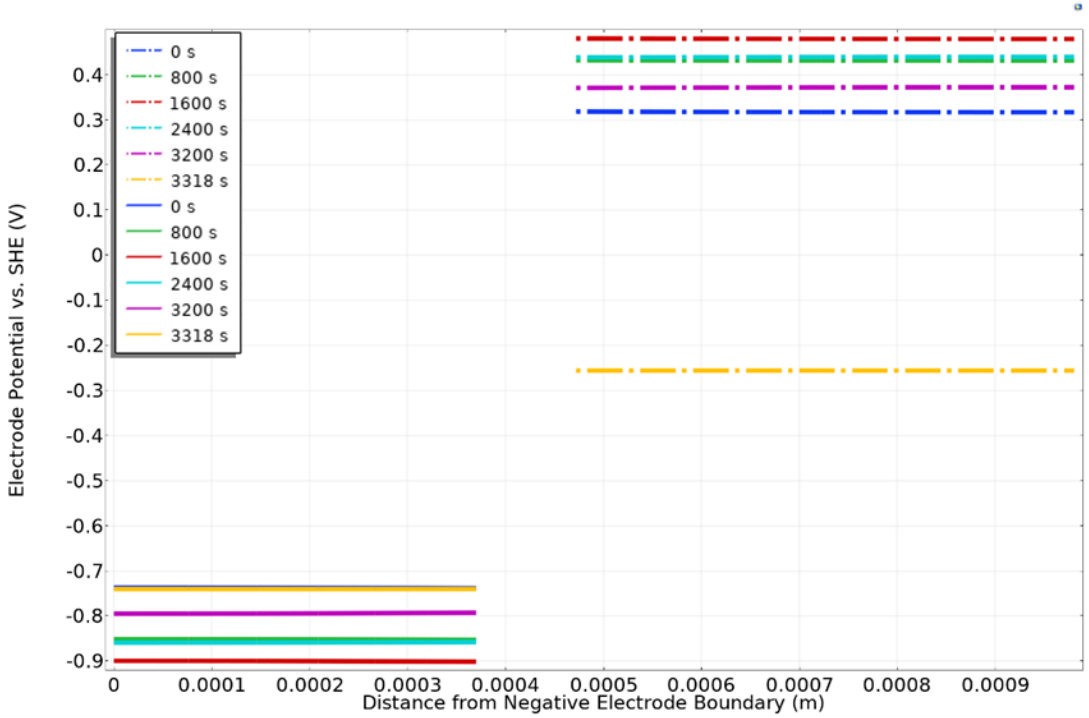

Figure 6.3: Electrode potentials along CL1. Solid lines apply to negative electrode and dot-dashed lines apply to positive electrode.

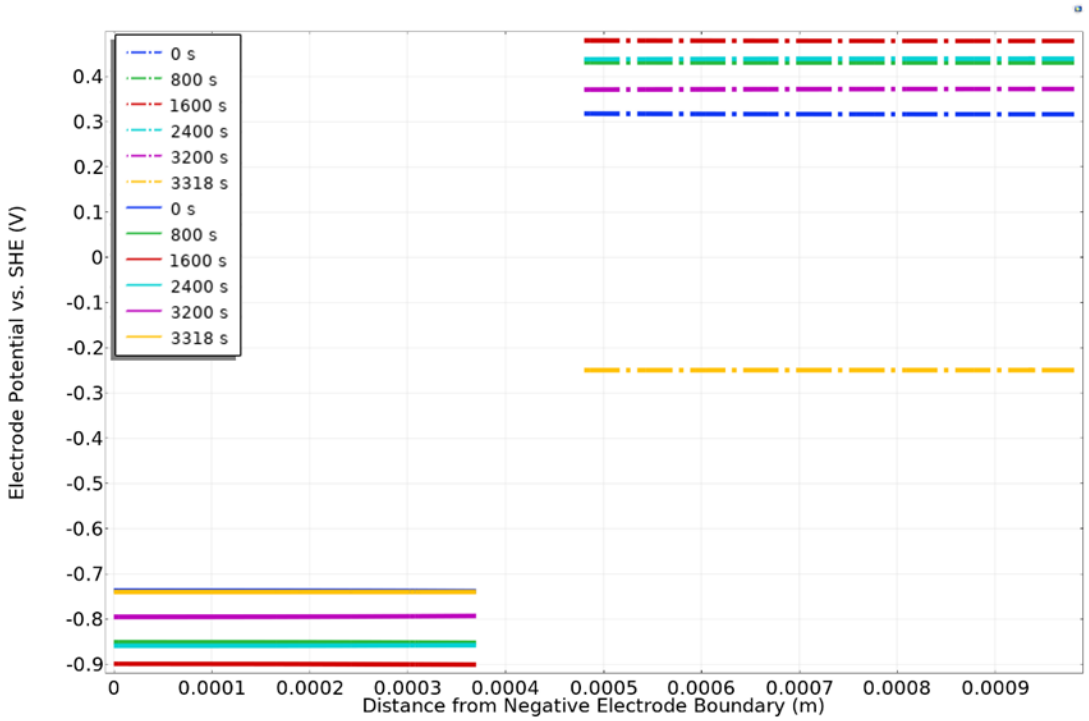

Figure 6.4: Electrode potentials along CL2. Solid lines apply to negative electrode and dot-dashed lines apply to positive electrode.

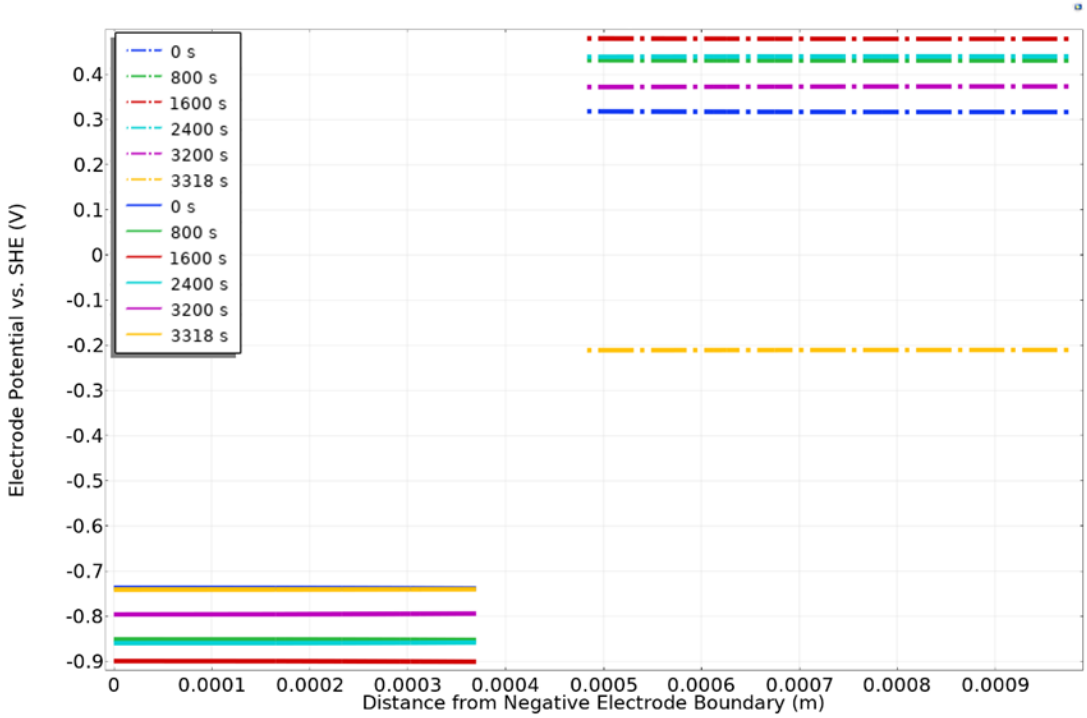

Figure 6.5: Electrode potentials along CL3. Solid lines apply to negative electrode and dot-dashed lines apply to positive electrode.

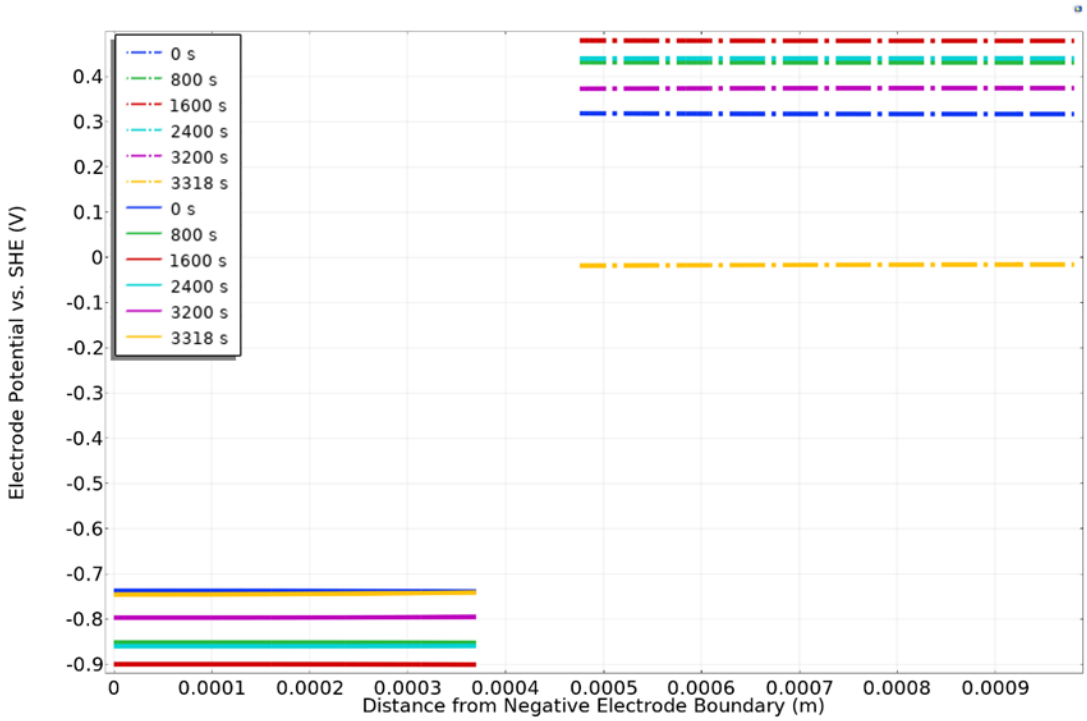

Figure 6.6: Electrode potentials along CL4. Solid lines apply to negative electrode and dot-dashed lines apply to positive electrode.

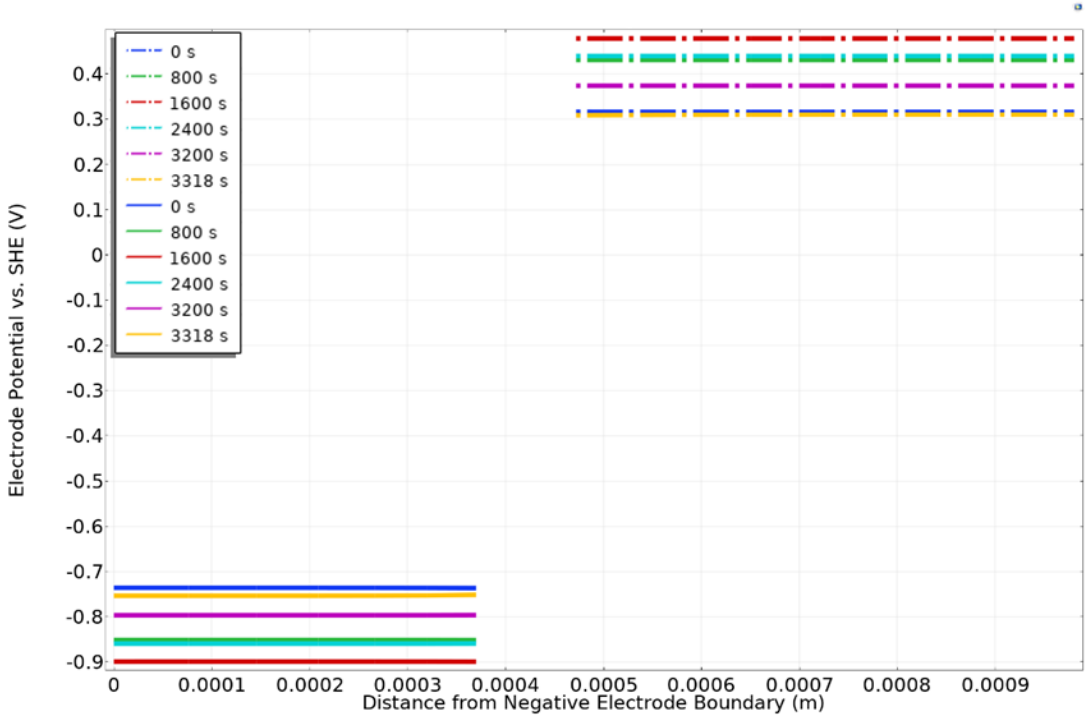

Figure 6.7: Electrode potentials along CL5. Solid lines apply to negative electrode and dot-dashed lines apply to positive electrode.

The common aspect of these cut lines is that they are oriented along the direction of current flow. For both electrodes, it can be seen that the variation in the electrode potential is insignificant along the direction in which current flows. The electrode potentials do change with time, as expected from the charge and discharge processes. The negative electrode potential becomes more negative as it is charged (shown in the 0 s, 800 s, and 1600 s lines) and becomes less negative as it is discharged (shown in the 2400 s, 3200 s, and 3318 s lines). Similarly, the positive electrode potential becomes more positive as it is charged and less positive as it is discharged. The electrode potential profiles in the negative electrode along cut lines CL6 and CL7, which lie in a plane tangent to the direction of electrolyte flow and normal to the direction of current flow, are shown in Figures 6.8 and 6.9, respectively. Similarly, the electrode potential profiles in the positive electrode along cut lines CL8 and CL9, which also lie in a plane tangent to the direction of electrolyte flow and normal to the direction of current flow, are shown in Figures 6.10 and 6.11, respectively.

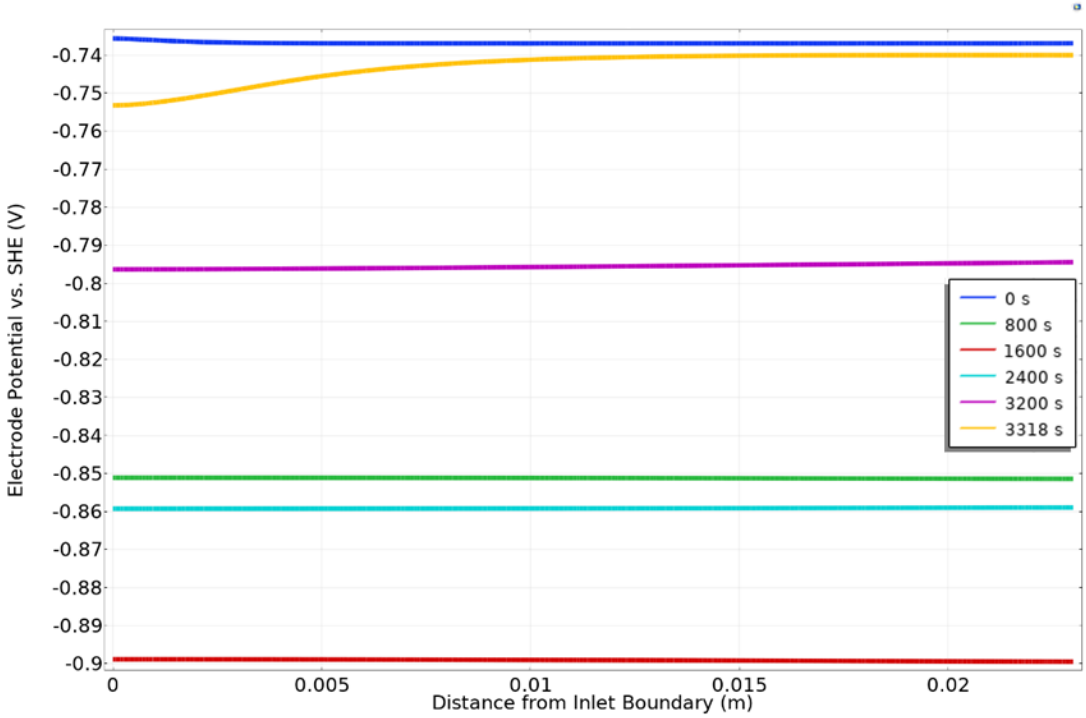

Figure 6.8: Electrode potentials along CL6.

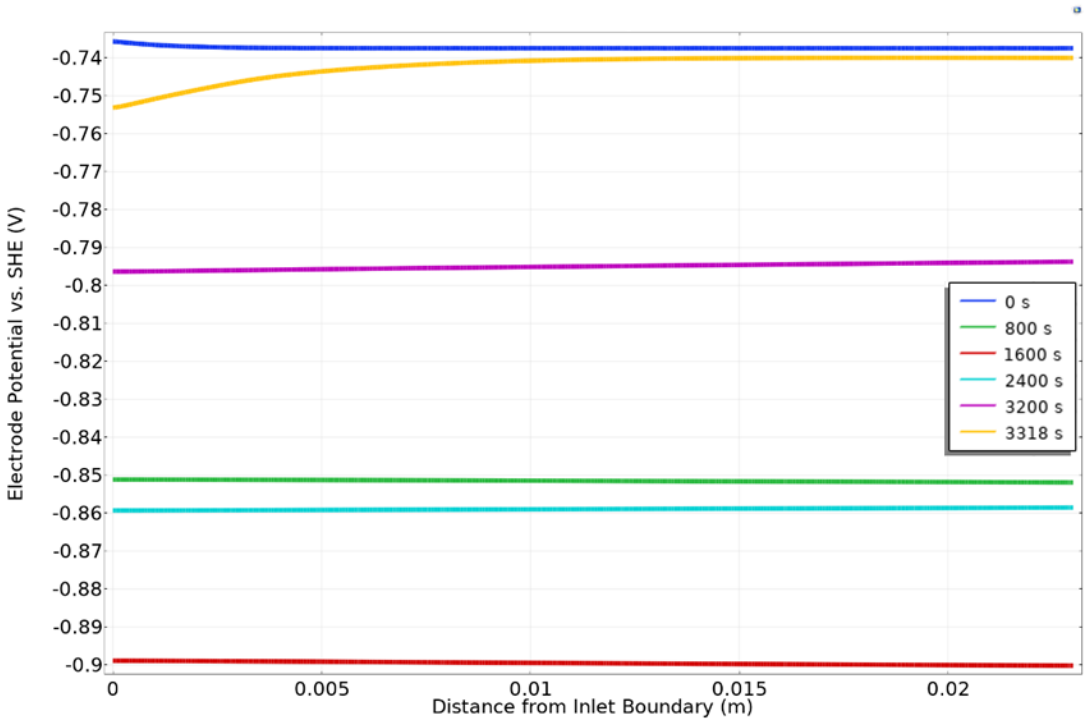

Figure 6.9: Electrode potentials along CL7.

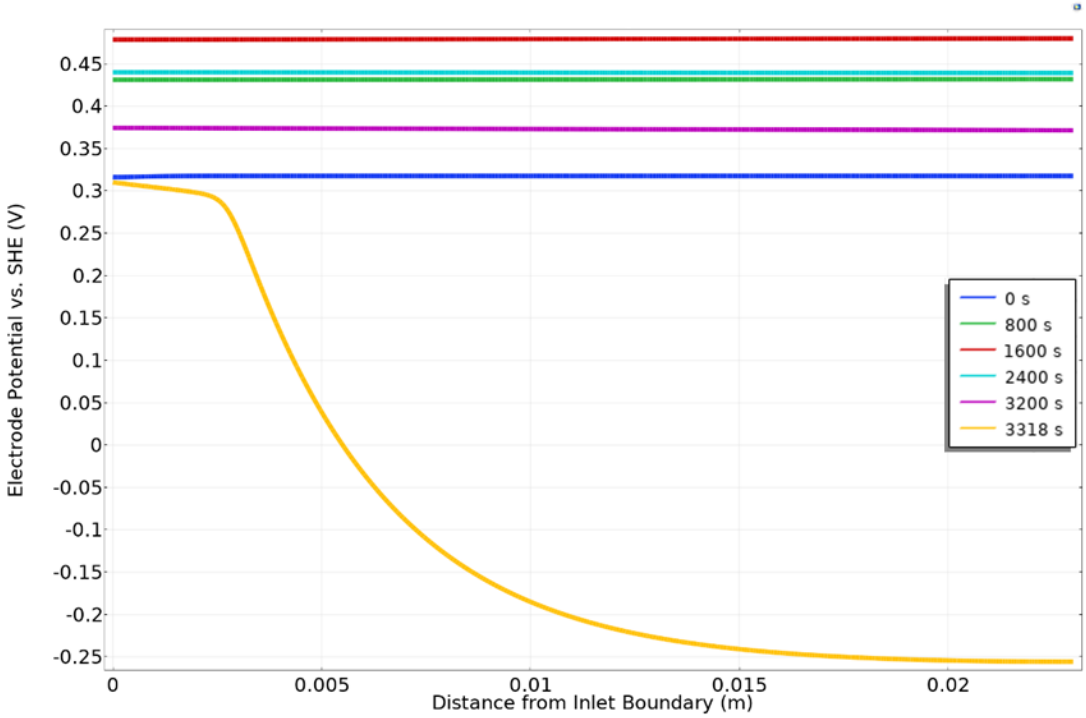

Figure 6.10: Electrode potentials along CL8.

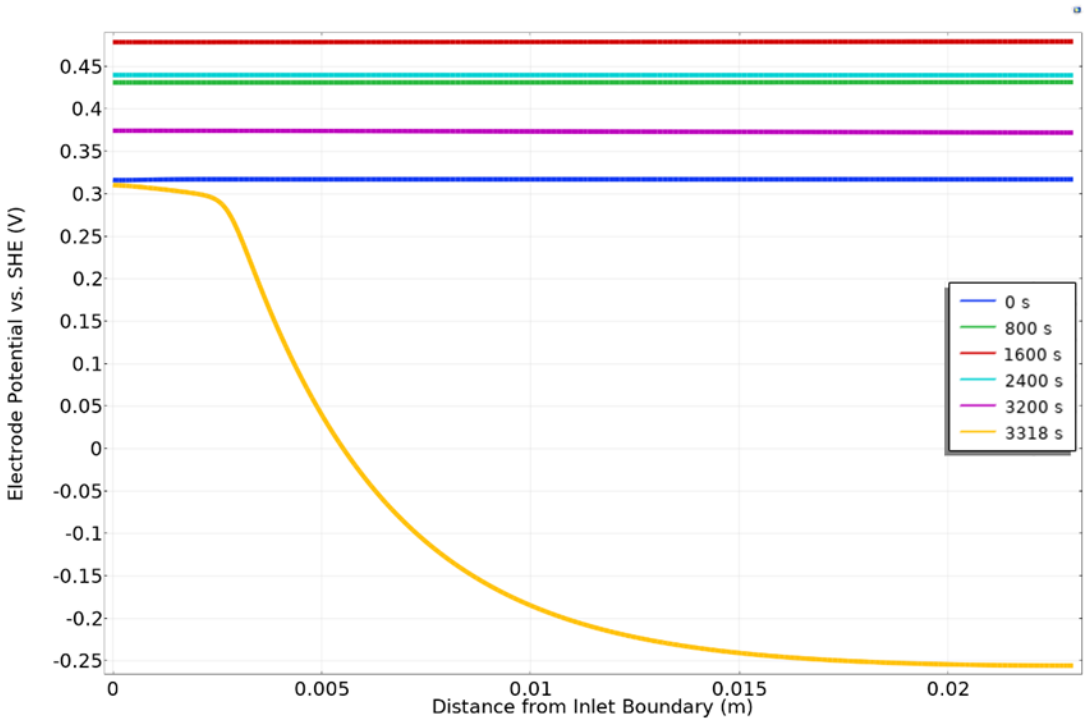

Figure 6.11: Electrode potentials along CL9.

It can be seen from these figures that the variation in electrode potential throughout both the positive and negative electrodes is minimal in this direction at all times, with the exception of the end of discharge. It can be seen from Figures 6.8–6.11 that at the time when the discharge voltage threshold is met for the RFB system the electrode potentials at both electrodes display a significant change along the direction of electrolyte flow. The change in electrode potential on the positive side is greater in magnitude and steeper at the end of discharge than on the negative side. This can be explained by the fact that the positive electrode is the limiting electrode that depletes nearly all of its Fe(III)-CN while the negative electrode still has some Fe(II)-TEOA remaining. The dependence of electrode potential on redox reactant concentrations results in these differences between the positive and negative electrode potential profiles at the end of discharge.

The spatial trends for electrode potential in the model may be explained by a combination of the facile kinetics and high electrical conductivity of the electrode, as well as the stability of species concentrations throughout most of the cycle. Each of these factors contributes to the losses that affect the electrode potential. The facile kinetics of the primary redox reactions at each electrode result in less variation in electrode potential due to the relationship between current density and activation overpotential. It can be seen from eqs (4.13) and (4.14) that lower overpotentials are required to achieve a given current density when the reaction has a larger rate constant (k_j^0). This is due to the fact that a reaction with facile kinetics will require less driving force in the form of the electrode potential to take place. In the present system, reaction kinetics should therefore not be expected to cause significant spatial variation in electrode potential. The relatively high electrical conductivity of the porous electrode suggests low potential variation due to ohmic losses. Inspection of eq (4.11) reveals that the current balance in the model specifies an inverse relationship between electrode conductivity σ_e and the gradient of solid-phase electrical potential ϕ_s with respect to the solid-phase current density $\boldsymbol{i_s}$. This represents the variation in solid-phase potential due to ohmic losses. This affects the electrode potential

as a consequence, since electrode potential depends on the solid-phase potential. The high conductivity of the electrode in both directions thus does not result in significant spatial variation in electrode potential. This is confirmed by Figure 6.12, which shows the solid-phase potential at the end of discharge, when the spatial variation in electrode potential is most pronounced. The minimum and maximum values are identified at the bottom and top of each colour legend to illustrate the small magnitude of variation in these values. It should be noted that the scales of the two colour legends differ due to the fact that the two electrodes are at very different potentials and the variation in solid-phase potential on each side is so small. The left legend uses microvolts (10^{-6} V) and the right legend uses volts (V). It can be seen that the solid-phase potential of the negative electrode varies by no more than ~ 0.3 mV, while that of the positive electrode varies by no more than ~ 0.6 mV. These values suggest that ohmic losses through the electrode do not contribute substantially to the electrode potentials in the model.

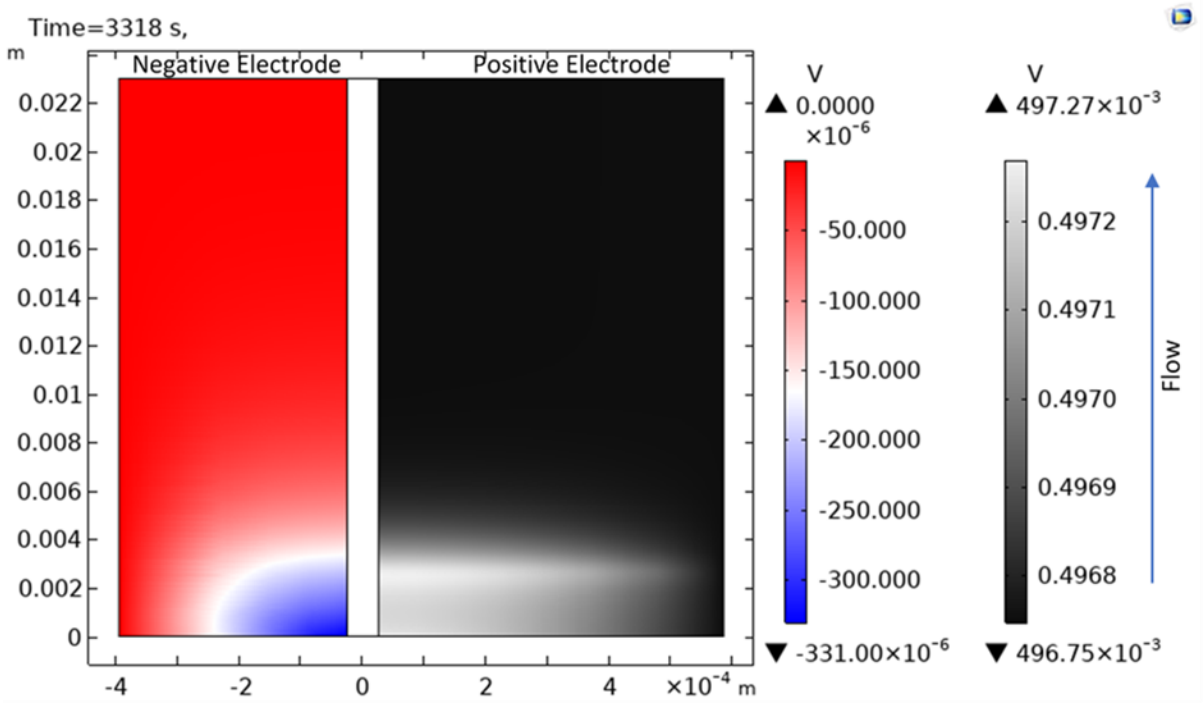

Figure 6.12: Solid-phase potential at the end of discharge for both porous electrodes. The left and right legends correspond to the negative and positive electrodes, respectively.

This plot shows that the spatial variation in electrode potential due to resistance in the solid phase is negligible in the present system. Lastly, the fast recirculation and consequently low residence time of the electrolyte in the electrode lead to a small spatial variation in the concentration of redox species (see Figures 6.17–6.24 that follow) for most of the cycle. The residence time is given by the ratio of the reaction volume to flow rate and represents the average length of time spent by a unit volume in the reaction domain. Larger residence time generally leads to greater conversion of reactants and consequently larger differences in inlet and outlet reactant concentrations. The fast flow rate of 100 mL/min relative to the small liquid volume in each electrode (0.15-0.22 mL) results in electrolyte residence times much less than one second; for this reason, little variation in redox species concentrations is observed. The equilibrium potential $E_{\mathrm{rev},j}$ of each redox couple that affects the electrode potential is calculated from eq (4.16). This equation shows that the concentrations of reactants and products of redox reactions affect the electrode potential. Due to the low electrolyte residence time in each electrode, spatial variation in reactant and product concentrations is relatively low. This explains why very little spatial variation in electrode potential is observed for the majority of the cycle. It can further be seen from eq (4.16) that as a redox reaction asymptotically approaches complete conversion of its reactants in either direction, such as at the end of discharge, the equilibrium potential grows significantly in magnitude. This explains why the electrode potential increases significantly in magnitude at the end of discharge. At the end of discharge, the electrode potential changes rapidly in the direction of flow because the electrolyte is so deficient in reactants relative to products that the small change in their concentrations as they flow and react becomes enough to change the electrode potential dramatically. Obviously, the reactant conversion in the electrolyte increases as the distance from the inlet side increases. At this point, the electrode potential is very sensitive to reactant concentration, resulting in the electrode potential profiles observed at the end of

discharge. Figures 6.13, 6.14, and 6.15 support the presented explanation for electrode potential trends at the end of discharge.

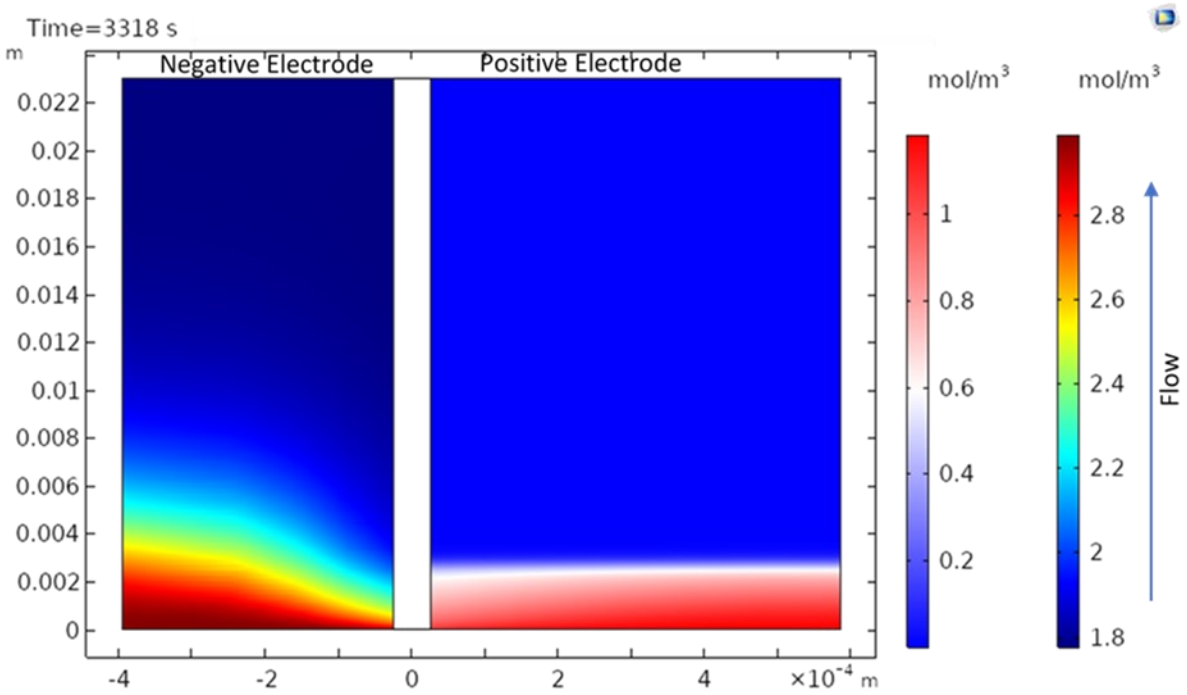

Figure 6.13: Concentrations of limiting reactants Fe(II)-TEOA (left) and Fe(III)-CN (right) at the end of discharge. The left and right legends correspond to the positive and negative electrodes, respectively.

Figure 6.13 confirms that the concentrations of redox reactants, particularly Fe(III)-CN at the positive electrode, drop to very low levels in the direction of flow at the end of discharge. At the positive electrode this corresponds to virtually complete depletion of Fe(III)-CN. Due to the limiting behaviour of the Nernst equation (eq (4.16)) as the reaction approaches complete conversion of reactants, the sensitivities of the equilibrium and electrode potentials to small changes in reactant concentration increase significantly.

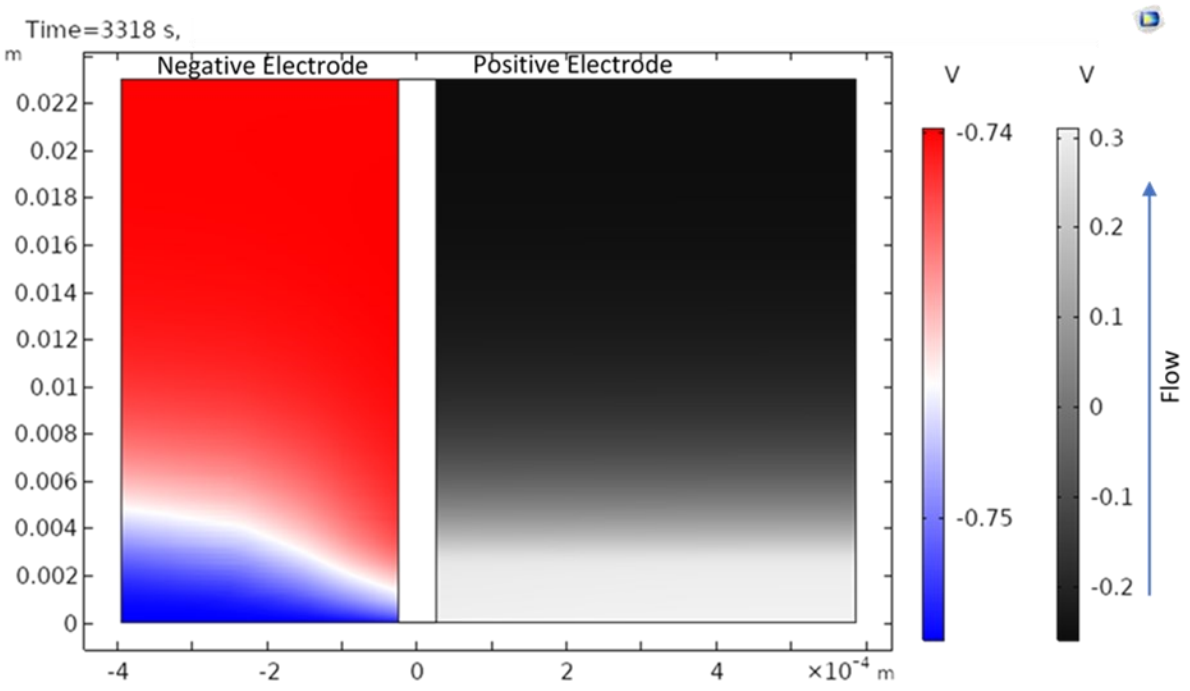

Figure 6.14: Equilibrium potentials of primary redox couples at the end of discharge. The left and right legends correspond to the negative and positive electrodes, respectively.

Figure 6.14 plots the equilibrium potentials for the main redox reactions at both electrodes at the end of discharge, while Figure 6.15 plots the electrode potentials at the end of discharge. It is observed that these figures display the same spatial trend and have similar numerical values, further supporting the conclusion that spatial variation in electrode potential is mostly due to the behaviour of the equilibrium potentials of the primary redox couples. Since the electrode potential is the sum of the equilibrium potential and overpotential for a reaction, as specified in eq (4.15), these results also suggest that the overpotentials for the primary redox reactions do not contribute significantly to the behaviour of the electrode potential. This is the expected behaviour for reactions with facile kinetics.

One of the significant observations reported by Gong et al.[17] from their experiments on this RFB system is that the reaction at the positive electrode is the limiting process at the end of discharge for the single-cycle run. This realization has helped shape the formulation of the model, as discussed earlier in this work. As expected from this observation, the drop in the positive electrode potential at the end of

discharge is much more pronounced than the relatively small change in the negative electrode potential at the same time. This can be seen from comparison of the plots of electrode potential along cut lines CL6 and CL7 (Figures 6.8 and 6.9) to those along cut lines CL8 and CL9 (Figures 6.10 and 6.11). This effect is also clearly depicted in Figure 6.15, which presents two-dimensional plots of the electrode potentials within both of the electrodes when the discharge voltage threshold is reached.

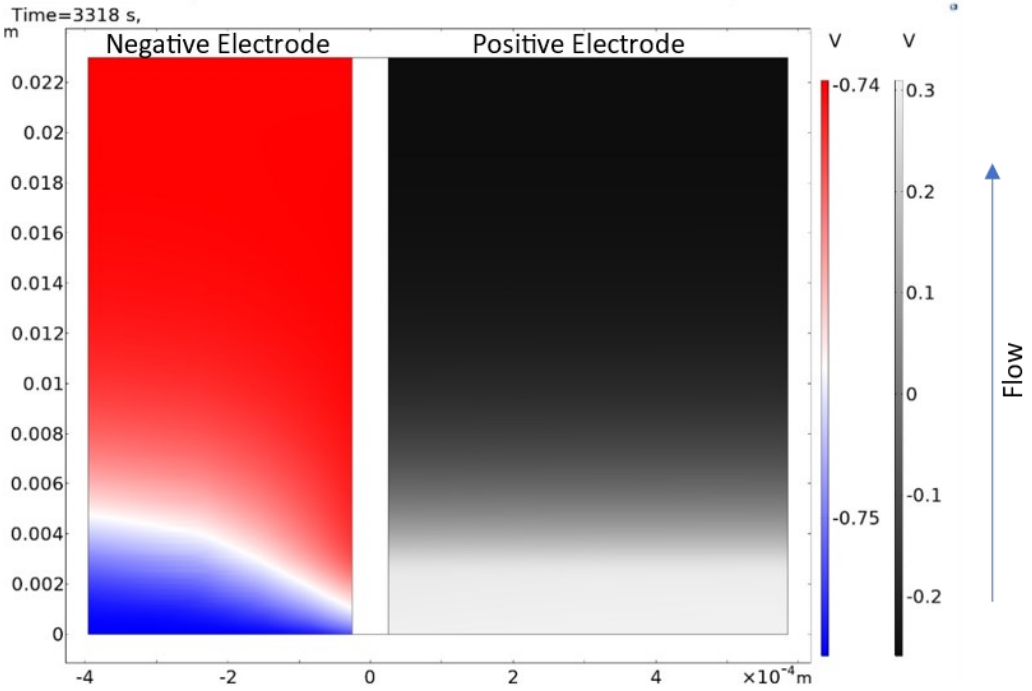

Figure 6.15: Electrode potentials at the end of the single-cycle discharge. The left and right legends correspond to the negative and positive electrodes, respectively.

Whereas the negative (left) electrode potential varies by only ~ 10 mV over the entire electrode at the end of discharge, the potential within the positive electrode varies by hundreds of millivolts over its volume. The potential decrease along the direction of flow through the positive electrode occurs primarily due to the near-complete depletion of Fe(III)-CN in the electrolyte leaving the outlet by the time the discharge threshold is reached, as explained earlier. Using the “average” component coupling operator in COMSOL Multiphysics, it is also possible to evaluate the spatial averages of the electrode potentials within the positive and negative electrodes as a function of time. These spatially-averaged

electrode potentials are plotted against time for the single-cycle run in Figure 6.16 along with the measured electrode potentials from Gong et al.[17] It should be noted that the experimental values presented in Figure 6.16 have been converted from values reported with respect to the Ag/AgCl reference electrode. Figure 6.16 and the remainder of plots in the present work refer to potentials relative to the standard hydrogen electrode (SHE). Gong et al.[17] state that the Ag/AgCl reference electrode used in their study has a potential of 0.194 relative to SHE. This value is used to convert this experimental data for comparison to the model output. The individual electrode potentials reported by Gong et al.[17] are only available for the end of discharge, so it is not possible to validate Figure 6.16 with respect to the entire cycle.

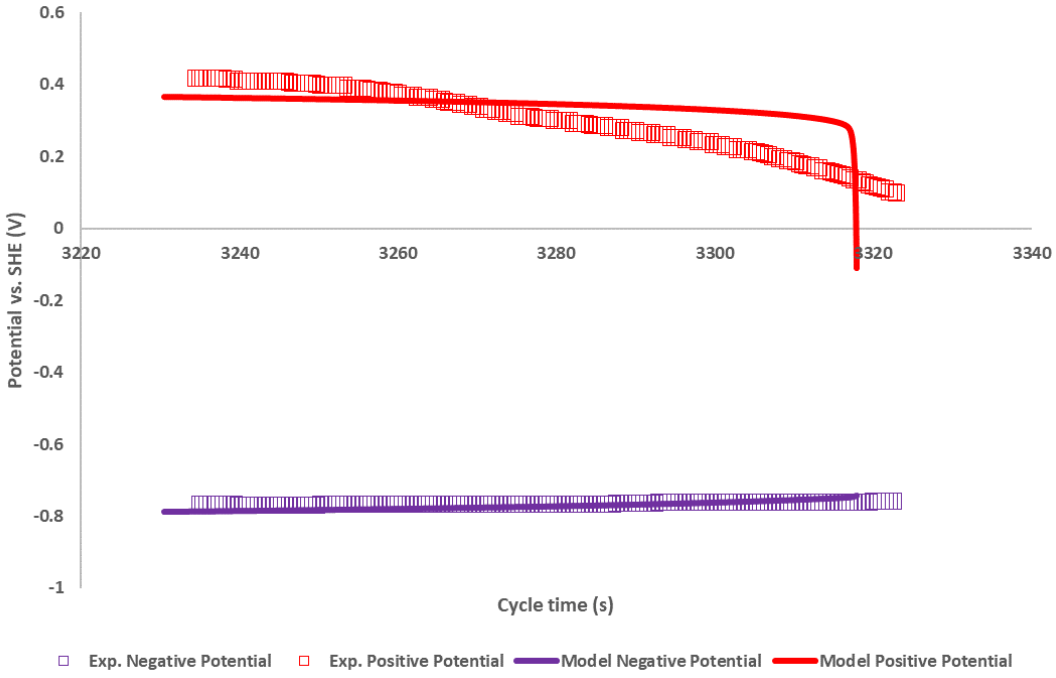

Figure 6.16: Model-computed half-cell electrode potentials and experimental electrode potentials measured by Gong et al.[17] at end of discharge.

Comparison of the curves shows reasonably good agreement between the model and experimental data at the end of discharge. The negative electrode potential values predicted by the model follow the experimental values very closely. The model predicts a much more rapid drop in electrode potential at

the positive electrode than the experimental data show. This behaviour is discussed briefly in Chapter 4; it is likely caused by the fact that the model does not take into account reactant transport from the bulk electrolyte phase to the electrode surface. The Butler-Volmer equation used in the model formulation does not distinguish between electrolyte concentrations and surface concentrations throughout the porous electrode subdomains. This simplification exists due to the lack of reported mass transfer coefficients in literature for this system and the fact that fitting these parameters to the experimental data would likely be difficult. Furthermore, the polarization curve of the RFB system (Figure 5.3) is linear up to a current density of 400 mA/cm^2. This shows that the performance of the RFB is much more sensitive to ohmic internal resistance, most likely from its membrane, than it is to mass transport phenomena. Since the system uses a current density of 40 mA/cm^2 in normal operation, the effect of concentration overpotential is assumed to be insignificant for most of the cycle. This assumption is not likely to hold near the end of discharge when the concentrations of reactant species are very low. This limitation of the model results in the prediction of a more rapid potential drop at the limiting positive electrode than is observed empirically. In this system, mass transfer overpotential can play a role in decreasing the electrode potential due to reactant transport limitations near the end of discharge. This would result in an earlier but more gradual drop in the positive electrode potential than is predicted by the model, which can be seen from Figure 6.16. Although the model does not predict this behaviour perfectly near the end of discharge, the observed potential only departs significantly from the model-predicted values in the last minute of discharge; this deviation is not likely to be of major importance if the model is used in practical applications. It should also be noted that the discharge time of the model is a few seconds shorter than the empirical data. While this difference is noticeable given the small time scale of Figure 6.16, it represents a miniscule percentage of the overall cycle time and is well within the error tolerance specified for the model. The good agreement in the behaviour of Figure 6.16 represents

another important validation of the model, showing that the predictions of the model correspond well to empirical observations.

The concentration profiles of the major redox species are presented in Figures 6.17–6.24. Figures 6.17–6.20 depict the computed concentrations of Fe(III)-TEOA and Fe(II)-CN at two points during charge and two points during discharge over the course of the single-cycle run. Similarly, Figures 6.21–6.24 show the concentrations of Fe(II)-TEOA and Fe(III)-CN at various times over the same run. Perhaps the most noteworthy aspect of these concentration profiles is that the concentrations of each of the redox species in the flow battery varies by less than 5 mol/m^3 (0.005 mol/L) within each electrode during normal operation of the flow battery. For much of the duration of charge and discharge of the RFB, the concentrations of these redox species vary by less than 2 mol/m^3. This can be attributed to both the small electrode sizes and the high rate of electrolyte recirculation relative to the size of the electrode. The concentration profiles further show that redox species concentrations vary most in close vicinity of the membrane boundary, reflecting that the system is limited more by solute transport through the membrane than solute transport within the electrodes and electrode kinetics. Conversely, the concentrations of the redox species in the portion of the electrolyte furthest away from the membrane vary little in both the vertical direction along which the electrolyte flows and the horizontal direction for the majority of the cycle duration. Figures 6.17–6.24 show that the region in which the redox species concentration varies most significantly spreads out vertically and horizontally within the electrode subdomains as the battery nears the end of discharge. This is similar to the behaviour noted above with respect to electrode potential profiles at the end of discharge. Figures 6.25 and 6.26 depict the corresponding volume-based electronic current generation due to the redox reactions within the two electrodes at similar points near the middle of charge (800 s) and discharge (2400 s). It is evident from these figures that the Fe(II)-TEOA/Fe(III)-TEOA reaction occurs at a uniform rate within the positive electrode and the Fe(II)-CN/Fe(III)-CN reaction occurs at a relatively uniform rate within the negative

electrode, except over narrow portions closest to the membrane where the electronic current drops. This is the expected behaviour according to porous electrode theory for composite electrodes consisting of a mixed electronic/ionic conductor. The contribution of the electronic current to the total current increases from zero at the membrane/electrode interface to 100% at the electrode/current collector interface, as described in eqs (4.26) and (4.27). In general, this would lead to high ionic current density close to the membrane that is either conducted through the electrolyte or converted to electronic current that drives the redox reactions. Based on the results obtained from the model showing that the region where ionic current is dominant is confined to narrow regions next to the membrane, it appears that most of the ionic current is rapidly converted to electronic current via redox reaction rather than being conducted through the electrolyte. This observation is also reflected in the plots showing the spatial distribution of the ionic current density magnitude during charge and discharge in Figures 6.27 and 6.28, respectively. Such behaviour is not unexpected given the facile kinetics of both electrode reactions. It also indicates that ionic transport through the electrolyte is slow relative to electronic transport through the solid electrode phases and electrode kinetics in this RFB.

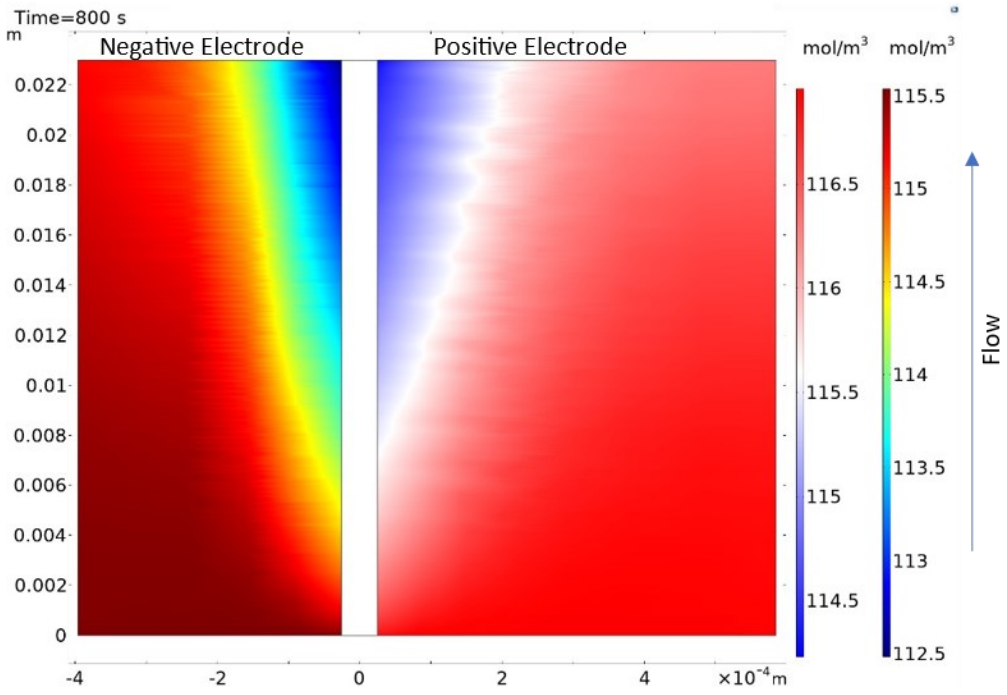

Figure 6.17: Fe(III)-TEOA (left) and Fe(II)-CN (right) concentrations at 800 s elapsed. The left and right legends correspond to the positive and negative electrodes, respectively.

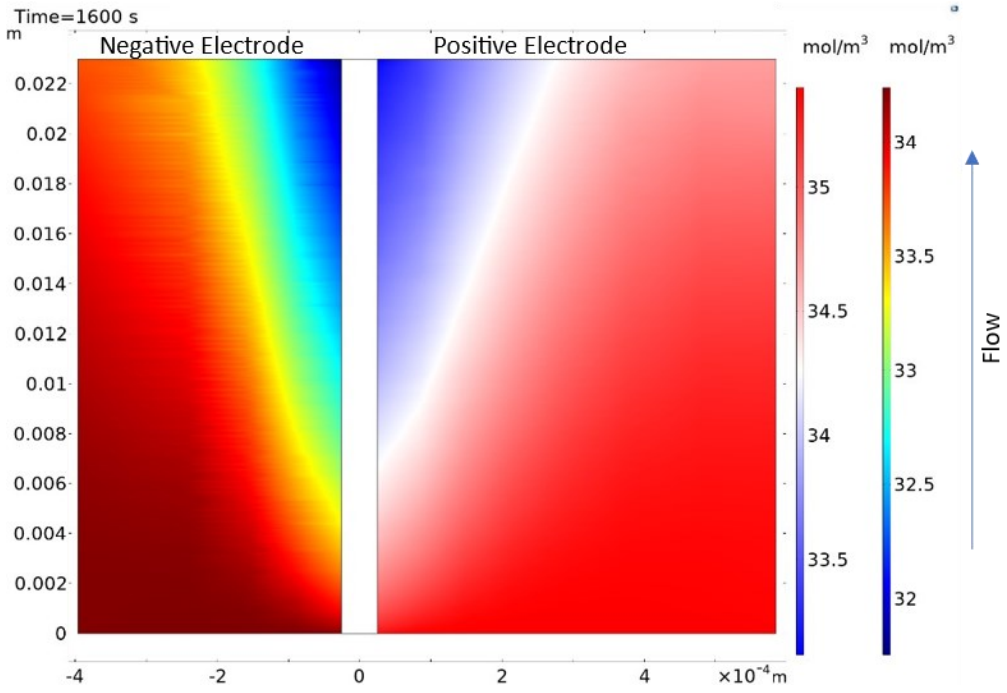

Figure 6.18: Fe(III)-TEOA (left) and Fe(II)-CN (right) concentrations at 1600 s elapsed. The left and right legends correspond to the positive and negative electrodes, respectively.

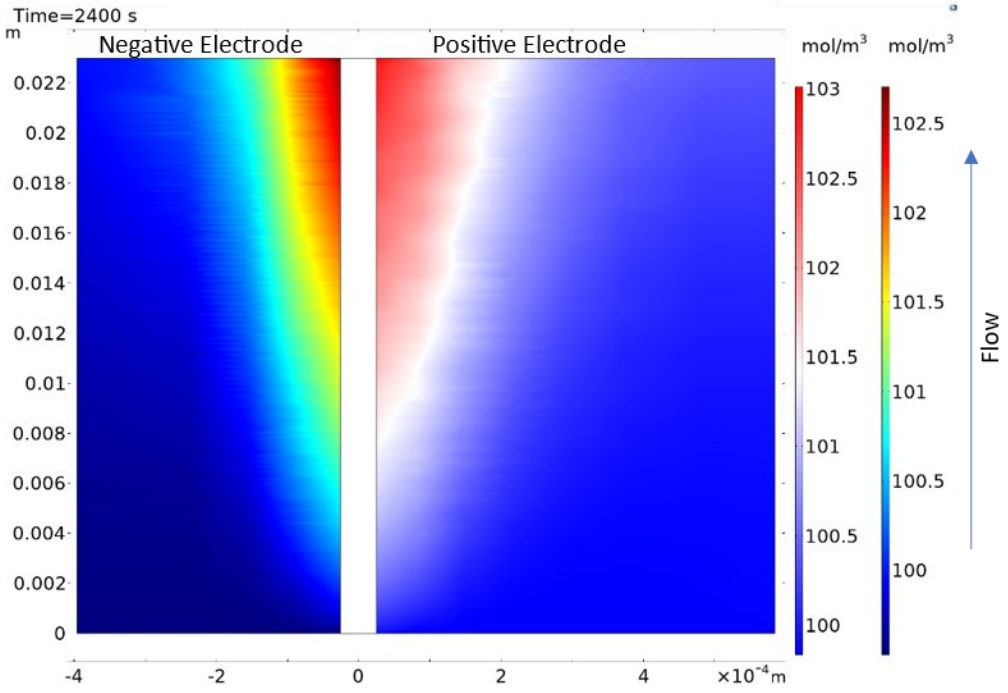

Figure 6.19: Fe(III)-TEOA (left) and Fe(II)-CN (right) concentrations at 2400 s elapsed. The left and right legends correspond to the positive and negative electrodes, respectively.

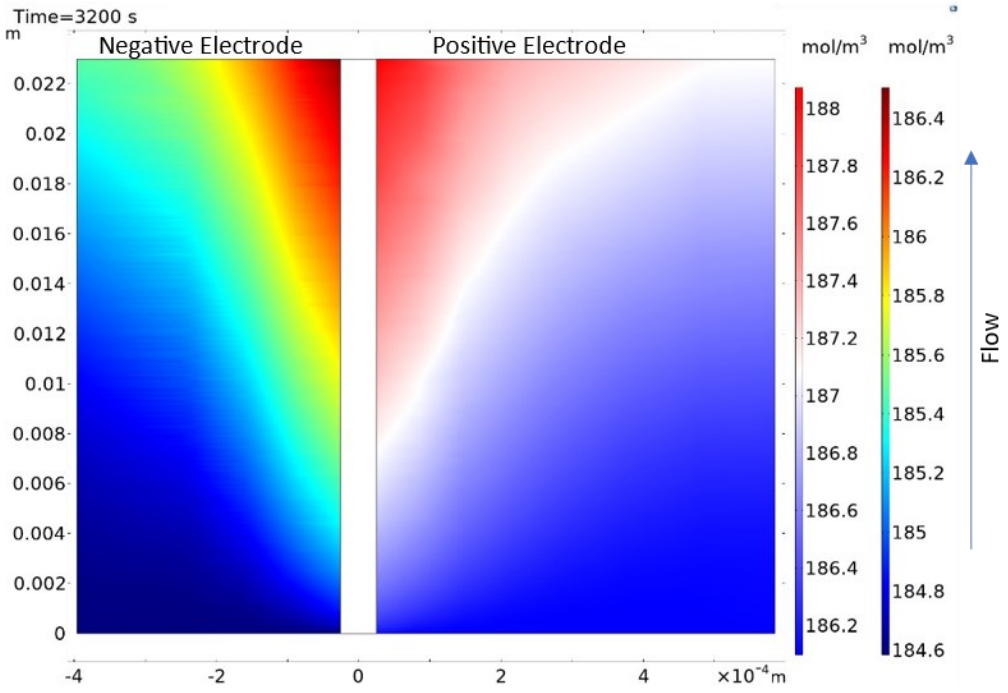

Figure 6.20: Fe(III)-TEOA (left) and Fe(II)-CN (right) concentrations at 3200 s elapsed. The left and right legends correspond to the positive and negative electrodes, respectively.

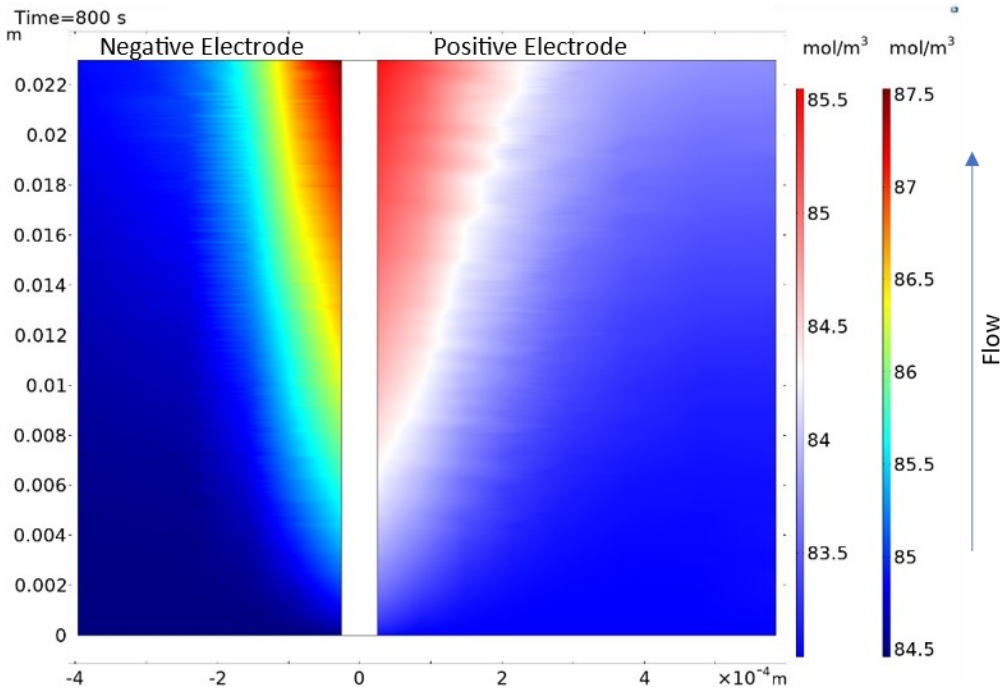

Figure 6.21: Fe(II)-TEOA (left) and Fe(III)-CN (right) concentrations at 800 s elapsed. The left and right legends correspond to the positive and negative electrodes, respectively.

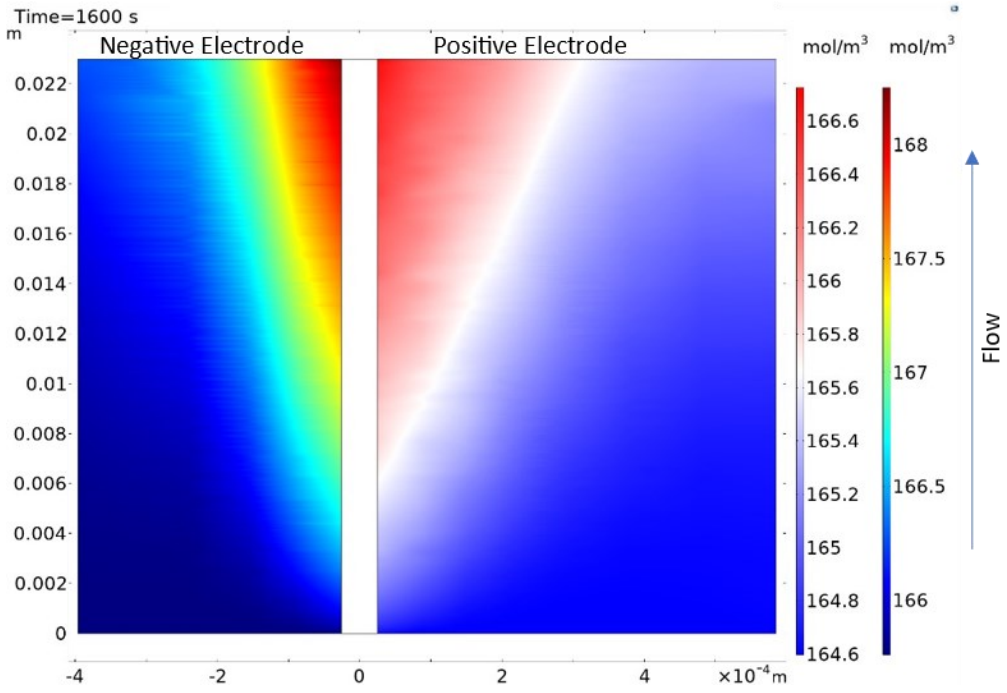

Figure 6.22: Fe(II)-TEOA (left) and Fe(III)-CN (right) concentrations at 1600 s elapsed. The left and right legends correspond to the positive and negative electrodes, respectively.

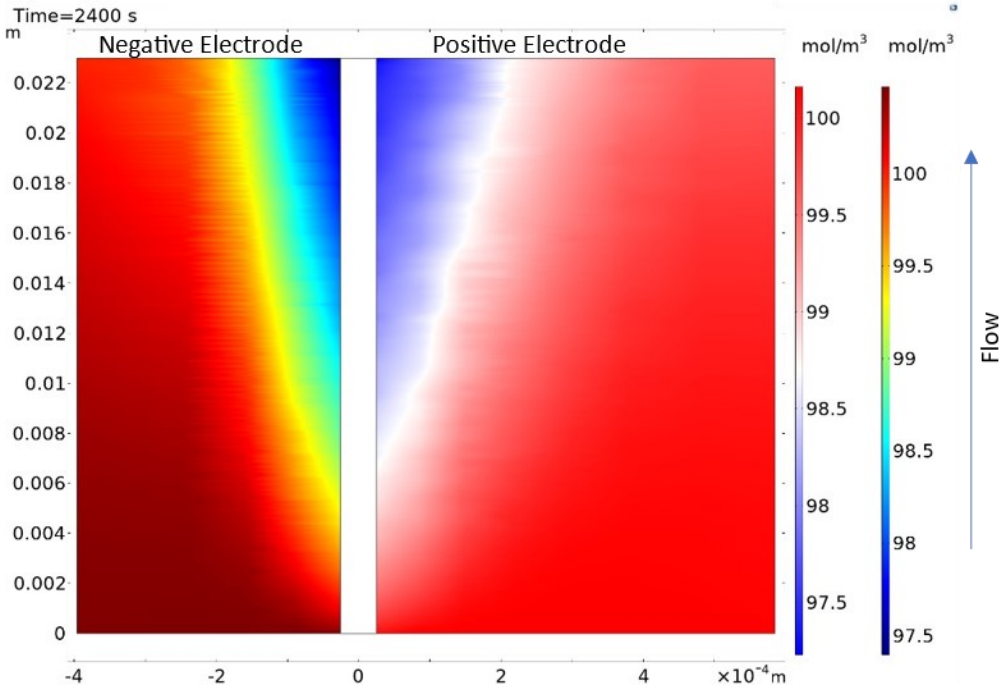

Figure 6.23: Fe(II)-TEOA (left) and Fe(III)-CN (right) concentrations at 2400 s elapsed. The left and right legends correspond to the positive and negative electrodes, respectively.

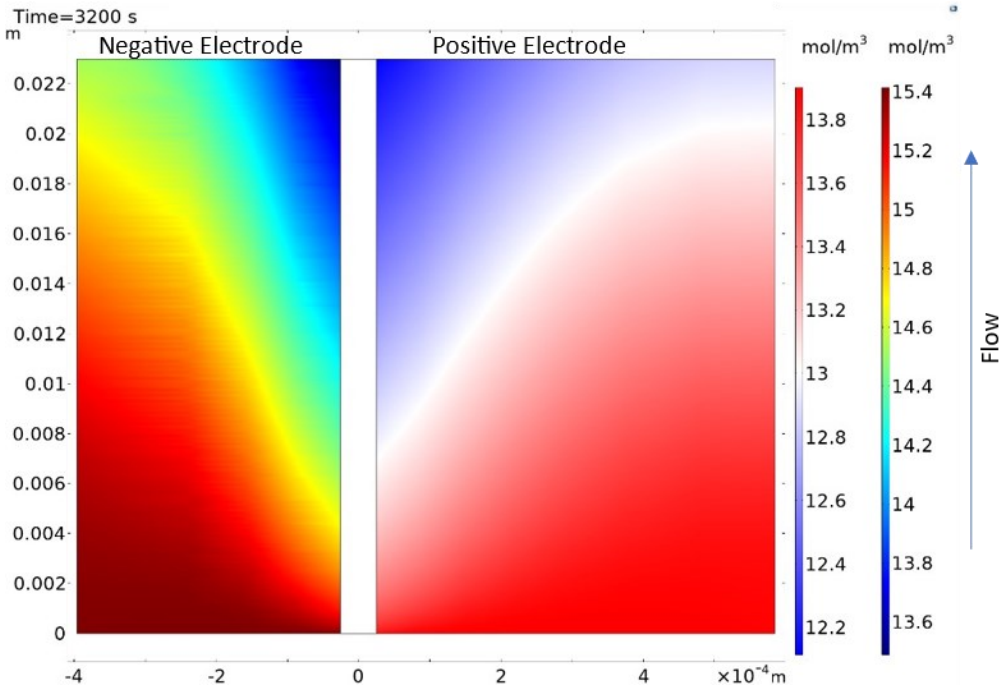

Figure 6.24: Fe(II)-TEOA (left) and Fe(III)-CN (right) concentrations at 3200 s elapsed. The left and right legends correspond to the positive and negative electrodes, respectively.

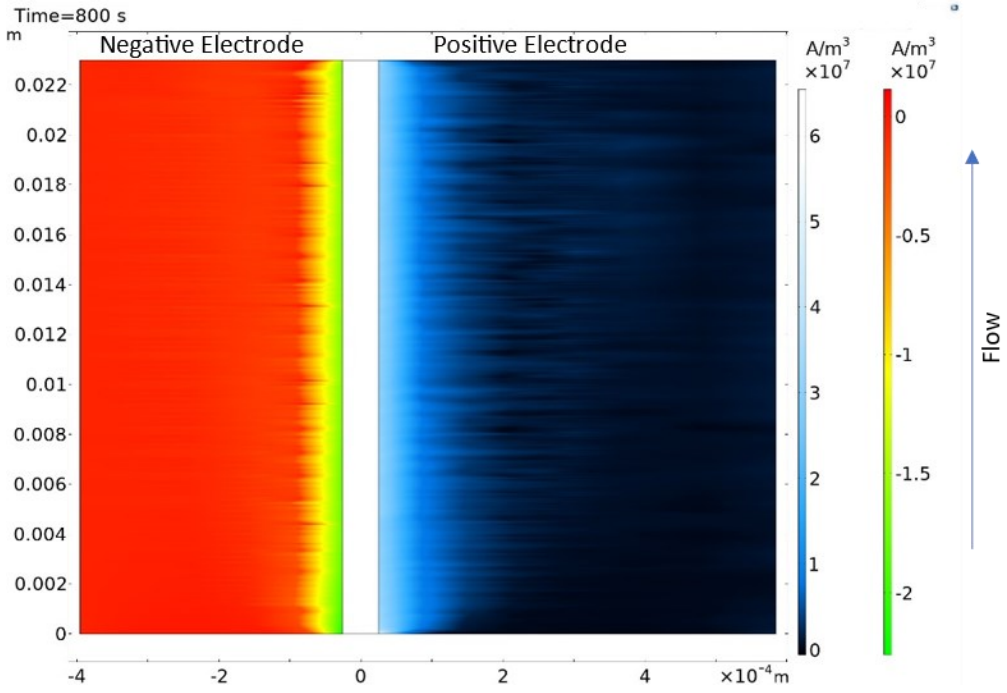

Figure 6.25: Volumetric current generation due to redox reactions at 800 s elapsed. The left and right legends correspond to the positive and negative electrodes, respectively.

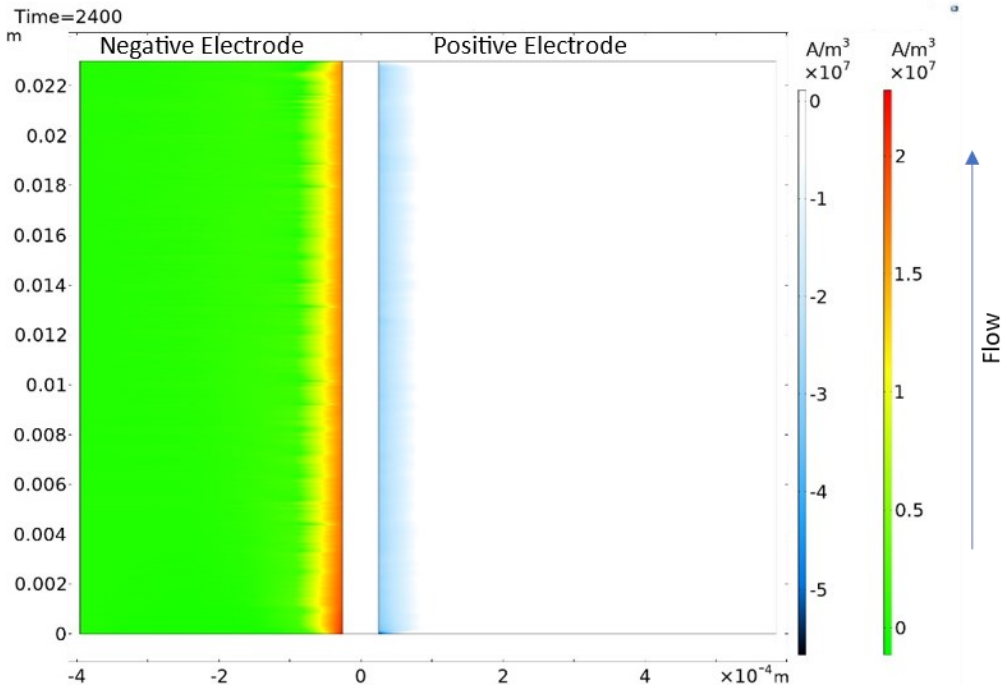

Figure 6.26: Volumetric current generation due to redox reactions at 2400 s elapsed. The left and right legends correspond to the positive and negative electrodes, respectively.

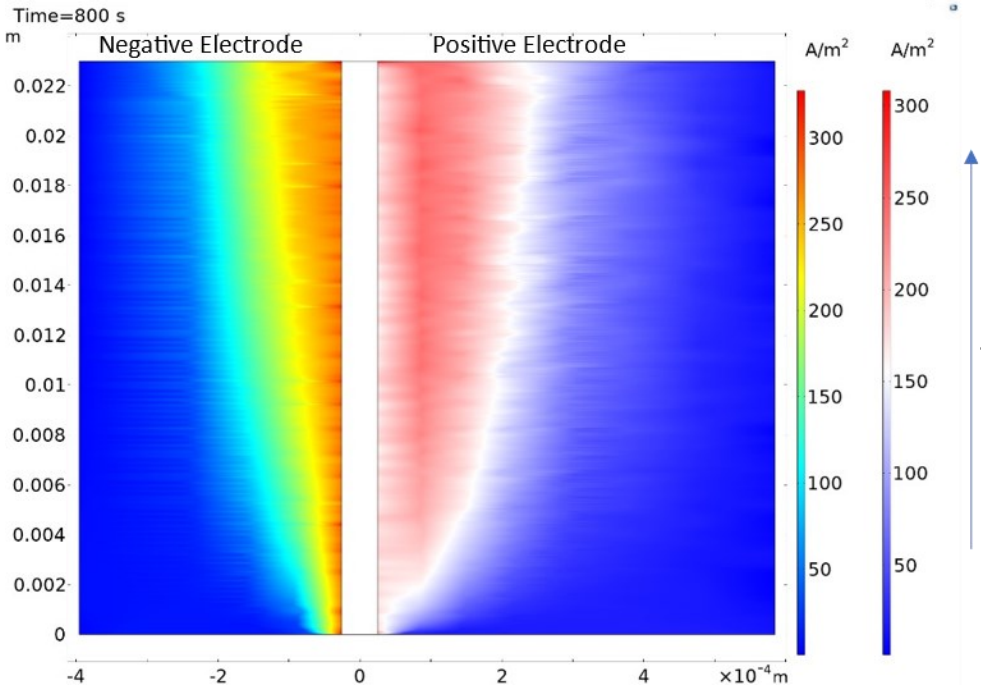

Figure 6.27: Electrolyte ionic current density magnitude at 800 s elapsed. The left and right legends correspond to the negative and positive electrodes, respectively.

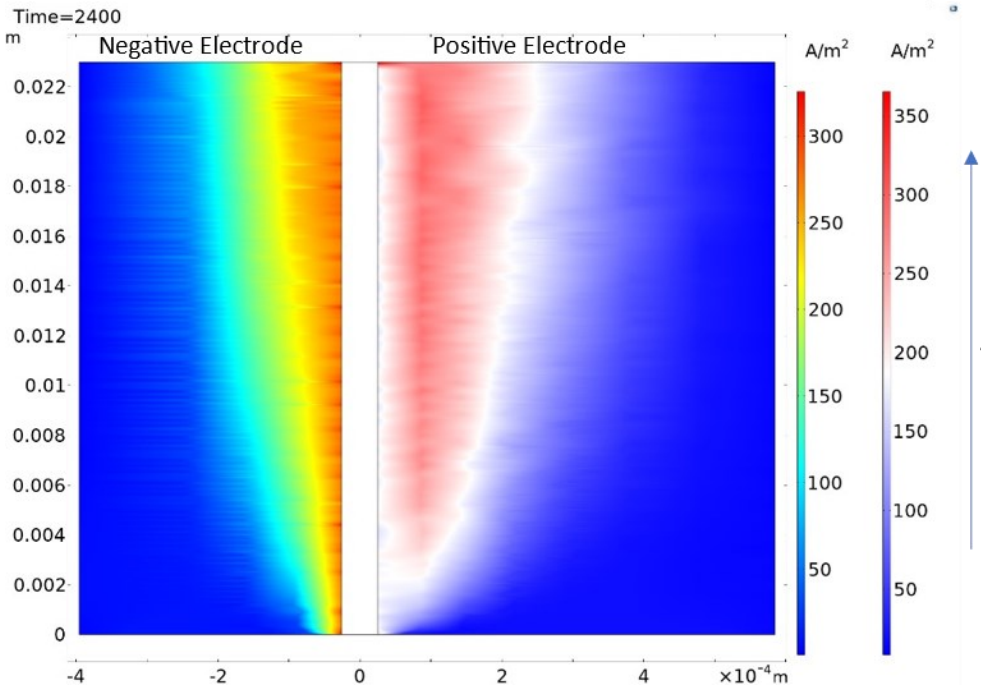

Figure 6.28: Electrolyte ionic current density magnitude at 2400 s elapsed. The left and right legends correspond to the negative and positive electrodes, respectively.

6.2 Multiple-Cycle Run

To validate the model, its behaviour must also be compared to the experimental data obtained by Gong et al.[17] for the multi-cycle run. The variation in the volumetric capacity and current efficiency over the multi-cycle run reported in the experimental study of Gong et al.[17] and computed by the model are compared below in Figure 6.29. It should be noted that volumetric capacity in this figure is based on the electrolyte volume for one side (half the total electrolyte volume) because this is the basis for the reported experimental capacity values. The model is used to simulate 180,000 seconds of operation, which amounts to 69 complete cycles. This simulation is used to fit only the hydrogen evolution reaction kinetics based on its behaviour, as discussed previously. The remaining parameters are determined from the single-cycle experiment and are used in this simulation to evaluate the robustness of their fit. Due to the long solution time of the model, it is not feasible to carry out simulations for the entire 110 cycles for which experimental data are available.

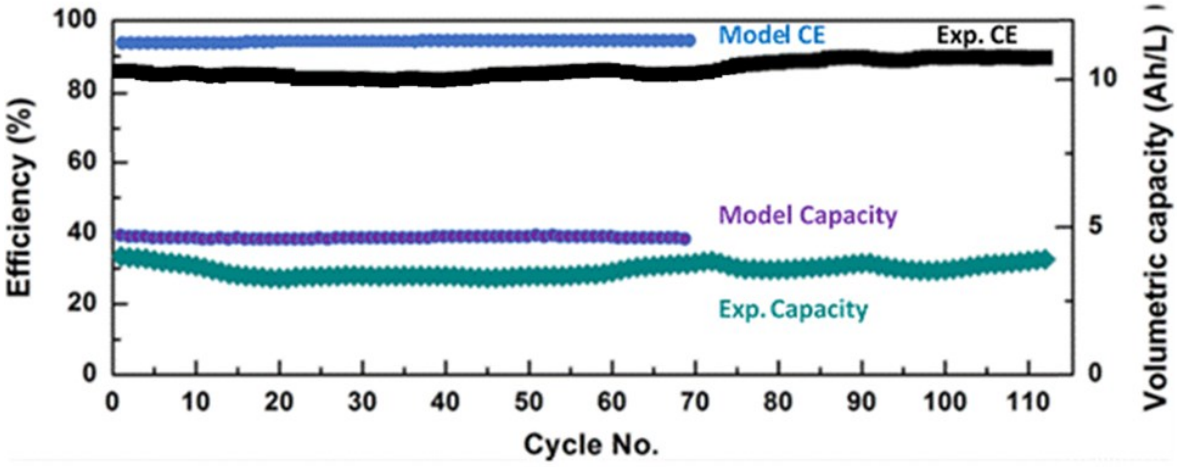

Figure 6.29: Current efficiency and volumetric capacity from multi-cycle simulation. Adapted from Gong et al.[17]

An observation that can be made from the experimental data is that the current efficiency of the RFB remains very stable over the first 70 cycles, before increasing gradually and slightly over the next 20 cycles and stabilizing thereafter at a higher level. From the available data, it is difficult to draw conclusions on the reason for this change in current efficiency. One possible explanation for the increase in current efficiency over time is the decline in TEOA permeation rate across the membrane due to its depletion in the negative electrolyte. This would increase the current efficiency at the positive electrode and potentially change which electrode reaction becomes limiting with respect to the RFB, as explained later in this chapter. While TEOA is initially present in great excess at the negative electrode, this raises potential questions about the capability of the RFB to sustain long-term cycling since TEOA depletion on the negative side should eventually result in iron precipitation as the TEOA concentration reaches a point where the Fe-TEOA complex becomes unstable. This effect has not been observed in the 110 experimental cycles but may occur in further cycling. Gong et al.[17] additionally state that the trend in current efficiency can be explained if the crossover of TEOA is highest at the start of cycling. Due to the computational limitations noted above, it is not potential to extend the simulations to cover the portion of the run where the small rise in current efficiency is observed. It should be acknowledged that it is unclear whether the model would have predicted this increase in current efficiency; it does take into account the decline in TEOA permeation due to depletion in the negative electrolyte but does not account for any other phenomena that may be responsible for this behaviour. The evolution of the current efficiency generated by the model over the first 69 charge-discharge cycles is shown in Figure 6.29. The behaviour of the model over the simulation duration is qualitatively consistent with that of the experimental results in that the current efficiency remains stable throughout the run. It should be noted, however, that the computed current efficiencies are ~ 8% higher than those observed during the experiments. Errors with the model are not the likely cause of this discrepancy. Instead, the problem appears to be related to inconsistencies in the experimental data reported by Gong et al.[17] The

parameters in the model that primarily affect the CE are fit based on the experimental data collected for the single-cycle run alone. Comparison of the data reported by Gong et al.[17] from their single-cycle experiment to that of their multi-cycle experiment reveals that the current efficiency during the first cycle of the multi-cycle run is ~ 8% lower than the value during the single-cycle experiment. Further testing is warranted to reconcile this discrepancy between the single-cycle and multi-cycle data. With the available information, the behaviour of the model appears to follow the behaviour observed for the multi-cycle testing, providing evidence of the model adequacy.

Another observation that can be made from the experimental data of Figure 6.29 is that the volumetric capacity of the RFB remains fairly stable, oscillating gently over the course of the multi-cycle run. It is not clear whether the relatively minor variation of RFB capacity over many runs can be attributed to experimental conditions or transient phenomena occurring in the system that are beyond the scope of this model. The fact that no persistent capacity loss observed over the course of many cycles of this RFB is significant in validating the present model. It should be noted that the model-predicted capacity values are higher than those observed experimentally. This is likely due to the discrepancy noted earlier between the single-cycle and multiple-cycle current efficiencies. As discussed in prior sections, the absence of any capacity fade in this RFB has been crucial in determining the phenomena that are likely taking place in this system. The evolution of the model-predicted volumetric capacity of the RFB over the multi-cycle run is presented in Figure 6.29. As shown, the capacity of the RFB remains stable over many runs, with no significant capacity fade. This validates the long-term behaviour with respect to RFB capacity predicted by the model.

An important observation during the simulation of the multi-cycle run is the change in limiting reactant that occurs over the course of many cycles. In the case of single-cycle operation, the experimental (and fitted model) measurements of the individual electrode potentials during discharge (Figure 6.15) reveal

that the reduction of ferricyanide to ferrocyanide at the positive electrode is the limiting reaction. However, Gong et al.[17] did not report measurements of the individual electrode potentials during the multi-cycle experiment. Consequently, it is not known from their study whether the positive electrode reaction continues to be limiting during the entirety of the multi-cycle operation. To use the model to investigate this question, we plot the difference between the inlet concentrations of Fe(III)-CN and Fe(II)-TEOA over the course of the run in Figure 6.30. This difference in concentrations is used because both species should remain at similar concentrations if the system remains balanced. The only iron-containing species at the negative electrode are Fe(II)-TEOA and Fe(III)-TEOA and the only iron-containing species at the positive electrode are Fe(II)-CN and Fe(III)-CN. These iron-containing species can only be converted between one another through redox reactions and the total iron concentration at each electrode is 200 mol/m^3 (0.2 M). In a battery where no side reactions take place and the redox species concentrations remain perfectly balanced, the difference in Fe(III)-CN and Fe(II)-TEOA will remain zero throughout. The nonzero values of this difference during cycling of the present system (Figure 6.30) therefore indicate the direction and magnitude of imbalance that develops between these reactants. The apparent oscillations in this value are likely due to the differing rates of the side reactions at the two electrodes during charge and discharge.

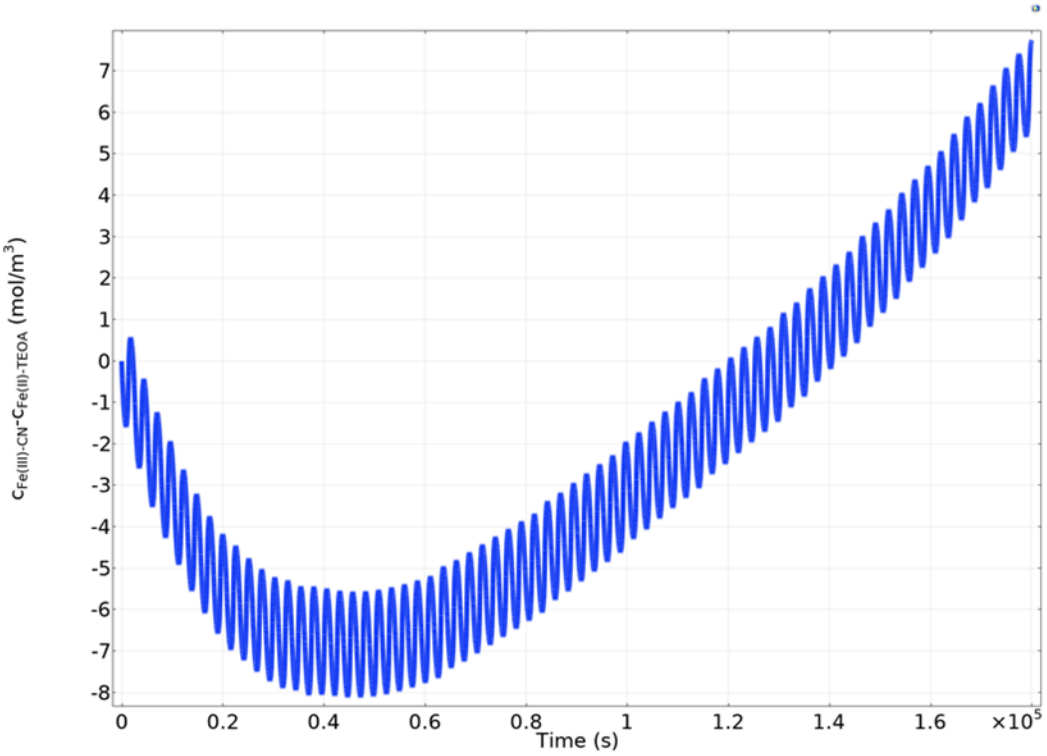

Figure 6.30: Difference between Fe(III)-CN and Fe(II)-TEOA inlet concentrations in multi-cycle simulation.

As discussed in earlier sections, continued imbalance between these two reactant concentrations is expected to result in persistent capacity fade. Initially, a relatively small difference in concentration exists between the two reactants, with Fe(III)-CN being depleted faster than Fe(II)-TEOA, as expected. This difference grows as the RFB operation continues for ~ 20 cycles, with the concentration of Fe(III)-CN consistently being lower than that of Fe(II)-TEOA. This implies that the negative electrode reaction is limiting during charge over this portion of the cycling, while the positive electrode reaction is limiting during discharge. During charge, Fe(II)-TEOA and Fe(III)-CN are products; if the Fe(III)-CN concentration is lower than that of Fe(II)-TEOA then the latter product will have its corresponding reactant (Fe(III)-TEOA) depleted first, limiting charge at the negative electrode. During discharge, these two species are reactants and Fe(III)-CN serves as a limiting reactant during discharge at the positive electrode. The difference between the two reactants grows until it reaches a maximum after ~ 20 cycles. However, thereafter the trend begins to reverse and the difference in concentrations now shrinks. Eventually,

after ~ 56 total cycles, the difference changes sign so that the concentration of Fe(III)-CN now becomes greater than that of Fe(II)-TEOA. This trend continues over the remaining cycles, with the difference becoming progressively larger. This suggests that after some cycling the iron-cyanide reaction becomes limiting during charge, while the iron-triethanolamine reaction becomes limiting during discharge. This is a reversal of the initial behaviour, as well as the behaviour observed during the single-cycle run. This behaviour is further reflected in the computed individual electrode potentials in Figure 6.31 that demonstrate deeper discharge of the positive electrode relative to the negative electrode in the early stages and deeper discharge of the negative electrode relative to the positive electrode in the later stages.

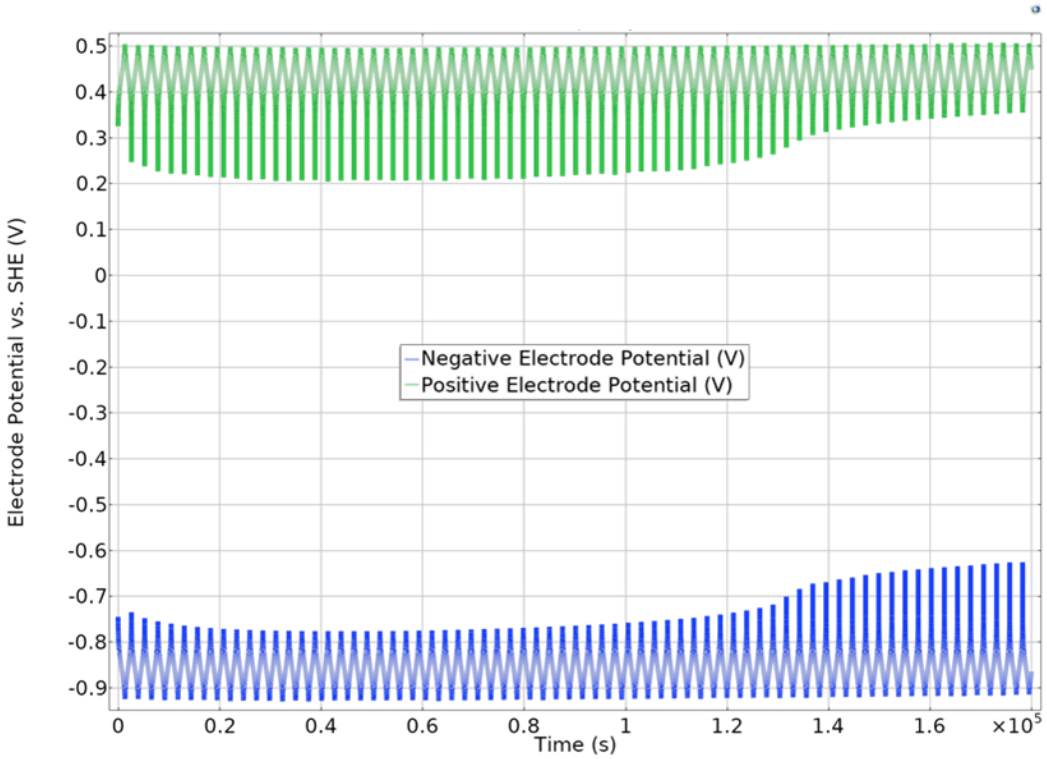

Figure 6.31: Electrode potentials from multi-cycle simulation.

Analysis of the model shows that this behaviour is caused by the continual permeation of TEOA through the membrane from the negative side to the positive side. As the concentration of free TEOA in the negative electrode decreases, its rate of transport across the membrane decreases proportionally. The

permeation flux of TEOA through the membrane over the multiple-cycle simulation is presented in Figure 6.32. It can be seen that by the end of the simulation, the flux and thus rate of TEOA permeation drops ~ 20% from its initial value.

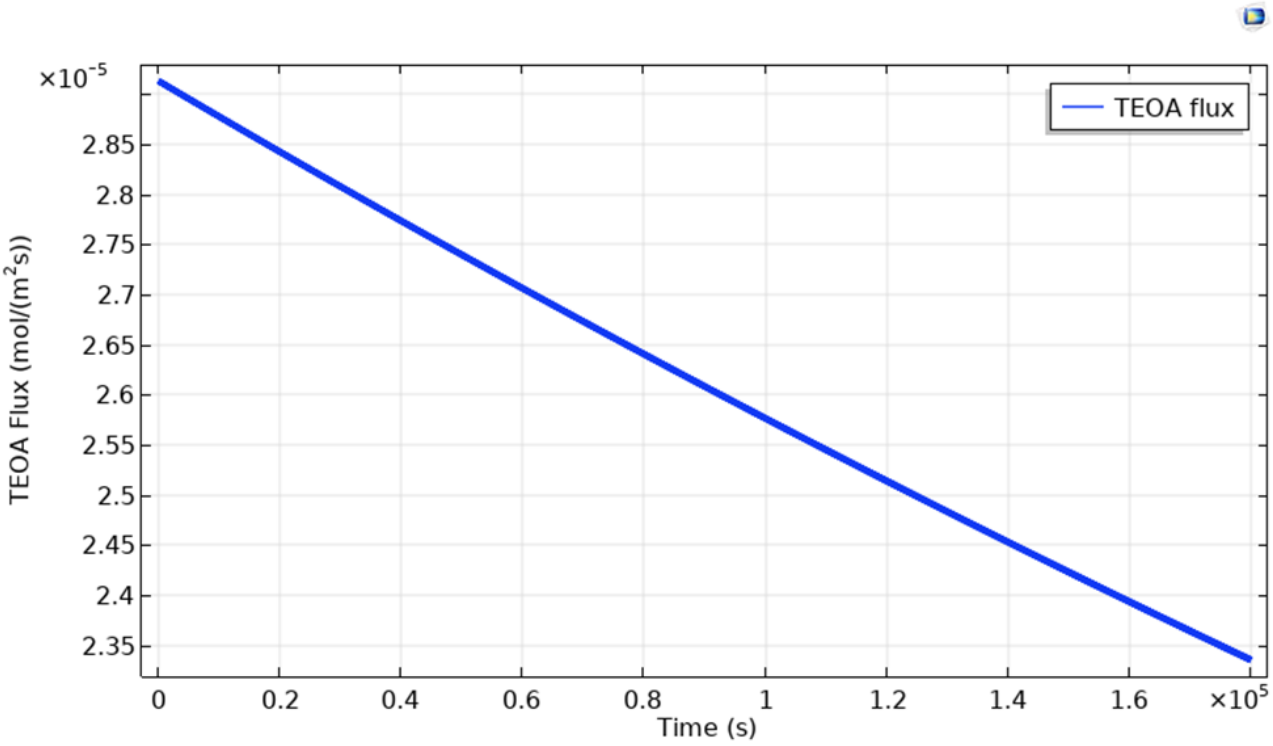

Figure 6.32: Flux of TEOA through membrane over multiple-cycle simulation.

With less free TEOA crossing over to the positive electrode, the current efficiency of the positive redox couple increases. This increased current efficiency would presumably lead to the iron-cyanide reaction becoming limiting during charge, as more of the applied current would drive the conversion of Fe(II)-CN to Fe(III)-CN, while the current efficiency of the negative electrode reaction would remain relatively unchanged. For the same reason, it would be expected that the iron-triethanolamine reaction would become limiting during discharge since a greater fraction of the cathodic current from the Fe-CN reaction would be balanced with the anodic current of the Fe-TEOA redox couple with slower TEOA transport and oxidation. This is because TEOA oxidation competes with Fe-TEOA oxidation for the

cathodic current of the Fe-CN redox couple during discharge. This explanation is consistent with Figure 6.33, which plots the concentrations of Fe(III)-CN, Fe(II)-TEOA, and free TEOA over time.

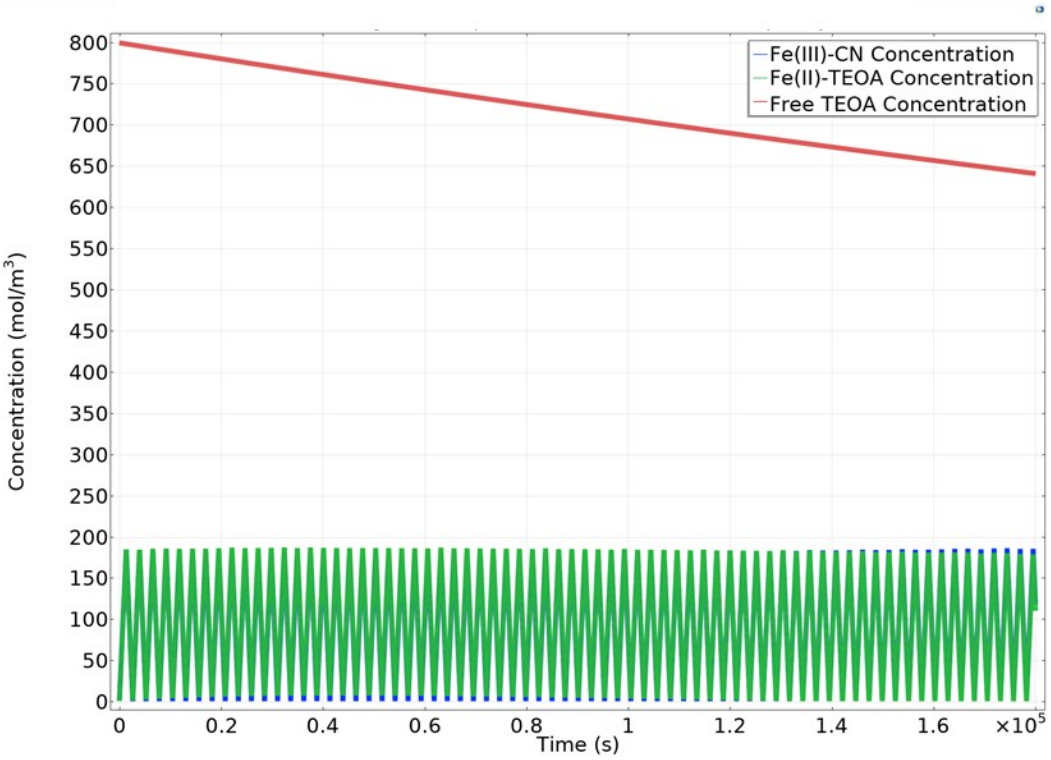

Figure 6.33: Concentrations of Fe(III)-CN, Fe(II)-TEOA, and free TEOA in multi-cycle simulation.

6.3 Model Convergence

The convergence of the transient solver is found to follow a consistent pattern during the solution of the model. The convergence plot obtained during the single-cycle simulation is shown in Figure 6.34. This plot provides a visual representation of the change in time-step size as the solver proceeds through the simulation. It should be noted that Figure 6.34 shows a plot of reciprocal step size over the course of the simulated charge-discharge cycle. A decrease in reciprocal step size indicates improvement in model convergence, allowing the transient solver to take larger time steps. An increase in reciprocal step size indicates that convergence is becoming more difficult, requiring the solver to take smaller steps in time.

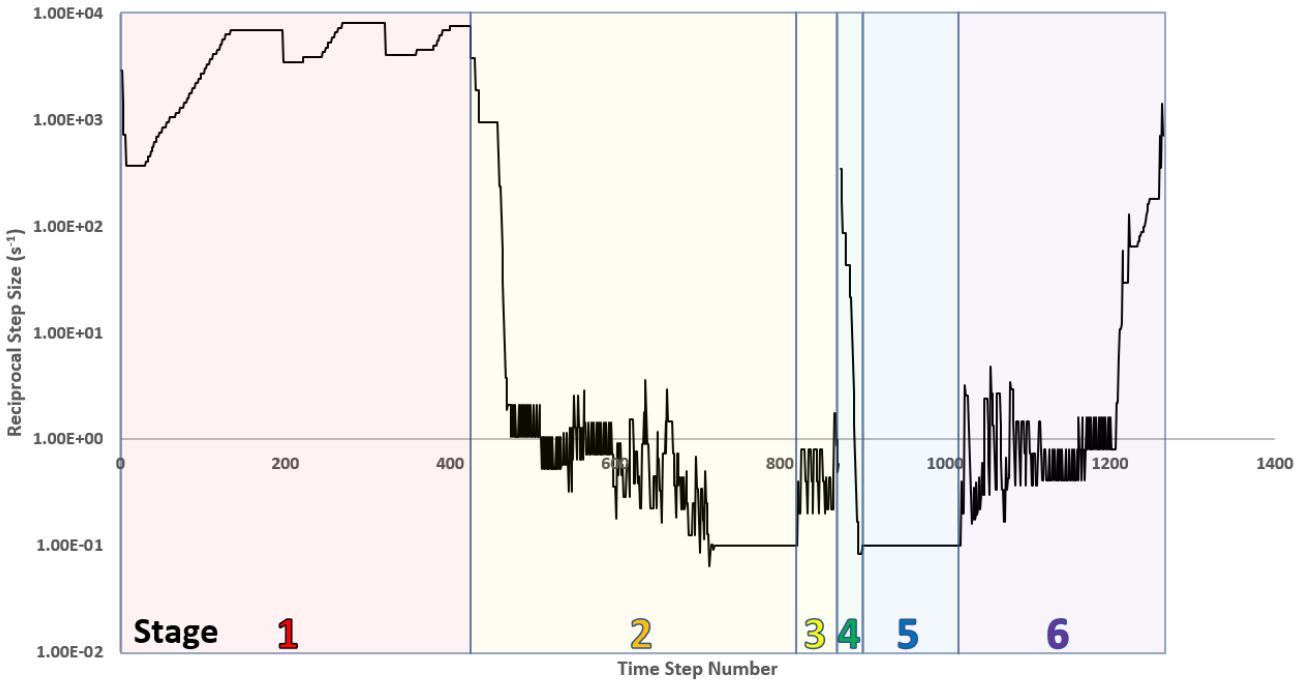

Figure 6.34: Single-cycle model convergence.

Figure 6.34 shows the typical pattern observed for the behaviour of the solver over the course of single-cycle simulations. In the first stage, the solver initializes the model and requires very small time steps in order to converge. This stage persists over a relatively large number of steps before reaching the point at which the solution stabilizes. Once the solution has stabilized following initialization, the second stage begins where charge occurs. During this stage, the model takes increasingly large steps in time as it becomes easier to meet the convergence criterion. The step size increases until it reaches 10 seconds, which is the user-specified maximum step size. The solver then continues with this step size until the system nears the end of charge after ~ 820 total time steps. Once the RFB is charged to a large enough extent, the RFB voltage begins to rise at a faster rate with charge. This leads to the third stage of the solution where the solver requires smaller time steps to converge. Eventually, the third stage ends after ~ 870 total time steps when the 1.6 V threshold voltage for the termination of charge is reached by the RFB. The fourth stage begins with reinitialization of the model, with the direction of current reversed,

indicating the switch from charge to discharge. The solver converges rapidly during this stage; this is likely due to the fact that the reactants of each redox couple are less depleted at the end of charge than at the start of charge. As shown in Figure 6.35, the Fe(II)-CN and Fe(III)-CN concentrations at the end of charge are closer to one another than at the start of charge. The same trend is observed in the case of Fe(II)-TEOA and Fe(III)-TEOA on the negative side. The fact that none of the species is depleted at the end of charge to the same degree that some species are at the end of discharge may result in greater stability during the transition from charge to discharge, relative to the transition from the subsequent discharge to charge. The fifth stage begins when the solver reaches the aforementioned maximum time step of 10 seconds at ~ 900 total time steps; it is during this stage that most of the discharge process occurs. Eventually, as the RFB discharges to a great enough extent, the voltage begins to drop at an increasing rate. This marks the beginning of the sixth and final stage, where the solver is again forced to take smaller steps in time to achieve convergence as a result of a rapidly changing solution. As the voltage continues to drop and reactants become more depleted, the time steps taken by the solver decrease. The time step size continues to shrink until the battery voltage reaches the discharge threshold, at which time the simulation ends.

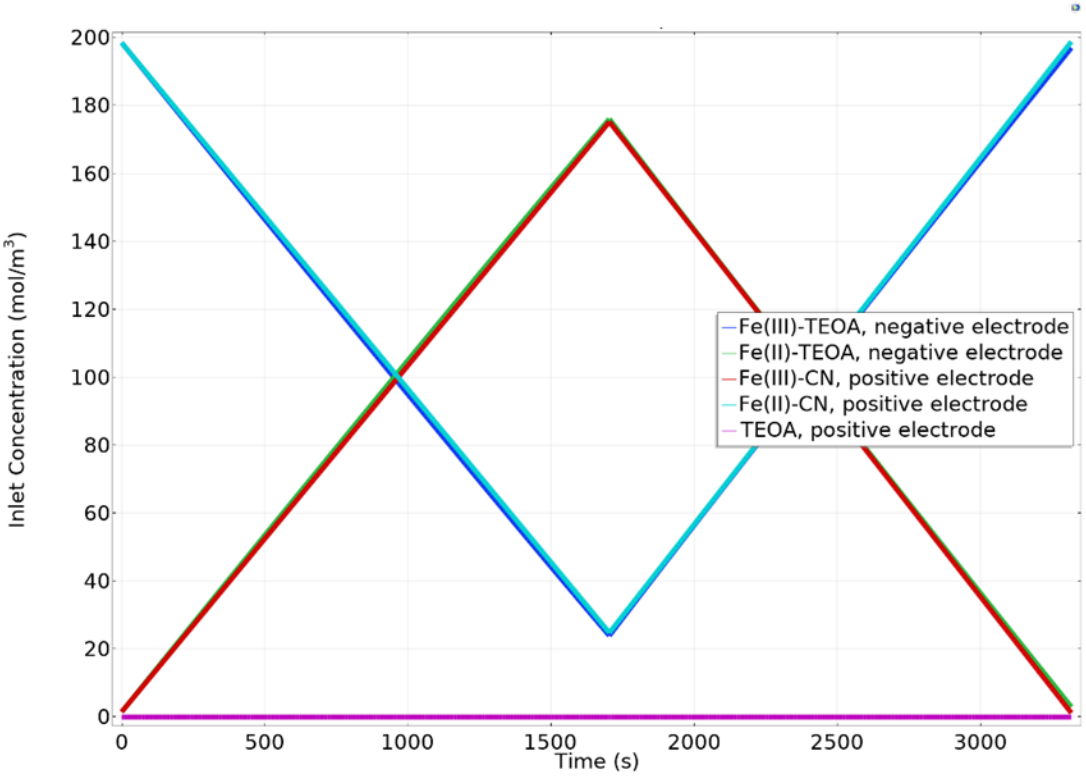

Figure 6.35: Inlet concentrations of redox species in single-cycle model.

The convergence of the multi-cycle simulation is illustrated in Figure 6.36. The behaviour of each individual cycle in this simulation follows the same trend as the single-cycle simulation, although this trend is not easily visible in Figure 6.36. Convergence of the multi-cycle simulation is also significantly faster due to the relaxed error tolerance of 0.01, which is four times the 0.0025 error tolerance used during the single-cycle simulation. Figure 6.36 illustrates how the convergence of the solver changes over the course of many cycles. It can be seen that over the first 75% of the time steps during the simulation, the model convergence is very stable so that the step size never decreases below a few thousandths of a second. However, over the final 25% of the simulation, the smallest step size required by the solver decreases progressively to much lower values and eventually reaches values as small as 0.0001 seconds (triggering the implicit event described in Chapter 4). This indicates that as time progresses, the simulation becomes less stable, resulting in more difficult convergence. It is difficult to speculate on the cause for the decrease in model stability over long periods of cycling due to the model

complexity and nonlinearity of its equations. A possible contributor to this decreasing stability is the decrease in TEOA permeation over time, as discussed earlier in the chapter. This drop in permeation is the most persistent change to the system that grows in significance over time. Lower TEOA permeation could reasonably be expected to reduce the TEOA concentration in the positive electrolyte to even smaller values than normal. Computation of the kinetics for the TEOA oxidation reaction at the positive electrode is performed with this positive-side TEOA concentration as an input. This may present a source of instability for the solver as the concentration of TEOA in the positive electrolyte reaches very small values. Due to the high-order implicit backward differentiation formula methods used by the solver, it is difficult to definitively diagnose the source of the decrease in stability.

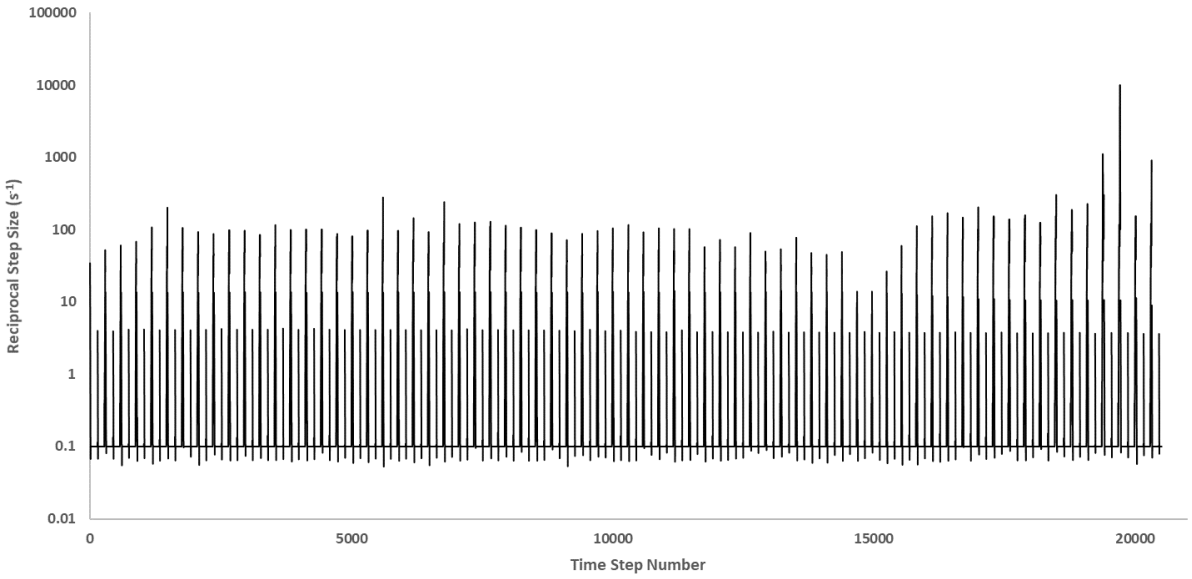

Figure 6.36: Convergence of multi-cycle simulation.

7 Conclusions and Recommendations

7.1 Conclusions

A transient two-dimensional model for the all-iron all-soluble aqueous redox flow battery introduced by Gong et al.[17] has been developed in the present work as the first model for this system. This flow battery uses the Fe(II)-TEOA/Fe(III)-TEOA redox couple at the negative electrode and the ferricyanide/ferrocyanide redox couple at the positive electrode. These negatively charged iron complexes are stabilized by operating the system at a high pH. Both redox couples have facile kinetics. During charge, Fe(III)-TEOA is reduced to Fe(II)-TEOA and ferrocyanide is oxidized to ferricyanide; these reactions are reversed during discharge. The model is solved using the finite element method in COMSOL Multiphysics and validated by comparison to the experimental data reported in the study of Gong et al.[17] The modelled battery consists of two porous electrode subdomains separated by an ion-exchange membrane subdomain.

The experimental data on which the model is based suggest that the main mechanism for current efficiency loss is the oxidation of free triethanolamine by ferricyanide in the positive electrolyte after it has permeated across the ion exchange membrane. The model prediction of a significant and persistent reactant imbalance between Fe(II)-TEOA and ferricyanide has led us to the conclusion that a small amount of hydrogen evolution also occurs at the negative electrode, something that was not considered by Gong et al.[17]

The inclusion of these processes within the model for the operating battery required us to formulate kinetic expressions for these reactions. Analysis of reaction rate data available in the literature shows that ferricyanide oxidizes triethanolamine rapidly in alkaline solutions. With the additional observation that the rate of triethanolamine oxidation observed in the present RFB system is dependent on

electrode potential, we have modelled the oxidation of triethanolamine as a single electrochemical step at the positive electrode. A cathodic Tafel relationship has been used to describe the rate of the hydrogen evolution reaction at the negative electrode.

The transport of charge carriers across the ion exchange membrane is also investigated. Due to the use of a cation exchange membrane in the redox flow battery under extremely alkaline conditions, a review of the literature has been conducted to determine the predominant charge carriers under these conditions. It is determined that hydroxide ions are most likely to be the prevailing charge carriers in the Nafion 212 membrane under these conditions. For the purposes of simplicity and numerical stability, the membrane has been modelled under the assumption of single-ion transport, with hydroxide being its sole charge carrier. For these same reasons, the membrane is modelled as a resistive element and a linear (ohmic) voltage-current relationship for the purposes of describing charge transfer is obtained.

Before carrying out the actual parameter estimation and model validation, we have performed a sensitivity analysis on parameters whose values are not confidently known to determine those among them that are most significant to the model fit and accuracy. Upon identification of these significant parameters (membrane conductivity σ_m, TEOA permeation coefficient P, and the ferricyanide/ferrocyanide reaction formal potential $E^{o\prime}_{\mathrm{pos}}$), these values are estimated by fitting the model to experimental cell voltage-time data obtained for a single charge-discharge cycle. The multiple-cycle simulation behaviour is also used to fit the hydrogen evolution exchange current density $i_{0,\mathrm{H_2}}$. Each of the fit parameters has a separate effect on the shape of the single-cycle charge-discharge curve or the multiple-cycle model behaviour, which greatly facilitated the process of fitting these parameter values. The membrane conductivity is found to primarily affect the voltage efficiency, which determines the difference between the charge voltage and discharge voltage in the galvanostatic charge-discharge curves. The permeation coefficient and electrochemical oxidation kinetics parameters (rate constant,

formal potential, and transfer coefficient) of free triethanolamine, which mainly affect the coulombic efficiency and the relative lengths of the charge and discharge times, are also fit based on the single-cycle charge and discharge voltage curves. The kinetic parameters for the hydrogen evolution reaction at the negative electrode, which affect the balance of reactants between the two primary electrode reactions, are further fit based on the behaviour observed experimentally in the multiple-cycle charge-discharge data. Additionally, the single-cycle charge and discharge curves are used to fit the formal potential of the iron-cyanide redox couple; this parameter affects both the charge and discharge potentials at the positive electrode, as well as the cell voltage.

Validation of the model is conducted by comparing the simulation of both a single charge-discharge cycle and a multiple-cycle run to experimental data obtained for the redox flow battery system by its original researchers. The single-cycle model output is used to evaluate the adequacy of the fit with respect to the experimental data used to fit it. The multiple-cycle model is used to simulate and validate the long-term cycling behaviour of the fit model with respect to the parameters fit from the single-cycle data and to evaluate the adequacy of the fit for the exchange current density of the hydrogen evolution reaction at the negative electrode. The fitted model for the single-cycle fits the experimental data reasonably well; the most significant deviation of the model from the experimental data occurs at the end of discharge, where the model predicts a steeper drop in cell voltage than that observed empirically. This discrepancy is most likely explained by factors such as pore-scale reactant transport phenomena that are beyond the scope of the present model.

The positive and negative electrode potential profiles are generated at several points in time over the course of the single-cycle simulation. These profiles show that the electrode potential does not vary significantly within each electrode for most of the cycle time; it is only toward the end of discharge that the variation in electrode potential within each electrode becomes significant. Comparison of the behaviour of the spatially-averaged electrode potentials at the end of discharge to the electrode

potentials observed experimentally shows good agreement. In both the experimental data and the simulation, the positive electrode is found to limit the cell voltage at the end of discharge. Reactant concentration profiles are also generated for the primary redox species across the positive and negative electrodes at several points in time over the course of the single-cycle simulation. The reactant depletion and product generation are found to be most significant in the regions close to the membrane-electrode boundary. It can thus be concluded that the model predicts that the rates of the primary redox reactions at each electrode are greatest in the vicinity of the membrane-electrode interface. No information is available in the literature that can be used to validate this prediction with respect to the present RFB system.

The model has been used to simulate a sequence of consecutive charge-discharge cycles in addition to the single-cycle simulation. Over nearly 70 cycles, the current efficiency and capacity of the redox flow battery remain nearly constant. Apart from some oscillatory variations in the experimental data, the model predictions agree well with the experimental observations; the current efficiency and capacity remain relatively constant over the same number of cycles. The model results suggest that the redox reaction limiting the discharge of the redox flow battery changes from the iron-cyanide reaction at the positive electrode to the iron-triethanolamine reaction at the negative electrode over the course of the multiple cycle run. This agrees with the expected behaviour of the redox flow battery due to the combined effects of the relatively constant rate of hydrogen evolution reaction at the negative electrode and the declining flux of free triethanolamine across the membrane over time. However, an inconsistency is noted between the experimental data reported by Gong et al.[17] for the single-cycle run and for multiple-cycle run – the current efficiency observed during most of the multiple-cycle run is significantly lower (~ 85-90%) than that observed during the single-cycle case (~ 93%).

Convergence of the model solution has been found to be a challenge during the simulations. The convergence follows a consistent trend; the solution is least stable at the start of each charge stage,

start of each discharge stage, and the end of each discharge stage. The stability of the convergence does not affect the model results but rather the step size for the transient solver. Lower stability results in the solver taking smaller time steps, which results in more computational time; in the extreme case of low stability, the solver cannot converge or takes an impractical amount of time to solve the model. During the multiple-cycle simulation, the convergence is found to become more difficult as the simulation progresses in time; it can be concluded from this behaviour that the model solution becomes less stable over many cycles. While a definitive cause for this decrease in stability over time has not been determined, the decrease in TEOA permeation over time may play a role due to its expected effect on the TEOA concentration in the positive electrolyte. The nonlinearity of the model equations and model complexity are also likely to contribute to the lack of model stability.

7.2 Recommendations

The following recommendations are presented for further development and analysis of the redox flow battery considered in the present work.

1. Given that the hydrogen evolution reaction kinetic parameters used in the model are fit based on the charge and discharge curves for the present redox flow battery system, it is recommended that the kinetics of hydrogen evolution under these conditions be investigated. Experiments similar to those conducted for the main redox couples of this battery could be performed to determine the formal potential and standard rate constant for the hydrogen evolution reaction in this RFB system. The model could then be updated to reflect this information to improve its accuracy.
2. The treatment of the ion exchange membrane as a purely resistive element has been adequate for modelling the system; however, a more general formulation of the membrane model would be beneficial to evaluate the validity of assumptions made in the present work. If the membrane

model were modified to consider multi-species transport by diffusion, convection, and migration, this would result in a more accurate depiction of the ion exchange membrane. Such a model would be able to operate without the assumption that a single charge carrier is responsible for the entirety of the membrane current, which is not entirely valid for the present membrane under alkaline conditions. Constructing this model would enable us to evaluate the validity of the assumption that hydroxide is the predominant charge carrier. The model may also enable phenomena such as osmotic and electro-osmotic transport to be considered, which would enable more accurate consideration of TEOA transport as well as water transport across the membrane. Based on the experience with the present model, it is likely that such a modification would result in model instability, perhaps to a great enough extent that it cannot be solved with the present solver settings. It is therefore recommended that a more comprehensive membrane model that is able to consider multiple transport phenomena and multiple charge carriers be investigated.

3. Membrane transport has been found to account for most of the resistance in the present redox flow battery. The facile kinetics of the main redox reactions and good mass transfer of electroactive species imply that the best voltage efficiency gains are likely to come from reducing membrane resistance. Although a cation exchange membrane has been selected for this battery, an anion exchange membrane is more appropriate from a transport point of view for this system that operates under alkaline conditions where the predominant charge carriers are hydroxide anions. This choice of membrane may be partially responsible for the magnitude of membrane resistance observed. An anion exchange membrane may be a good candidate to replace the existing membrane in this redox flow battery, as it would ideally be more highly selective to hydroxide ions and allow them to flow with less resistance. Thus, it is recommended

that alternative ion exchange membranes such as anion exchange membranes be investigated to improve the performance of this redox flow battery.

4. Some of the most significant limitations of the present model are the length of time required to solve it and the potential instability and convergence issues that occasionally emerge during this process. It can be seen from the reactant and potential profiles across both electrodes that the spatial variation within each electrode for much of the simulation is not very large. This raises the question of whether a two-dimensional transient model is strictly necessary to adequately model the system. It is recommended that a one-dimensional transient model be formulated and compared to the results obtained from the two-dimensional model. If the loss of accuracy from this reduction in dimensionality is not very severe, the significantly lower computational cost would justify the use of the one-dimensional model. If a one-dimensional model were found to be acceptable, it could be used to more rapidly conduct preliminary simulations for purposes such as optimization. The existing two-dimensional model could be reserved for more detailed and accurate calculations, such as those that deal explicitly with spatial variation in model variables, as needed. As discussed in Chapter 3, one-dimensional models have been formulated for other RFB systems such as all-vanadium but have not yet been developed for the present system.
5. A prediction from the model that has come from the multiple-cycle simulation results is that the discharge-limiting reaction changes from the positive electrode reaction to the negative electrode reaction as the battery is cycled continuously. It is recommended that the multi-cycle testing of the redox flow battery be repeated, with the negative and positive electrode potentials measured independently. The individual electrode potentials have only been measured during the single-cycle run and are the basis for the conclusion that the positive electrode reaction is the discharge-limiting reaction due to the fact that only the positive

electrode potential changes significantly at the end of discharge. The availability of these data for the multiple-cycle run would enable further validation of the conclusion that the iron-triethanolamine reaction becomes the discharge-limiting reaction.

6. The instability and convergence challenges encountered in the solution of the model have prevented the simulation of more than approximately 70 consecutive cycles of the flow battery system. It would be useful to be able to simulate more cycles since the experimental data reported by Gong et al.[17] include 110 consecutive cycles. One strategy that may improve the number of cycles that can be simulated would be to partition the solution process into segments of a certain number of cycles; the solver could then be run for each partition, stopped, and then reinitialized for the next partition with initial conditions corresponding to the end state of the previous partition. If this process were automated, the model would be able to continue until the point at which it is unable to converge without risking loss of most of the results obtained prior to that point. The use of a one-dimensional model would also likely enable the model to simulate more cycles due to its reduced complexity and faster expected solution time. Investigation of other solution algorithms and solver settings to find an optimal solver configuration for this specific application may also improve the stability of the model. It is therefore recommended that steps be taken to improve the stability and convergence of the present model for the purpose of simulating a greater number of consecutive cycles.

References

(1) Naterer, G. F.; Fowler, M.; Cotton, J.; Gabriel, K. Synergistic Roles of Off-Peak Electrolysis and Thermochemical Production of Hydrogen from Nuclear Energy in Canada. *Int. J. Hydrogen Energy* **2008**, *33* (23), 6849–6857. https://doi.org/10.1016/j.ijhydene.2008.09.011.

(2) Horvath, A.; Rachlew, E. Nuclear Power in the 21st Century: Challenges and Possibilities. *Ambio* **2016**, *45* (1), 38–49. https://doi.org/10.1007/s13280-015-0732-y.

(3) Figueiredo, F. C.; Flynn, P. C. Using Diurnal Power Price to Configure Pumped Storage. *IEEE Trans. Energy Convers.* **2006**, *21* (3), 804–809. https://doi.org/10.1109/TEC.2006.877373.

(4) *Battery Storage in the United States: An Update on Market Trends*; U.S. Department of Energy, U.S. Energy Information Administration: Washington, DC, 2020.

(5) Doluweera, G.; Rahmanifard, H.; Ahmadi, M. *Electricity Storage Systems: Applications and Business Cases*; Canadian Energy Research Institute: Calgary, AB, 2019.

(6) Bolund, B.; Bernhoff, H.; Leijon, M. Flywheel Energy and Power Storage Systems. *Renew. Sustain. Energy Rev.* **2007**, *11* (2), 235–258. https://doi.org/10.1016/j.rser.2005.01.004.

(7) Lund, H.; Salgi, G. The Role of Compressed Air Energy Storage (CAES) in Future Sustainable Energy Systems. *Energy Convers. Manag.* **2009**, *50* (5), 1172–1179. https://doi.org/10.1016/j.enconman.2009.01.032.

(8) Götz, M.; Lefebvre, J.; Mörs, F.; McDaniel Koch, A.; Graf, F.; Bajohr, S.; Reimert, R.; Kolb, T. Renewable Power-to-Gas: A Technological and Economic Review. *Renew. Energy* **2016**, *85*, 1371–1390. https://doi.org/10.1016/j.renene.2015.07.066.

(9) Sawai, K.; Ohzuku, T. Factors Affecting Rate Capability of Graphite Electrodes for Lithium-Ion Batteries. *J. Electrochem. Soc.* **2003**, *150* (6), A674. https://doi.org/10.1149/1.1568107.

(10) Zheng, H.; Li, J.; Song, X.; Liu, G.; Battaglia, V. S. A Comprehensive Understanding of Electrode Thickness Effects on the Electrochemical Performances of Li-Ion Battery Cathodes. *Electrochim. Acta* **2012**, *71*, 258–265. https://doi.org/10.1016/j.electacta.2012.03.161.

(11) Mei, W.; Chen, H.; Sun, J.; Wang, Q. The Effect of Electrode Design Parameters on Battery Performance and Optimization of Electrode Thickness Based on the Electrochemical–Thermal Coupling Model. *Sustain. Energy Fuels* **2019**, *3* (1), 148–165. https://doi.org/10.1039/C8SE00503F.

(12) Lucas, A.; Chondrogiannis, S. Smart Grid Energy Storage Controller for Frequency Regulation and Peak Shaving, Using a Vanadium Redox Flow Battery. *Int. J. Electr. Power Energy Syst.* **2016**, *80*, 26–36. https://doi.org/10.1016/j.ijepes.2016.01.025.

(13) Li, L.; Kim, S.; Wang, W.; Vijayakumar, M.; Nie, Z.; Chen, B.; Zhang, J.; Xia, G.; Hu, J.; Graff, G.; Liu, J.; Yang, Z. A Stable Vanadium Redox-Flow Battery with High Energy Density for Large-Scale Energy Storage. *Adv. Energy Mater.* **2011**, *1* (3), 394–400. https://doi.org/10.1002/aenm.201100008.

(14) Xu, N.; Li, X.; Zhao, X.; Goodenough, J. B.; Huang, K. A Novel Solid Oxide Redox Flow Battery for Grid Energy Storage. *Energy Environ. Sci.* **2011**, *4* (12), 4942–4946. https://doi.org/10.1039/C1EE02489B.

(15) Tucker, M. C.; Phillips, A.; Weber, A. Z. All-Iron Redox Flow Battery Tailored for Off-Grid Portable Applications. *ChemSusChem* **2015**, *8* (23), 3996–4004. https://doi.org/10.1002/cssc.201500845.

(16) Wang, W.; Luo, Q.; Li, B.; Wei, X.; Li, L.; Yang, Z. Recent Progress in Redox Flow Battery Research and Development. *Adv. Funct. Mater.* **2013**, *23* (8), 970–986. https://doi.org/10.1002/adfm.201200694.

(17) Gong, K.; Xu, F.; B. Grunewald, J.; Ma, X.; Zhao, Y.; Gu, S.; Yan, Y. All-Soluble All-Iron Aqueous Redox-Flow Battery. *ACS Energy Lett.* **2016**, *1* (1), 89–93. https://doi.org/10.1021/acsenergylett.6b00049.

(18) Yin, C.; Gao, Y.; Guo, S.; Tang, H. A Coupled Three Dimensional Model of Vanadium Redox Flow Battery for Flow Field Designs. *Energy* **2014**, *74*, 886–895. https://doi.org/10.1016/j.energy.2014.07.066.

(19) Zheng, Q.; Xing, F.; Li, X.; Ning, G.; Zhang, H. Flow Field Design and Optimization Based on the Mass Transport Polarization Regulation in a Flow-through Type Vanadium Flow Battery. *J. Power Sources* **2016**, *324*, 402–411. https://doi.org/10.1016/j.jpowsour.2016.05.110.

(20) Bhattarai, A.; Whitehead, A. H.; Schweiss, R.; Scherer, G. G.; Skyllas-Kazacos, M.; Wai, N.; Nguyen, T. D.; Ghimire, P. C.; Oo, M. O.; Hng, H. H. Anomalous Behavior of Anion Exchange Membrane during Operation of a Vanadium Redox Flow Battery. *ACS Appl. Energy Mater.* **2019**, *2* (3), 1712–1719. https://doi.org/10.1021/acsaem.8b01816.

(21) Kwabi, D. G.; Lin, K.; Ji, Y.; Kerr, E. F.; Goulet, M.-A.; De Porcellinis, D.; Tabor, D. P.; Pollack, D. A.; Aspuru-Guzik, A.; Gordon, R. G.; Aziz, M. J. Alkaline Quinone Flow Battery with Long Lifetime at PH 12. *Joule* **2018**, *2* (9), 1894–1906. https://doi.org/10.1016/j.joule.2018.07.005.

(22) Ji, Y.; Goulet, M.-A.; Pollack, D. A.; Kwabi, D. G.; Jin, S.; De Porcellinis, D.; Kerr, E. F.; Gordon, R. G.; Aziz, M. J. A Phosphonate-Functionalized Quinone Redox Flow Battery at Near-Neutral PH with Record Capacity Retention Rate. *Adv. Energy Mater.* **2019**, *9* (12), 1900039. https://doi.org/10.1002/aenm.201900039.

(23) Goulet, M.-A.; Aziz, M. J. Flow Battery Molecular Reactant Stability Determined by Symmetric Cell Cycling Methods. *J. Electrochem. Soc.* **2018**, *165* (7), A1466–A1477. https://doi.org/10.1149/2.0891807jes.

(24) Zhang, C.; Zhao, T. S.; Xu, Q.; An, L.; Zhao, G. Effects of Operating Temperature on the Performance of Vanadium Redox Flow Batteries. *Appl. Energy* **2015**, *155*, 349–353. https://doi.org/10.1016/j.apenergy.2015.06.002.

(25) Xi, J.; Xiao, S.; Yu, L.; Wu, L.; Liu, L.; Qiu, X. Broad Temperature Adaptability of Vanadium Redox Flow Battery—Part 2: Cell Research. *Electrochim. Acta* **2016**, *191*, 695–704. https://doi.org/10.1016/j.electacta.2016.01.165.

(26) Tang, A.; Bao, J.; Skyllas-Kazacos, M. Thermal Modelling of Battery Configuration and Self-Discharge Reactions in Vanadium Redox Flow Battery. *J. Power Sources* **2012**, *216*, 489–501. https://doi.org/10.1016/j.jpowsour.2012.06.052.

(27) Kausar, N.; Mousa, A.; Skyllas-Kazacos, M. The Effect of Additives on the High-Temperature Stability of the Vanadium Redox Flow Battery Positive Electrolytes. *ChemElectroChem* **2016**, *3* (2), 276–282. https://doi.org/10.1002/celc.201500453.

(28) Holze, R. MEASUREMENT METHODS | Electrochemical: Potential and Current Steps. In *Encyclopedia of Electrochemical Power Sources*; Garche, J., Ed.; Elsevier: Amsterdam, 2009; pp 655–659. https://doi.org/10.1016/B978-044452745-5.00070-8.

(29) Mirceski, V.; Laborda, E.; Guziejewski, D.; Compton, R. G. New Approach to Electrode Kinetic Measurements in Square-Wave Voltammetry: Amplitude-Based Quasireversible Maximum. *Anal. Chem.* **2013**, *85* (11), 5586–5594. https://doi.org/10.1021/ac4008573.

(30) Nicholson, R. S. Theory and Application of Cyclic Voltammetry for Measurement of Electrode Reaction Kinetics. *Anal. Chem.* **1965**, *37* (11), 1351–1355. https://doi.org/10.1021/ac60230a016.

(31) Elgrishi, N.; Rountree, K. J.; McCarthy, B. D.; Rountree, E. S.; Eisenhart, T. T.; Dempsey, J. L. A Practical Beginner's Guide to Cyclic Voltammetry. *J. Chem. Educ.* **2018**, *95* (2), 197–206. https://doi.org/10.1021/acs.jchemed.7b00361.

(32) Wang, W.; Wei, X.; Choi, D.; Lu, X.; Yang, G.; Sun, C. Chapter 1 - Electrochemical Cells for Medium- and Large-Scale Energy Storage: Fundamentals. In *Advances in Batteries for Medium and Large-Scale Energy Storage*; Menictas, C., Skyllas-Kazacos, M., Lim, T. M., Eds.; Woodhead Publishing, 2015; pp 3–28. https://doi.org/10.1016/B978-1-78242-013-2.00001-7.

(33) Burheim, O. S. Chapter 6 - Electrochemical Energy Storage. In *Engineering Energy Storage*; Burheim, O. S., Ed.; Academic Press, 2017; pp 75–110. https://doi.org/10.1016/B978-0-12-814100-7.00006-7.

(34) Aaron, D.; Tang, Z.; Papandrew, A. B.; Zawodzinski, T. A. Polarization Curve Analysis of All-Vanadium Redox Flow Batteries. *J. Appl. Electrochem.* **2011**, *41* (10), 1175. https://doi.org/10.1007/s10800-011-0335-7.

(35) Song, Y.; Evans, C. E. Method and System for Rebalancing Electrolytes in a Redox Flow Battery System. U.S. Patent 9806366, October 31, 2017.

(36) Perry, M. L.; Smeltz, A.; Xie, W. Rebalancing Electrolyte Concentration in Flow Battery Using Pressure Differential. U.S. Patent 10050290, August 14, 2018.

(37) Keshavarz, M.; Karuppaiah, C.; Zu, G.; Sahu, S. K.; Nair, S. K. S.; Mani, V.; Parakulam, G. R.; Firouzi, A.; Rasu, V. Redox Flow Cell Rebalancing. U.S. Patent 8877365, November 4, 2014.

(38) Gahn, R. F. Method and Apparatus for Rebalancing a Redox Flow Cell System. U.S. Patent 4576878, March 18, 1986.

(39) Chang, O. K.; Pham, A. Q. Rebalancing Electrolytes in Redox Flow Battery Systems. U.S. Patent 8916281, December 23, 2014.

(40) Thaller, L. H. Electrochemical Cell for Rebalancing Redox Flow System. U.S. Patent 4159366, June 26, 1979.

(41) Winsberg, J.; Hagemann, T.; Muench, S.; Friebe, C.; Häupler, B.; Janoschka, T.; Morgenstern, S.; Hager, M. D.; Schubert, U. S. Poly(Boron-Dipyrromethene)—A Redox-Active Polymer Class for Polymer Redox-Flow Batteries. *Chem. Mater.* **2016**, *28* (10), 3401–3405. https://doi.org/10.1021/acs.chemmater.6b00640.

(42) Kangro, W. Verfahren Zur Speicherung von Elektrischer Energie. Germany Patent 914264, June 28, 1954.

(43) Thaller, L. H. Recent Advances in Redox Flow Cell Storage Systems. In *Proceedings of the 14th Intersociety Energy Conversion Engineering Conference*; 1979; Vol. 1, pp 715–721.

(44) Waters, S. E.; Robb, B. H.; Marshak, M. P. Effect of Chelation on Iron–Chromium Redox Flow Batteries. *ACS Energy Lett.* **2020**, *5* (6), 1758–1762. https://doi.org/10.1021/acsenergylett.0c00761.

(45) Zeng, Y. K.; Zhao, T. S.; An, L.; Zhou, X. L.; Wei, L. A Comparative Study of All-Vanadium and Iron-Chromium Redox Flow Batteries for Large-Scale Energy Storage. *J. Power Sources* **2015**, *300*, 438–443. https://doi.org/10.1016/j.jpowsour.2015.09.100.

(46) Zeng, Y. K.; Zhao, T. S.; Zhou, X. L.; Zeng, L.; Wei, L. The Effects of Design Parameters on the Charge-Discharge Performance of Iron-Chromium Redox Flow Batteries. *Appl. Energy* **2016**, *182*, 204–209. https://doi.org/10.1016/j.apenergy.2016.08.135.

(47) Zeng, Y. K.; Zhou, X. L.; Zeng, L.; Yan, X. H.; Zhao, T. S. Performance Enhancement of Iron-Chromium Redox Flow Batteries by Employing Interdigitated Flow Fields. *J. Power Sources* **2016**, *327*, 258–264. https://doi.org/10.1016/j.jpowsour.2016.07.066.

(48) Zeng, Y. K.; Zhou, X. L.; An, L.; Wei, L.; Zhao, T. S. A High-Performance Flow-Field Structured Iron-Chromium Redox Flow Battery. *J. Power Sources* **2016**, *324*, 738–744. https://doi.org/10.1016/j.jpowsour.2016.05.138.

(49) Wang, S.; Xu, Z.; Wu, X.; Zhao, H.; Zhao, J.; Liu, J.; Yan, C.; Fan, X. Analyses and Optimization of Electrolyte Concentration on the Electrochemical Performance of Iron-Chromium Flow Battery. *Appl. Energy* **2020**, *271*, 115252. https://doi.org/10.1016/j.apenergy.2020.115252.

(50) Chen, N.; Zhang, H.; Luo, X.-D.; Sun, C.-Y. SiO2-Decorated Graphite Felt Electrode by Silicic Acid Etching for Iron-Chromium Redox Flow Battery. *Electrochim. Acta* **2020**, *336*, 135646. https://doi.org/10.1016/j.electacta.2020.135646.

(51) Sun, C.-Y.; Zhang, H. Investigation of Nafion Series Membranes on the Performance of Iron-Chromium Redox Flow Battery. *Int. J. Energy Res.* **2019**, *43* (14), 8739–8752. https://doi.org/10.1002/er.4875.

(52) Jiang, H. R.; Sun, J.; Wei, L.; Wu, M. C.; Shyy, W.; Zhao, T. S. A High Power Density and Long Cycle Life Vanadium Redox Flow Battery. *Energy Storage Mater.* **2020**, *24*, 529–540. https://doi.org/10.1016/j.ensm.2019.07.005.

(53) Yu, L.; Lin, F.; Xiao, W.; Xu, L.; Xi, J. Achieving Efficient and Inexpensive Vanadium Flow Battery by Combining CexZr1−xO2 Electrocatalyst and Hydrocarbon Membrane. *Chem. Eng. J.* **2019**, *356*, 622–631. https://doi.org/10.1016/j.cej.2018.09.069.

(54) Chen, D.; Chen, X.; Ding, L.; Li, X. Advanced Acid-Base Blend Ion Exchange Membranes with High Performance for Vanadium Flow Battery Application. *J. Memb. Sci.* **2018**, *553*, 25–31. https://doi.org/10.1016/j.memsci.2018.02.039.

(55) Xi, J.; Jiang, B.; Yu, L.; Liu, L. Membrane Evaluation for Vanadium Flow Batteries in a Temperature Range of −20–50°C. *J. Memb. Sci.* **2017**, *522*, 45–55. https://doi.org/10.1016/j.memsci.2016.09.012.

(56) Yu, L.; Xi, J. Durable and Efficient PTFE Sandwiched SPEEK Membrane for Vanadium Flow Batteries. *ACS Appl. Mater. Interfaces* **2016**, *8* (36), 23425–23430. https://doi.org/10.1021/acsami.6b07782.

(57) Chen, F.; Che, X.; Ren, X.; Zhao, L.; Zhang, D.; Chen, H.; Liu, J.; Yang, J. Polybenzimidazole and Polyvinylpyrrolidone Blend Membranes for Vanadium Flow Battery. *J. Electrochem. Soc.* **2020**, *167* (6), 60511. https://doi.org/10.1149/1945-7111/ab823a.

(58) Liu, S.; Sang, X.; Wang, L.; Zhang, J.; Song, J.; Han, B. Incorporation of Metal-Organic Framework in Polymer Membrane Enhances Vanadium Flow Battery Performance. *Electrochim. Acta* **2017**, *257*, 243–249. https://doi.org/10.1016/j.electacta.2017.10.084.

(59) Ma, Y.; Li, L.; Ma, L.; Qaisrani, N. A.; Gong, S.; Li, P.; Zhang, F.; He, G. Cyclodextrin Templated Nanoporous Anion Exchange Membrane for Vanadium Flow Battery Application. *J. Memb. Sci.* **2019**, *586*, 98–105. https://doi.org/10.1016/j.memsci.2019.05.055.

(60) Jing, M.; Wei, Z.; Su, W.; He, H.; Fan, X.; Qin, Y.; Liu, J.; Yan, C. Improved Electrochemical Performance for Vanadium Flow Battery by Optimizing the Concentration of the Electrolyte. *J. Power Sources* **2016**, *324*, 215–223. https://doi.org/10.1016/j.jpowsour.2016.05.099.

(61) Chakrabarti, M. H.; Hajimolana, S. A.; Mjalli, F. S.; Saleem, M.; Mustafa, I. Redox Flow Battery for Energy Storage. *Arab. J. Sci. Eng.* **2013**, *38* (4), 723–739. https://doi.org/10.1007/s13369-012-0356-5.

(62) Souentie, S.; Amr, I.; Alsuhaibani, A.; Almazroei, E.; Hammad, A. D. Temperature, Charging Current and State of Charge Effects on Iron-Vanadium Flow Batteries Operation. *Appl. Energy* **2017**, *206*, 568–576. https://doi.org/10.1016/j.apenergy.2017.08.089.

(63) Lee, W.; Kwon, B. W.; Jung, M.; Serhiichuk, D.; Henkensmeier, D.; Kwon, Y. Iron-Vanadium Redox Flow Batteries with Polybenzimidazole Membranes: High Coulomb Efficiency and Low Capacity Loss. *J. Power Sources* **2019**, *439*, 227079. https://doi.org/10.1016/j.jpowsour.2019.227079.

(64) Wang, W.; Nie, Z.; Chen, B.; Chen, F.; Luo, Q.; Wei, X.; Xia, G.-G.; Skyllas-Kazacos, M.; Li, L.; Yang, Z. A New Fe/V Redox Flow Battery Using a Sulfuric/Chloric Mixed-Acid Supporting Electrolyte. *Adv. Energy Mater.* **2012**, *2* (4), 487–493. https://doi.org/10.1002/aenm.201100527.

(65) Zhao, P.; Zhang, H.; Zhou, H.; Yi, B. Nickel Foam and Carbon Felt Applications for Sodium Polysulfide/Bromine Redox Flow Battery Electrodes. *Electrochim. Acta* **2005**, *51* (6), 1091–1098. https://doi.org/10.1016/j.electacta.2005.06.008.

(66) Zhou, H.; Zhang, H.; Zhao, P.; Yi, B. A Comparative Study of Carbon Felt and Activated Carbon Based Electrodes for Sodium Polysulfide/Bromine Redox Flow Battery. *Electrochim. Acta* **2006**, *51* (28), 6304–6312. https://doi.org/10.1016/j.electacta.2006.03.106.

(67) Zhou, H.; Zhang, H.; Zhao, P.; Yi, B. Novel Cobalt Coated Carbon Felt as High Performance Negative Electrode in Sodium Polysulfide/Bromine Redox Flow Battery. *Electrochemistry* **2006**, *74* (4), 296–298. https://doi.org/10.5796/electrochemistry.74.296.

(68) Ge, S. H.; Yi, B. L.; Zhang, H. M. Study of a High Power Density Sodium Polysulfide/Bromine Energy Storage Cell. *J. Appl. Electrochem.* **2004**, *34* (2), 181–185. https://doi.org/10.1023/B:JACH.0000009936.82613.ad.

(69) Leung, P. K.; Mohamed, M. R.; Shah, A. A.; Xu, Q.; Conde-Duran, M. B. A Mixed Acid Based Vanadium–Cerium Redox Flow Battery with a Zero-Gap Serpentine Architecture. *J. Power Sources* **2015**, *274*, 651–658. https://doi.org/10.1016/j.jpowsour.2014.10.034.

(70) Sankarasubramanian, S.; Zhang, Y.; Ramani, V. Methanesulfonic Acid-Based Electrode-Decoupled Vanadium–Cerium Redox Flow Battery Exhibits Significantly Improved Capacity and Cycle Life. *Sustain. Energy Fuels* **2019**, *3* (9), 2417–2425. https://doi.org/10.1039/C9SE00286C.

(71) Yun, S.; Parrondo, J.; Ramani, V. A Vanadium–Cerium Redox Flow Battery with an Anion-Exchange Membrane Separator. *Chempluschem* **2015**, *80* (2), 412–421. https://doi.org/10.1002/cplu.201402096.

(72) Wang, Z.; Parrondo, J.; Ramani, V. Polystyrene-Block-Poly(Ethylene-Ran-Butylene)-Block-Polystyrene Triblock Copolymer Separators for a Vanadium-Cerium Redox Flow Battery. *J. Electrochem. Soc.* **2017**, *164* (4), F372–F378. https://doi.org/10.1149/2.1301704jes.

(73) Govindan, M.; He, K.; Moon, I.-S. Evaluation of Dual Electrochemical Cell Design for Cerium-Vanadium Redox Flow Battery to Use Different Combination of Electrodes. *Int. J. Electrochem. Sci.* **2013**, *8* (8), 10265–10279.

(74) Vafiadis, H.; Skyllas-Kazacos, M. Evaluation of Membranes for the Novel Vanadium Bromine Redox Flow Cell. *J. Memb. Sci.* **2006**, *279* (1), 394–402. https://doi.org/10.1016/j.memsci.2005.12.028.

(75) Kim, D.; Kim, Y.; Lee, Y.; Jeon, J. 1,2-Dimethylimidazole Based Bromine Complexing Agents for Vanadium Bromine Redox Flow Batteries. *Int. J. Hydrogen Energy* **2019**, *44* (23), 12024–12032. https://doi.org/10.1016/j.ijhydene.2019.03.050.

(76) Wang, Y. Y.; Lin, M. R.; Wan, C. C. A Study of the Discharge Performance of the Ti/Fe Redox Flow System. *J. Power Sources* **1984**, *13* (1), 65–74. https://doi.org/10.1016/0378-7753(84)80054-3.

(77) Savinell, R. F.; Liu, C. C.; Galasco, R. T.; Chiang, S. H.; Coetzee, J. F. Discharge Characteristics of a Soluble Iron-Titanium Battery System. *J. Electrochem. Soc.* **1979**, *126* (3), 357–360. https://doi.org/10.1149/1.2129043.

(78) Reynard, D.; Maye, S.; Peljo, P.; Chanda, V.; Girault, H. H.; Gentil, S. Vanadium–Manganese Redox Flow Battery: Study of MnIII Disproportionation in the Presence of Other Metallic Ions. *Chem. Eur. J.* **2020**, *26* (32), 7250–7257. https://doi.org/10.1002/chem.202000340.

(79) Lee, H. J.; Park, S.; Kim, H. Analysis of the Effect of MnO2Precipitation on the Performance of a Vanadium/Manganese Redox Flow Battery. *J. Electrochem. Soc.* **2018**, *165* (5), A952–A956. https://doi.org/10.1149/2.0881805jes.

(80) Hoyt, N. C.; Hawthorne, K. L.; Savinell, R. F.; Wainright, J. S. Plating Utilization of Carbon Felt in a Hybrid Flow Battery. *J. Electrochem. Soc.* **2015**, *163* (1), A5041–A5048. https://doi.org/10.1149/2.0061601jes.

(81) Zhou, X.; Lin, L.; Lv, Y.; Zhang, X.; Fan, L.; Wu, Q. Elucidating Effects of Component Materials and Flow Fields on Sn–Fe Hybrid Flow Battery Performance. *J. Power Sources* **2020**, *450*, 227613. https://doi.org/10.1016/j.jpowsour.2019.227613.

(82) Khor, A.; Leung, P.; Mohamed, M. R.; Flox, C.; Xu, Q.; An, L.; Wills, R. G. A.; Morante, J. R.; Shah, A. A. Review of Zinc-Based Hybrid Flow Batteries: From Fundamentals to Applications. *Mater. Today Energy* **2018**, *8*, 80–108. https://doi.org/10.1016/j.mtener.2017.12.012.

(83) Leung, P. K.; Ponce de León, C.; Walsh, F. C. An Undivided Zinc–Cerium Redox Flow Battery Operating at Room Temperature (295 K). *Electrochem. commun.* **2011**, *13* (8), 770–773. https://doi.org/10.1016/j.elecom.2011.04.011.

(84) Leung, P. K.; Ponce de Leon, C.; Walsh, F. C. The Influence of Operational Parameters on the Performance of an Undivided Zinc–Cerium Flow Battery. *Electrochim. Acta* **2012**, *80*, 7–14. https://doi.org/10.1016/j.electacta.2012.06.074.

(85) Leung, P. K.; Ponce-de-León, C.; Low, C. T. J.; Shah, A. A.; Walsh, F. C. Characterization of a Zinc–Cerium Flow Battery. *J. Power Sources* **2011**, *196* (11), 5174–5185. https://doi.org/10.1016/j.jpowsour.2011.01.095.

(86) Nikiforidis, G.; Berlouis, L.; Hall, D.; Hodgson, D. Impact of Electrolyte Composition on the Performance of the Zinc–Cerium Redox Flow Battery System. *J. Power Sources* **2013**, *243*, 691–698. https://doi.org/10.1016/j.jpowsour.2013.06.045.

(87) Nikiforidis, G.; Berlouis, L.; Hall, D.; Hodgson, D. Charge/Discharge Cycles on Pt and Pt-Ir Based Electrodes for the Positive Side of the Zinc-Cerium Hybrid Redox Flow Battery. *Electrochim. Acta* **2014**, *125*, 176–182. https://doi.org/10.1016/j.electacta.2014.01.075.

(88) Amini, K.; Pritzker, M. D. Improvement of Zinc-Cerium Redox Flow Batteries Using Mixed Methanesulfonate-Chloride Negative Electrolyte. *Appl. Energy* **2019**, *255*, 113894. https://doi.org/10.1016/j.apenergy.2019.113894.

(89) Leung, P. K.; Ponce-de-León, C.; Recio, F. J.; Herrasti, P.; Walsh, F. C. Corrosion of the Zinc Negative Electrode of Zinc–Cerium Hybrid Redox Flow Batteries in Methanesulfonic Acid. *J. Appl. Electrochem.* **2014**, *44* (9), 1025–1035. https://doi.org/10.1007/s10800-014-0714-y.

(90) Leung, P. K.; Ponce de León, C.; Low, C. T. J.; Walsh, F. C. Ce(III)/Ce(IV) in Methanesulfonic Acid as the Positive Half Cell of a Redox Flow Battery. *Electrochim. Acta* **2011**, *56* (5), 2145–2153. https://doi.org/10.1016/j.electacta.2010.12.038.

(91) Amini, K.; Pritzker, M. D. Life-Cycle Analysis of Zinc-Cerium Redox Flow Batteries. *Electrochim. Acta* **2020**, *356*, 136785. https://doi.org/10.1016/j.electacta.2020.136785.

(92) Amini, K.; Pritzker, M. D. In Situ Polarization Study of Zinc–Cerium Redox Flow Batteries. *J. Power Sources* **2020**, *471*, 228463. https://doi.org/10.1016/j.jpowsour.2020.228463.

(93) Arenas, L. F.; León, C. P. de; Walsh, F. C. Mass Transport and Active Area of Porous Pt/Ti Electrodes for the Zn-Ce Redox Flow Battery Determined from Limiting Current Measurements. *Electrochim. Acta* **2016**, *221*, 154–166. https://doi.org/10.1016/j.electacta.2016.10.097.

(94) Nikiforidis, G.; Cartwright, R.; Hodgson, D.; Hall, D.; Berlouis, L. Factors Affecting the Performance of the Zn-Ce Redox Flow Battery. *Electrochim. Acta* **2014**, *140*, 139–144. https://doi.org/10.1016/j.electacta.2014.04.150.

(95) Schneider, M.; Rajarathnam, G. P.; Easton, M. E.; Masters, A. F.; Maschmeyer, T.; Vassallo, A. M. The Influence of Novel Bromine Sequestration Agents on Zinc/Bromine Flow Battery Performance. *RSC Adv.* **2016**, *6* (112), 110548–110556. https://doi.org/10.1039/C6RA23446A.

(96) Wu, M.; Zhao, T.; Zhang, R.; Jiang, H.; Wei, L. A Zinc–Bromine Flow Battery with Improved Design of Cell Structure and Electrodes. *Energy Technol.* **2018**, *6* (2), 333–339. https://doi.org/10.1002/ente.201700481.

(97) Lai, Q.; Zhang, H.; Li, X.; Zhang, L.; Cheng, Y. A Novel Single Flow Zinc–Bromine Battery with Improved Energy Density. *J. Power Sources* **2013**, *235*, 1–4. https://doi.org/10.1016/j.jpowsour.2013.01.193.

(98) Wu, M. C.; Zhao, T. S.; Jiang, H. R.; Zeng, Y. K.; Ren, Y. X. High-Performance Zinc Bromine Flow Battery via Improved Design of Electrolyte and Electrode. *J. Power Sources* **2017**, *355*, 62–68. https://doi.org/10.1016/j.jpowsour.2017.04.058.

(99) Xiang, H.-X.; Tan, A.-D.; Piao, J.-H.; Fu, Z.-Y.; Liang, Z.-X. Efficient Nitrogen-Doped Carbon for Zinc–Bromine Flow Battery. *Small* **2019**, *15* (24), 1901848. https://doi.org/10.1002/smll.201901848.

(100) Wu, M. C.; Zhao, T. S.; Wei, L.; Jiang, H. R.; Zhang, R. H. Improved Electrolyte for Zinc-Bromine Flow Batteries. *J. Power Sources* **2018**, *384*, 232–239. https://doi.org/10.1016/j.jpowsour.2018.03.006.

(101) Hosseiny, S. S.; Saakes, M.; Wessling, M. A Polyelectrolyte Membrane-Based Vanadium/Air Redox Flow Battery. *Electrochem. commun.* **2011**, *13* (8), 751–754. https://doi.org/10.1016/j.elecom.2010.11.025.

(102) grosse Austing, J.; Nunes Kirchner, C.; Komsiyska, L.; Wittstock, G. Investigation of Crossover Processes in a Unitized Bidirectional Vanadium/Air Redox Flow Battery. *J. Power Sources* **2016**, *306*, 692–701. https://doi.org/10.1016/j.jpowsour.2015.12.052.

(103) grosse Austing, J.; Nunes Kirchner, C.; Hammer, E.-M.; Komsiyska, L.; Wittstock, G. Study of an Unitised Bidirectional Vanadium/Air Redox Flow Battery Comprising a Two-Layered Cathode. *J. Power Sources* **2015**, *273*, 1163–1170. https://doi.org/10.1016/j.jpowsour.2014.09.177.

(104) Merle, G.; Ioana, F. C.; Demco, D. E.; Saakes, M.; Hosseiny, S. S. Friedel–Crafts Crosslinked Highly Sulfonated Polyether Ether Ketone (SPEEK) Membranes for a Vanadium/Air Redox Flow Battery. *Membranes*. 2014. https://doi.org/10.3390/membranes4010001.

(105) grosse Austing, J.; Nunes Kirchner, C.; Komsiyska, L.; Wittstock, G. Layer-by-Layer Modification of Nafion Membranes for Increased Life-Time and Efficiency of Vanadium/Air Redox Flow Batteries. *J. Memb. Sci.* **2016**, *510*, 259–269. https://doi.org/10.1016/j.memsci.2016.03.005.

(106) Petek, T. J.; Hoyt, N. C.; Savinell, R. F.; Wainright, J. S. Slurry Electrodes for Iron Plating in an All-Iron Flow Battery. *J. Power Sources* **2015**, *294*, 620–626. https://doi.org/10.1016/j.jpowsour.2015.06.050.

(107) Hawthorne, K. L.; Petek, T. J.; Miller, M. A.; Wainright, J. S.; Savinell, R. F. An Investigation into Factors Affecting the Iron Plating Reaction for an All-Iron Flow Battery. *J. Electrochem. Soc.* **2014**, *162* (1), A108–A113. https://doi.org/10.1149/2.0591501jes.

(108) Jayathilake, B. S.; Plichta, E. J.; Hendrickson, M. A.; Narayanan, S. R. Improvements to the Coulombic Efficiency of the Iron Electrode for an All-Iron Redox-Flow Battery. *J. Electrochem. Soc.* **2018**, *165* (9), A1630–A1638. https://doi.org/10.1149/2.0451809jes.

(109) Wills, R. G. A.; Collins, J.; Stratton-Campbell, D.; Low, C. T. J.; Pletcher, D.; Walsh, F. C. Developments in the Soluble Lead-Acid Flow Battery. *J. Appl. Electrochem.* **2010**, *40* (5), 955–965. https://doi.org/10.1007/s10800-009-9815-4.

(110) Zhang, C. P.; Sharkh, S. M.; Li, X.; Walsh, F. C.; Zhang, C. N.; Jiang, J. C. The Performance of a Soluble Lead-Acid Flow Battery and Its Comparison to a Static Lead-Acid Battery. *Energy Convers. Manag.* **2011**, *52* (12), 3391–3398. https://doi.org/10.1016/j.enconman.2011.07.006.

(111) Oury, A.; Kirchev, A.; Bultel, Y.; Chainet, E. PbO2/Pb2+ Cycling in Methanesulfonic Acid and Mechanisms Associated for Soluble Lead-Acid Flow Battery Applications. *Electrochim. Acta* **2012**, *71*, 140–149. https://doi.org/10.1016/j.electacta.2012.03.116.

(112) Bates, A.; Mukerjee, S.; Lee, S. C.; Lee, D.-H.; Park, S. An Analytical Study of a Lead-Acid Flow Battery as an Energy Storage System. *J. Power Sources* **2014**, *249*, 207–218. https://doi.org/10.1016/j.jpowsour.2013.10.090.

(113) Krishna, M.; Fraser, E. J.; Wills, R. G. A.; Walsh, F. C. Developments in Soluble Lead Flow Batteries and Remaining Challenges: An Illustrated Review. *J. Energy Storage* **2018**, *15*, 69–90. https://doi.org/10.1016/j.est.2017.10.020.

(114) Krishna, M.; Wills, R. G. A.; Shah, A. A.; Hall, D.; Collins, J. The Separator-Divided Soluble Lead Flow Battery. *J. Appl. Electrochem.* **2018**, *48* (9), 1031–1041. https://doi.org/10.1007/s10800-018-1230-2.

(115) Lin, Y.-T.; Tan, H.-L.; Lee, C.-Y.; Chen, H.-Y. Stabilizing the Electrodeposit-Electrolyte Interphase in Soluble Lead Flow Batteries with Ethanoate Additive. *Electrochim. Acta* **2018**, *263*, 60–67. https://doi.org/10.1016/j.electacta.2018.01.013.

(116) Luo, X.; Liu, Z.; Jiang, B.; Ji, D. High Efficiency of the Lead Methanesulfonate Flow Battery Achieved by Changing the Characteristics of PbOx under Potentiostatic Conditions. *J. Energy Storage* **2019**, *24*, 100771. https://doi.org/10.1016/j.est.2019.100771.

(117) Krishna, M.; Wallis, L. P. J.; Wills, R. G. A.; Hall, D.; Shah, A. A. Measurement of Key Electrolyte Properties for Improved Performance of the Soluble Lead Flow Battery. *Int. J. Hydrogen Energy* **2017**, *42* (29), 18491–18498. https://doi.org/10.1016/j.ijhydene.2017.05.004.

(118) Xu, Q.; Zhao, T. S.; Leung, P. K. Numerical Investigations of Flow Field Designs for Vanadium Redox Flow Batteries. *Appl. Energy* **2013**, *105*, 47–56. https://doi.org/10.1016/j.apenergy.2012.12.041.

(119) Evans, T. I.; White, R. E. A Review of Mathematical Modeling of the Zinc/Bromine Flow Cell and Battery. *J. Electrochem. Soc.* **1987**, *134* (11), 2725–2733. https://doi.org/10.1149/1.2100277.

(120) Codina, G.; Aldaz, A. Scale-up Studies of an Fe/Cr Redox Flow Battery Based on Shunt Current Analysis. *J. Appl. Electrochem.* **1992**, *22* (7), 668–674. https://doi.org/10.1007/BF01092617.

(121) Li, M.; Hikihara, T. A Coupled Dynamical Model of Redox Flow Battery Based on Chemical Reaction, Fluid Flow, and Electrical Circuit. *IEICE Trans. Fundam. Electron. Commun. Comput. Sci.* **2008**, *E91.A* (7), 1741–1747. https://doi.org/10.1093/ietfec/e91-a.7.1741.

(122) Blanc, C.; Rufer, A. Multiphysics and Energetic Modeling of a Vanadium Redox Flow Battery. In *2008 IEEE International Conference on Sustainable Energy Technologies*; 2008; pp 696–701. https://doi.org/10.1109/ICSET.2008.4747096.

(123) You, D.; Zhang, H.; Chen, J. A Simple Model for the Vanadium Redox Battery. *Electrochim. Acta* **2009**, *54* (27), 6827–6836. https://doi.org/10.1016/j.electacta.2009.06.086.

(124) Shah, A. A.; Watt-Smith, M. J.; Walsh, F. C. A Dynamic Performance Model for Redox-Flow Batteries Involving Soluble Species. *Electrochim. Acta* **2008**, *53* (27), 8087–8100. https://doi.org/10.1016/j.electacta.2008.05.067.

(125) Shah, A. A.; Al-Fetlawi, H.; Walsh, F. C. Dynamic Modelling of Hydrogen Evolution Effects in the All-Vanadium Redox Flow Battery. *Electrochim. Acta* **2010**, *55* (3), 1125–1139. https://doi.org/10.1016/j.electacta.2009.10.022.

(126) Al-Fetlawi, H.; Shah, A. A.; Walsh, F. C. Non-Isothermal Modelling of the All-Vanadium Redox Flow Battery. *Electrochim. Acta* **2009**, *55* (1), 78–89. https://doi.org/10.1016/j.electacta.2009.08.009.

(127) Al-Fetlawi, H.; Shah, A. A.; Walsh, F. C. Modelling the Effects of Oxygen Evolution in the All-Vanadium Redox Flow Battery. *Electrochim. Acta* **2010**, *55* (9), 3192–3205. https://doi.org/10.1016/j.electacta.2009.12.085.

(128) Scamman, D. P.; Reade, G. W.; Roberts, E. P. L. Numerical Modelling of a Bromide–Polysulphide Redox Flow Battery: Part 1: Modelling Approach and Validation for a Pilot-Scale System. *J. Power Sources* **2009**, *189* (2), 1220–1230. https://doi.org/10.1016/j.jpowsour.2009.01.071.

(129) Chen, C. L.; Yeoh, H. K.; Chakrabarti, M. H. An Enhancement to Vynnycky's Model for the All-Vanadium Redox Flow Battery. *Electrochim. Acta* **2014**, *120*, 167–179. https://doi.org/10.1016/j.electacta.2013.12.074.

(130) Vynnycky, M. Analysis of a Model for the Operation of a Vanadium Redox Battery. *Energy* **2011**, *36* (4), 2242–2256. https://doi.org/10.1016/j.energy.2010.03.060.

(131) Li, Y.; Skyllas-Kazacos, M.; Bao, J. A Dynamic Plug Flow Reactor Model for a Vanadium Redox Flow Battery Cell. *J. Power Sources* **2016**, *311*, 57–67. https://doi.org/10.1016/j.jpowsour.2016.02.018.

(132) Yang, W. W.; He, Y. L.; Li, Y. S. Performance Modeling of a Vanadium Redox Flow Battery during Discharging. *Electrochim. Acta* **2015**, *155*, 279–287. https://doi.org/10.1016/j.electacta.2014.12.138.

(133) Ma, X.; Zhang, H.; Xing, F. A Three-Dimensional Model for Negative Half Cell of the Vanadium Redox Flow Battery. *Electrochim. Acta* **2011**, *58*, 238–246. https://doi.org/10.1016/j.electacta.2011.09.042.

(134) Ozgoli, H. A.; Elyasi, S.; Mollazadeh, M. Hydrodynamic and Electrochemical Modeling of Vanadium Redox Flow Battery. *Mech. Ind.* **2015**, *16* (2), 201. https://doi.org/10.1051/meca/2014071.

(135) Sharma, A. K.; Ling, C. Y.; Birgersson, E.; Vynnycky, M.; Han, M. Verified Reduction of Dimensionality for an All-Vanadium Redox Flow Battery Model. *J. Power Sources* **2015**, *279*, 345–350. https://doi.org/10.1016/j.jpowsour.2015.01.019.

(136) Stephenson, D.; Kim, S.; Chen, F.; Thomsen, E.; Viswanathan, V.; Wang, W.; Sprenkle, V. Electrochemical Model of the Fe/V Redox Flow Battery. *J. Electrochem. Soc.* **2012**, *159* (12), A1993–A2000. https://doi.org/10.1149/2.052212jes.

(137) Smith, S.; Firdous, I.; Wang, Q.; Esmalla, S.; Daoud, W. A. A Two-Dimensional Model of the Vanadium–Cerium Redox Flow Battery. *Electrochim. Acta* **2019**, *328*, 135019. https://doi.org/10.1016/j.electacta.2019.135019.

(138) Xu, J.; Ma, Q.; Xing, L.; Li, H.; Leung, P.; Yang, W.; Su, H.; Xu, Q. Modeling the Effect of Temperature on Performance of an Iron-Vanadium Redox Flow Battery with Deep Eutectic Solvent (DES) Electrolyte. *J. Power Sources* **2020**, *449*, 227491. https://doi.org/10.1016/j.jpowsour.2019.227491.

(139) Xu, Z.; Wang, J.; Yan, S. C.; Fan, Q.; Lund, P. D. Modeling of Zinc Bromine Redox Flow Battery with Application to Channel Design. *J. Power Sources* **2020**, *450*, 227436. https://doi.org/10.1016/j.jpowsour.2019.227436.

(140) Guo, M.; Zhao, X.; White, R. E.; Huang, K. A Multi-Physics Model for Solid Oxide Iron-Air Redox Flow Battery: Simulation of Discharge Behavior at High Current Density. *J. Electrochem. Soc.* **2013**, *160* (11), A2085–A2092. https://doi.org/10.1149/2.062311jes.

(141) Ma, Q.; Xu, Q.; Chen, Q.; Chen, Z.; Su, H.; Zhang, W. Lattice Boltzmann Model for Complex Transfer Behaviors in Porous Electrode of All Copper Redox Flow Battery with Deep Eutectic Solvent Electrolyte. *Appl. Therm. Eng.* **2019**, *160*, 114015. https://doi.org/10.1016/j.applthermaleng.2019.114015.

(142) Zhang, B. W.; Lei, Y.; Bai, B. F.; Xu, A.; Zhao, T. S. A Two-Dimensional Mathematical Model for Vanadium Redox Flow Battery Stacks Incorporating Nonuniform Electrolyte Distribution in the Flow Frame. *Appl. Therm. Eng.* **2019**, *151*, 495–505. https://doi.org/10.1016/j.applthermaleng.2019.02.037.

(143) Oh, K.; Yoo, H.; Ko, J.; Won, S.; Ju, H. Three-Dimensional, Transient, Nonisothermal Model of All-Vanadium Redox Flow Batteries. *Energy* **2015**, *81*, 3–14. https://doi.org/10.1016/j.energy.2014.05.020.

(144) Wang, Y.; Cho, S. C. Analysis and Three-Dimensional Modeling of Vanadium Flow Batteries. *J. Electrochem. Soc.* **2014**, *161* (9), A1200–A1212. https://doi.org/10.1149/2.0061409jes.

(145) Zheng, Q.; Zhang, H.; Xing, F.; Ma, X.; Li, X.; Ning, G. A Three-Dimensional Model for Thermal Analysis in a Vanadium Flow Battery. *Appl. Energy* **2014**, *113*, 1675–1685. https://doi.org/10.1016/j.apenergy.2013.09.021.

(146) Trovò, A.; Marini, G.; Sutto, A.; Alotto, P.; Giomo, M.; Moro, F.; Guarnieri, M. Standby Thermal Model of a Vanadium Redox Flow Battery Stack with Crossover and Shunt-Current Effects. *Appl. Energy* **2019**, *240*, 893–906. https://doi.org/10.1016/j.apenergy.2019.02.067.

(147) Tang, A.; Ting, S.; Bao, J.; Skyllas-Kazacos, M. Thermal Modelling and Simulation of the All-Vanadium Redox Flow Battery. *J. Power Sources* **2012**, *203*, 165–176. https://doi.org/10.1016/j.jpowsour.2011.11.079.

(148) Wei, Z.; Zhao, J.; Xiong, B. Dynamic Electro-Thermal Modeling of All-Vanadium Redox Flow Battery with Forced Cooling Strategies. *Appl. Energy* **2014**, *135*, 1–10. https://doi.org/10.1016/j.apenergy.2014.08.062.

(149) Tsushima, S.; Suzuki, T. Modeling and Simulation of Vanadium Redox Flow Battery with Interdigitated Flow Field for Optimizing Electrode Architecture. *J. Electrochem. Soc.* **2020**, *167* (2), 20553. https://doi.org/10.1149/1945-7111/ab6dd0.

(150) Ishitobi, H.; Saito, J.; Sugawara, S.; Oba, K.; Nakagawa, N. Visualized Cell Characteristics by a Two-Dimensional Model of Vanadium Redox Flow Battery with Interdigitated Channel and Thin Active Electrode. *Electrochim. Acta* **2019**, *313*, 513–522. https://doi.org/10.1016/j.electacta.2019.04.055.

(151) Yin, C.; Gao, Y.; Xie, G.; Li, T.; Tang, H. Three Dimensional Multi-Physical Modeling Study of Interdigitated Flow Field in Porous Electrode for Vanadium Redox Flow Battery. *J. Power Sources* **2019**, *438*, 227023. https://doi.org/10.1016/j.jpowsour.2019.227023.

(152) Ke, X.; Prahl, J. M.; Alexander, J. I. D.; Savinell, R. F. Mathematical Modeling of Electrolyte Flow in a Segment of Flow Channel over Porous Electrode Layered System in Vanadium Flow Battery with Flow Field Design. *Electrochim. Acta* **2017**, *223*, 124–134. https://doi.org/10.1016/j.electacta.2016.12.017.

(153) Wang, Q.; Qu, Z. G.; Jiang, Z. Y.; Yang, W. W. Numerical Study on Vanadium Redox Flow Battery Performance with Non-Uniformly Compressed Electrode and Serpentine Flow Field. *Appl. Energy* **2018**, *220*, 106–116. https://doi.org/10.1016/j.apenergy.2018.03.058.

(154) Messaggi, M.; Canzi, P.; Mereu, R.; Baricci, A.; Inzoli, F.; Casalegno, A.; Zago, M. Analysis of Flow Field Design on Vanadium Redox Flow Battery Performance: Development of 3D Computational Fluid Dynamic Model and Experimental Validation. *Appl. Energy* **2018**, *228*, 1057–1070. https://doi.org/10.1016/j.apenergy.2018.06.148.

(155) Banerjee, R.; Bevilacqua, N.; Mohseninia, A.; Wiedemann, B.; Wilhelm, F.; Scholta, J.; Zeis, R. Carbon Felt Electrodes for Redox Flow Battery: Impact of Compression on Transport Properties. *J. Energy Storage* **2019**, *26*, 100997. https://doi.org/10.1016/j.est.2019.100997.

(156) Lu, M.-Y.; Yang, W.-W.; Bai, X.-S.; Deng, Y.-M.; He, Y.-L. Performance Improvement of a Vanadium Redox Flow Battery with Asymmetric Electrode Designs. *Electrochim. Acta* **2019**, *319*, 210–226. https://doi.org/10.1016/j.electacta.2019.06.158.

(157) Qiu, G.; Joshi, A. S.; Dennison, C. R.; Knehr, K. W.; Kumbur, E. C.; Sun, Y. 3-D Pore-Scale Resolved Model for Coupled Species/Charge/Fluid Transport in a Vanadium Redox Flow Battery. *Electrochim. Acta* **2012**, *64*, 46–64. https://doi.org/10.1016/j.electacta.2011.12.065.

(158) Knehr, K. W.; Agar, E.; Dennison, C. R.; Kalidindi, A. R.; Kumbur, E. C. A Transient Vanadium Flow Battery Model Incorporating Vanadium Crossover and Water Transport through the Membrane. *J. Electrochem. Soc.* **2012**, *159* (9), A1446–A1459. https://doi.org/10.1149/2.017209jes.

(159) You, D.; Zhang, H.; Sun, C.; Ma, X. Simulation of the Self-Discharge Process in Vanadium Redox Flow Battery. *J. Power Sources* **2011**, *196* (3), 1578–1585. https://doi.org/10.1016/j.jpowsour.2010.08.036.

(160) Yuan, C.; Xing, F.; Zheng, Q.; Zhang, H.; Li, X.; Ma, X. Factor Analysis of the Uniformity of the Transfer Current Density in Vanadium Flow Battery by an Improved Three-Dimensional Transient Model. *Energy* **2020**, *194*, 116839. https://doi.org/10.1016/j.energy.2019.116839.

(161) Merei, G.; Adler, S.; Magnor, D.; Leuthold, M.; Sauer, D. U. Multi-Physics Model for a Vanadium Redox Flow Battery. *Energy Procedia* **2014**, *46*, 194–203. https://doi.org/10.1016/j.egypro.2014.01.173.

(162) Wei, Z.; Bhattarai, A.; Zou, C.; Meng, S.; Lim, T. M.; Skyllas-Kazacos, M. Real-Time Monitoring of Capacity Loss for Vanadium Redox Flow Battery. *J. Power Sources* **2018**, *390*, 261–269. https://doi.org/10.1016/j.jpowsour.2018.04.063.

(163) Pugach, M.; Kondratenko, M.; Briola, S.; Bischi, A. Zero Dimensional Dynamic Model of Vanadium Redox Flow Battery Cell Incorporating All Modes of Vanadium Ions Crossover. *Appl. Energy* **2018**, *226*, 560–569. https://doi.org/10.1016/j.apenergy.2018.05.124.

(164) Tang, A.; Bao, J.; Skyllas-Kazacos, M. Dynamic Modelling of the Effects of Ion Diffusion and Side Reactions on the Capacity Loss for Vanadium Redox Flow Battery. *J. Power Sources* **2011**, *196* (24), 10737–10747. https://doi.org/10.1016/j.jpowsour.2011.09.003.

(165) Xiong, B.; Zhao, J.; Su, Y.; Wei, Z.; Skyllas-Kazacos, M. State of Charge Estimation of Vanadium Redox Flow Battery Based on Sliding Mode Observer and Dynamic Model Including Capacity Fading Factor. *IEEE Trans. Sustain. Energy* **2017**, *8* (4), 1658–1667. https://doi.org/10.1109/TSTE.2017.2699288.

(166) Barton, J. L.; Brushett, F. R. A One-Dimensional Stack Model for Redox Flow Battery Analysis and Operation. *Batteries* **2019**, *5* (1), 25. https://doi.org/10.3390/batteries5010025.

(167) Turker, B.; Arroyo Klein, S.; Hammer, E.-M.; Lenz, B.; Komsiyska, L. Modeling a Vanadium Redox Flow Battery System for Large Scale Applications. *Energy Convers. Manag.* **2013**, *66*, 26–32. https://doi.org/10.1016/j.enconman.2012.09.009.

(168) Gu, F.-C.; Chen, H.-C.; Li, K.-Y. Mathematic Modeling and Performance Analysis of Vanadium Redox Flow Battery. *Energy & Fuels* **2020**, *34* (8), 10142–10147. https://doi.org/10.1021/acs.energyfuels.0c01536.

(169) Wei, Z.; Zhao, J.; Skyllas-Kazacos, M.; Xiong, B. Dynamic Thermal-Hydraulic Modeling and Stack Flow Pattern Analysis for All-Vanadium Redox Flow Battery. *J. Power Sources* **2014**, *260*, 89–99. https://doi.org/10.1016/j.jpowsour.2014.02.108.

(170) Ontiveros, L. J.; Mercado, P. E. Modeling of a Vanadium Redox Flow Battery for Power System Dynamic Studies. *Int. J. Hydrogen Energy* **2014**, *39* (16), 8720–8727. https://doi.org/10.1016/j.ijhydene.2013.12.042.

(171) Wei, Z.; Tseng, K. J.; Wai, N.; Lim, T. M.; Skyllas-Kazacos, M. Adaptive Estimation of State of Charge and Capacity with Online Identified Battery Model for Vanadium Redox Flow Battery. *J. Power Sources* **2016**, *332*, 389–398. https://doi.org/10.1016/j.jpowsour.2016.09.123.

(172) D'Agostino, R.; Baumann, L.; Damiano, A.; Boggasch, E. A Vanadium-Redox-Flow-Battery Model for Evaluation of Distributed Storage Implementation in Residential Energy Systems. *IEEE Trans. Energy Convers.* **2015**, *30* (2), 421–430. https://doi.org/10.1109/TEC.2014.2369437.

(173) Mohamed, M. R.; Ahmad, H.; Seman, M. N. A.; Razali, S.; Najib, M. S. Electrical Circuit Model of a Vanadium Redox Flow Battery Using Extended Kalman Filter. *J. Power Sources* **2013**, *239*, 284–293. https://doi.org/10.1016/j.jpowsour.2013.03.127.

(174) Qiu, X.; Nguyen, T. A.; Guggenberger, J. D.; Crow, M. L.; Elmore, A. C. A Field Validated Model of a Vanadium Redox Flow Battery for Microgrids. *IEEE Trans. Smart Grid* **2014**, *5* (4), 1592–1601. https://doi.org/10.1109/TSG.2014.2310212.

(175) Zhang, Y.; Zhao, J.; Wang, P.; Skyllas-Kazacos, M.; Xiong, B.; Badrinarayanan, R. A Comprehensive Equivalent Circuit Model of All-Vanadium Redox Flow Battery for Power System Analysis. *J. Power Sources* **2015**, *290*, 14–24. https://doi.org/10.1016/j.jpowsour.2015.04.169.

(176) Wei, Z.; Meng, S.; Tseng, K. J.; Lim, T. M.; Soong, B. H.; Skyllas-Kazacos, M. An Adaptive Model for Vanadium Redox Flow Battery and Its Application for Online Peak Power Estimation. *J. Power Sources* **2017**, *344*, 195–207. https://doi.org/10.1016/j.jpowsour.2017.01.102.

(177) Wei, Z.; Lim, T. M.; Skyllas-Kazacos, M.; Wai, N.; Tseng, K. J. Online State of Charge and Model Parameter Co-Estimation Based on a Novel Multi-Timescale Estimator for Vanadium Redox Flow Battery. *Appl. Energy* **2016**, *172*, 169–179. https://doi.org/10.1016/j.apenergy.2016.03.103.

(178) Tang, A.; Bao, J.; Skyllas-Kazacos, M. Studies on Pressure Losses and Flow Rate Optimization in Vanadium Redox Flow Battery. *J. Power Sources* **2014**, *248*, 154–162. https://doi.org/10.1016/j.jpowsour.2013.09.071.

(179) Binyu, X.; Jiyun, Z.; Jinbin, L. Modeling of an All-Vanadium Redox Flow Battery and Optimization of Flow Rates. In *2013 IEEE Power & Energy Society General Meeting*; 2013; pp 1–5. https://doi.org/10.1109/PESMG.2013.6672599.

(180) König, S.; Suriyah, M. R.; Leibfried, T. Innovative Model-Based Flow Rate Optimization for Vanadium Redox Flow Batteries. *J. Power Sources* **2016**, *333*, 134–144. https://doi.org/10.1016/j.jpowsour.2016.09.147.

(181) Blanc, C.; Rufer, A. Optimization of the Operating Point of a Vanadium Redox Flow Battery. In *2009 IEEE Energy Conversion Congress and Exposition*; 2009; pp 2600–2605. https://doi.org/10.1109/ECCE.2009.5316566.

(182) National Center for Biotechnology Information. PubChem Compound Summary for CID 439210, Ferricyanide. https://pubchem.ncbi.nlm.nih.gov/compound/439210#section=2D-Structure (accessed May 19, 2021).

(183) National Center for Biotechnology Information. PubChem Compound Summary for CID 7618, Triethanolamine. https://pubchem.ncbi.nlm.nih.gov/compound/7618#section=2D-Structure (accessed May 19, 2021).

(184) Lê, A.; Floner, D.; Roisnel, T.; Cador, O.; Chancelier, L.; Geneste, F. Highly Soluble Fe(III)-Triethanolamine Complex Relevant for Redox Flow Batteries. *Electrochim. Acta* **2019**, *301*, 472–477. https://doi.org/10.1016/j.electacta.2019.02.017.

(185) Esswein, A. J.; Goeltz, J.; Amadeo, D. High solubility iron hexacyanides. U.S. Patent 10374248, August 6, 2019.

(186) Lenninger, M.; Aguilo-Aguayo, N.; Bechtold, T. Quantification of Triethanolamine through Measurement of Catalytic Current in Alkaline Iron-d-Gluconate Solution. *J. Electroanal. Chem.* **2018**, *830–831*, 50–55. https://doi.org/10.1016/j.jelechem.2018.10.026.

(187) Wei, X.; Xia, G.-G.; Kirby, B.; Thomsen, E.; Li, B.; Nie, Z.; Graff, G. G.; Liu, J.; Sprenkle, V.; Wang, W. An Aqueous Redox Flow Battery Based on Neutral Alkali Metal Ferri/Ferrocyanide and Polysulfide Electrolytes. *J. Electrochem. Soc.* **2015**, *163* (1), A5150–A5153. https://doi.org/10.1149/2.0221601jes.

(188) Chu, C.; Kwon, B. W.; Lee, W.; Kwon, Y. Effect of Temperature on the Performance of Aqueous Redox Flow Battery Using Carboxylic Acid Functionalized Alloxazine and Ferrocyanide Redox Couple. *Korean J. Chem. Eng.* **2019**, *36* (10), 1732–1739. https://doi.org/10.1007/s11814-019-0374-z.

(189) Lee, W.; Kwon, B. W.; Kwon, Y. Effect of Carboxylic Acid-Doped Carbon Nanotube Catalyst on the Performance of Aqueous Organic Redox Flow Battery Using the Modified Alloxazine and Ferrocyanide Redox Couple. *ACS Appl. Mater. Interfaces* **2018**, *10* (43), 36882–36891. https://doi.org/10.1021/acsami.8b10952.

(190) Marichelvam, T.; Manzoor Bhat, Z.; Thimmappa, R.; Devendrachari, M. C.; Kottaichamy, A. R.; Naranammalpuram Sundaram, V. N.; Thotiyl, M. O. Hydrogen Fuel Exhaling Zn−Ferricyanide Redox Flow Battery. *ACS Sustain. Chem. Eng.* **2019**, *7* (19), 16241–16246. https://doi.org/10.1021/acssuschemeng.9b03213.

(191) Zhang, Y.; Cao, J.; Chen, Z.; Xu, J.; Yu, C. An Organic-Based Aqueous Hybrid Flow Battery with High Power and Long Cycle Life: A Tetrapyridophenazine/Ferrocyanide System. *J. Mater. Chem. A* **2020**, *8* (14), 6874–6881. https://doi.org/10.1039/D0TA02070B.

(192) Lee, W.; Permatasari, A.; Kwon, Y. Neutral PH Aqueous Redox Flow Batteries Using an Anthraquinone-Ferrocyanide Redox Couple. *J. Mater. Chem. C* **2020**, *8* (17), 5727–5731. https://doi.org/10.1039/D0TC00640H.

(193) Jin, S.; Fell, E. M.; Vina-Lopez, L.; Jing, Y.; Michalak, P. W.; Gordon, R. G.; Aziz, M. J. Near Neutral pH Redox Flow Battery with Low Permeability and Long-Lifetime Phosphonated Viologen Active Species. *Adv. Energy Mater.* **2020**, *10* (20), 2000100. https://doi.org/10.1002/aenm.202000100.

(194) Orita, A.; Verde, M. G.; Sakai, M.; Meng, Y. S. A biomimetic redox flow battery based on flavin mononucleotide. *Nat. Commun.* **2016**, *7* (1), 13230. https://doi.org/10.1038/ncomms13230.

(195) Cheonho, C.; Wonmi, L.; Yongchai, K. The Effect of Additives on the Performance of Aqueous Organic Redox Flow Battery Using Quinoxaline and Ferrocyanide Redox Couple. *Korean Chem. Eng. Res.* **2019**, *57* (6), 847–852. https://doi.org/10.9713/KCER.2019.57.6.847.

(196) Luo, J.; Sam, A.; Hu, B.; DeBruler, C.; Wei, X.; Wang, W.; Liu, T. L. Unraveling PH Dependent Cycling Stability of Ferricyanide/Ferrocyanide in Redox Flow Batteries. *Nano Energy* **2017**, *42*, 215–221. https://doi.org/10.1016/j.nanoen.2017.10.057.

(197) Páez, T.; Martínez-Cuezva, A.; Palma, J.; Ventosa, E. Revisiting the Cycling Stability of Ferrocyanide in Alkaline Media for Redox Flow Batteries. *J. Power Sources* **2020**, *471*, 228453. https://doi.org/10.1016/j.jpowsour.2020.228453.

(198) Noh, C.; Chung, Y.; Kwon, Y. Organometallic Redox Flow Batteries Using Iron Triethanolamine and Cobalt Triethanolamine Complexes. *J. Power Sources* **2020**, *466*, 228333. https://doi.org/10.1016/j.jpowsour.2020.228333.

(199) Arroyo-Currás, N.; Hall, J. W.; Dick, J. E.; Jones, R. A.; Bard, A. J. An Alkaline Flow Battery Based on the Coordination Chemistry of Iron and Cobalt. *J. Electrochem. Soc.* **2014**, *162* (3), A378–A383. https://doi.org/10.1149/2.0461503jes.

(200) Wen, Y. H.; Zhang, H. M.; Qian, P.; Zhou, H. T.; Zhao, P.; Yi, B. L.; Yang, Y. S. A Study of the Fe(III)/Fe(II)–Triethanolamine Complex Redox Couple for Redox Flow Battery Application. *Electrochim. Acta* **2006**, *51* (18), 3769–3775. https://doi.org/10.1016/j.electacta.2005.10.040.

(201) Ji, Y.; Zhang, F.; Zhou, M.; Yu, J.; Wang, Q. Spatially Decoupled Hydrogen Evolution in Alkaline Conditions with a Redox Targeting-Based Flow Battery. *Int. J. Hydrogen Energy* **2020**, *45* (38), 18888–18894. https://doi.org/10.1016/j.ijhydene.2020.05.129.

(202) Newman, J.; Tiedemann, W. Porous-Electrode Theory with Battery Applications. *AIChE J.* **1975**, *21* (1), 25–41. https://doi.org/10.1002/aic.690210103.

(203) Smith, R. B.; Bazant, M. Z. Multiphase Porous Electrode Theory. *J. Electrochem. Soc.* **2017**, *164* (11), E3291–E3310. https://doi.org/10.1149/2.0171711jes.

(204) Suthar, B.; Northrop, P. W. C.; Rife, D.; Subramanian, V. R. Effect of Porosity, Thickness and Tortuosity on Capacity Fade of Anode. *J. Electrochem. Soc.* **2015**, *162* (9), A1708–A1717. https://doi.org/10.1149/2.0061509jes.

(205) You, X.; Ye, Q.; Cheng, P. The Dependence of Mass Transfer Coefficient on the Electrolyte Velocity in Carbon Felt Electrodes: Determination and Validation. *J. Electrochem. Soc.* **2017**, *164* (11), E3386–E3394. https://doi.org/10.1149/2.0401711jes.

(206) COMSOL. The Batteries & Fuel Cells Module User's Guide. https://doc.comsol.com/5.4/doc/com.comsol.help.bfc/BatteriesAndFuelCellsModuleUsersGuide.pdf (accessed Oct 12, 2020), version 5.4.

(207) Lyons, M. E. G.; Keeley, G. P. The Redox Behaviour of Randomly Dispersed Single Walled Carbon Nanotubes Both in the Absence and in the Presence of Adsorbed Glucose Oxidase. *Sensors*. **2006**, *6* (12), 1791–1826. https://doi.org/10.3390/s6121791.

(208) Daum, P. H.; Enke, C. G. Electrochemical Kinetics of the Ferri-Ferrocyanide Couple on Platinum. *Anal. Chem.* **1969**, *41* (4), 653–656. https://doi.org/10.1021/ac60273a007.

(209) Buckingham, M. A.; Hammoud, S.; Li, H.; Beale, C. J.; Sengel, J. T.; Aldous, L. A Fundamental Study of the Thermoelectrochemistry of Ferricyanide/Ferrocyanide: Cation, Concentration, Ratio, and Heterogeneous and Homogeneous Electrocatalysis Effects in Thermogalvanic Cells. *Sustain. Energy Fuels* **2020**, *4* (7), 3388–3399. https://doi.org/10.1039/D0SE00440E.

(210) Bard, A. J.; Faulkner, L. R. *Electrochemical Methods: Fundamentals and Applications*, 2nd ed.; John Wiley & Sons, Inc.: New Jersey, 2000.

(211) An, L.; Zhao, T. S.; Li, Y.; Wu, Q. Charge Carriers in Alkaline Direct Oxidation Fuel Cells. *Energy Environ. Sci.* **2012**, *5* (6), 7536–7538. https://doi.org/10.1039/C2EE21734A.

(212) Hu, J.; Zhang, H.; Xu, W.; Yuan, Z.; Li, X. Mechanism and Transfer Behavior of Ions in Nafion Membranes under Alkaline Media. *J. Memb. Sci.* **2018**, *566*, 8–14. https://doi.org/10.1016/j.memsci.2018.08.057.

(213) Zhou, X. L.; Zhao, T. S.; An, L.; Zeng, Y. K.; Yan, X. H. A Vanadium Redox Flow Battery Model Incorporating the Effect of Ion Concentrations on Ion Mobility. *Appl. Energy* **2015**, *158*, 157–166. https://doi.org/10.1016/j.apenergy.2015.08.028.

(214) Knehr, K. W.; Kumbur, E. C. Open Circuit Voltage of Vanadium Redox Flow Batteries: Discrepancy between Models and Experiments. *Electrochem. commun.* **2011**, *13* (4), 342–345. https://doi.org/10.1016/j.elecom.2011.01.020.

(215) Volkov, A. G.; Markin, V. S. Chapter 4 - Electric Properties of Oil/Water Interfaces. In *Emulsions: Structure Stability and Interactions*; Petsev, D. N., Ed.; Elsevier, 2004; Vol. 4, pp 91–182. https://doi.org/10.1016/S1573-4285(04)80006-1.

(216) COMSOL. COMSOL Multiphysics Reference Manual. https://doc.comsol.com/5.4/doc/com.comsol.help.comsol/COMSOL_ReferenceManual.pdf (accessed Oct 13, 2020), version 5.4.

(219) Atkinson, K. E.; Han, W.; Stewart, D. Stiff Differential Equations. In *Numerical Solution of Ordinary Differential Equations*; Wiley Online Books; John Wiley & Sons, Inc.: New Jersey, 2009; pp 127–148. https://doi.org/10.1002/9781118164495.ch8.

(220) Gong, K. University of Delaware, Newark, DE. Personal communication, 2019.

(221) Harris, D. C.; Lucy, C. A. *Quantitative Chemical Analysis*, 9th ed.; Freeman Custom Publishing: New York, NY, 2016.

(222) Shukla, K. S.; Mathur, P. C.; Bansal, O. P. Oxidation Kinetics of Triethanolamine by Alkaline Hexacyanoferrate(III). *J. Inorg. Nucl. Chem.* **1973**, *35* (4), 1301–1307. https://doi.org/10.1016/0022-1902(73)80203-9.

(223) Fuel Cell Store. Nafion NR211 and NR212. https://www.fuelcellstore.com/spec-sheets/chemours-nafion-211-212-spec-sheet.pdf (accessed Oct 15, 2020).

(224) Odgaard, M. Chapter 14 - The Use of Per-Fluorinated Sulfonic Acid (PFSA) Membrane as Electrolyte in Fuel Cells. In *Advanced Fluoride-Based Materials for Energy Conversion*; Nakajima, T., Groult, H., Eds.; Elsevier, 2015; pp 325–374. https://doi.org/10.1016/B978-0-12-800679-5.00014-2.

(225) Wu, X. W.; Yamamura, T.; Ohta, S.; Zhang, Q. X.; Lv, F. C.; Liu, C. M.; Shirasaki, K.; Satoh, I.; Shikama, T.; Lu, D.; Liu, S. Q. Acceleration of the Redox Kinetics of VO2+/VO2+ and V3+/V2+ Couples on Carbon Paper. *J. Appl. Electrochem.* **2011**, *41* (10), 1183. https://doi.org/10.1007/s10800-011-0343-7.

(226) Toray. Electrode base material for fuel cell Physical property table. https://www.torayca.com/en/lineup/composites/com_009_01.html (accessed Oct 15, 2020).

(227) Sakai, K.; Iwamura, S.; Sumida, R.; Ogino, I.; Mukai, S. R. Carbon Paper with a High Surface Area Prepared from Carbon Nanofibers Obtained through the Liquid Pulse Injection Technique. *ACS Omega* **2018**, *3* (1), 691–697. https://doi.org/10.1021/acsomega.7b01822.

(228) Singh, A. K.; Yasri, N.; Karan, K.; Roberts, E. P. L. Electrocatalytic Activity of Functionalized Carbon Paper Electrodes and Their Correlation to the Fermi Level Derived from Raman Spectra. *ACS Appl. Energy Mater.* **2019**, *2* (3), 2324–2336. https://doi.org/10.1021/acsaem.9b00180.

(229) Van Doren, E. A. F.; De Temmerman, P.-J. R. H.; Francisco, M. A. D.; Mast, J. Determination of the Volume-Specific Surface Area by Using Transmission Electron Tomography for Characterization and Definition of Nanomaterials. *J. Nanobiotechnology* **2011**, *9* (1), 17. https://doi.org/10.1186/1477-3155-9-17.

(230) Yuan-Hui, L.; Gregory, S. Diffusion of Ions in Sea Water and in Deep-Sea Sediments. *Geochim. Cosmochim. Acta* **1974**, *38* (5), 703–714. https://doi.org/10.1016/0016-7037(74)90145-8.

(231) Hikita, H.; Ishikawa, H.; Uku, K.; Murakami, T. Diffusivities of Mono-, Di-, and Triethanolamines in Aqueous Solutions. *J. Chem. Eng. Data* **1980**, *25* (4), 324–325. https://doi.org/10.1021/je60087a008.

(232) Kolthoff, I. M.; Tomsicek, W. J. The Oxidation Potential of the System Potassium Ferrocyanide–Potassium Ferricyanide at Various Ionic Strengths. *J. Phys. Chem.* **1935**, *39* (7), 945–954. https://doi.org/10.1021/j150367a004.

(233) Aaron, D. S.; Liu, Q.; Tang, Z.; Grim, G. M.; Papandrew, A. B.; Turhan, A.; Zawodzinski, T. A.; Mench, M. M. Dramatic Performance Gains in Vanadium Redox Flow Batteries through Modified Cell Architecture. *J. Power Sources* **2012**, *206*, 450–453. https://doi.org/10.1016/j.jpowsour.2011.12.026.

(234) Benzina, M.; Mowla, D.; Lacoste, G. Mass Transfer Studies in Porous Electrodes: Application of the Limiting Current Technique. *Chem. Eng. J.* **1983**, *27* (1), 1–7. https://doi.org/10.1016/0300-9467(83)80040-9.

(235) Sun, Y.-P.; Scott, K. An Analysis of the Influence of Mass Transfer on Porous Electrode Performance. *Chem. Eng. J.* **2004**, *102* (1), 83–91. https://doi.org/10.1016/j.cej.2004.01.026.

(236) Kinoshita, K.; Leach, S. C. Mass-Transfer Study of Carbon Felt, Flow-Through Electrode. *J. Electrochem. Soc.* **1982**, *129* (9), 1993–1997. https://doi.org/10.1149/1.2124338.

(237) Xu, Q.; Zhao, T. S. Determination of the Mass-Transport Properties of Vanadium Ions through the Porous Electrodes of Vanadium Redox Flow Batteries. *Phys. Chem. Chem. Phys.* **2013**, *15* (26), 10841–10848. https://doi.org/10.1039/C3CP51944A.

(238) Milshtein, J. D.; Tenny, K. M.; Barton, J. L.; Drake, J.; Darling, R. M.; Brushett, F. R. Quantifying Mass Transfer Rates in Redox Flow Batteries. *J. Electrochem. Soc.* **2017**, *164* (11), E3265–E3275. https://doi.org/10.1149/2.0201711jes.